DISSERTATIONES
CHIMICAE
UNIVERSITATIS
TARTUENSIS
158

MIHKEL VESTLI

Ultrasonic spray pyrolysis deposited electrolyte layers for intermediate temperature solid oxide fuel cells

DISSERTATIONES CHIMICAE UNIVERSITATIS TARTUENSIS
158

DISSERTATIONES CHIMICAE UNIVERSITATIS TARTUENSIS

158

MIHKEL VESTLI

Ultrasonic spray pyrolysis deposited electrolyte layers for intermediate temperature solid oxide fuel cells

UNIVERSITY OF TARTU
Press

Institute of Chemistry, Faculty of Science and Technology, University of Tartu, Estonia.

Dissertation was accepted for the commencement of the degree of *Doctor philosophiae* in Chemistry at the University of Tartu on June 30, 2016 by the Council of Institute of Chemistry, Faculty of Science and Technology, University of Tartu.

Supervisors: Prof. Enn Lust, University of Tartu, Estonia
Ph.D. Gunnar Nurk, University of Tartu, Estonia

Opponent: Prof. Peter Holtappels, Technical University of Denmark, Denmark

Commencement: August 25, 2016, at 11:00, 14a Ravila Street, Tartu (Chemicum)

ISSN 1406-0299
ISBN 978-9949-77-199-8 (print)
ISBN 978-9949-77-200-1 (pdf)

University of Tartu Press
www.tyk.ee

TABLE OF CONTENTS

1. LIST OF ORIGINAL PUBLICATIONS

I. **M. Vestli**, E. Lust, G. Nurk, Characterization of Terbium and Samarium Co-Doped Ceria Films Prepared Using Ultrasonic Spray Pyrolysis, J. Electrochem. Soc. 162 (2015) F812–F820.

II. M. Maide, O. Korjus, **M. Vestli**, T. Romann, J. Aruväli, K. Kirsimäe, G. Nurk, Comparative Study of $BaY_{0.1}Zr_{0.9}O_{3-\delta}$ Protective Layers Deposited to $BaY_{0.1}Ce_{0.9}O_{3-\delta}$ Membrane Using Ultrasonic Spray Pyrolysis and Magnetron Sputtering Methods, J. Electrochem. Soc. 163 (2016) F443–F447 (licensed under CC BY-NC-ND).

III. G. Nurk, **M. Vestli**, P. Moller, R. Jaaniso, M. Kodu, H. Mandar, T. Romann, R. Kanarbik, E. Lust, Mobility of Sr in Gadolinia Doped Ceria Barrier Layers Prepared Using Spray Pyrolysis, Pulsed Laser Deposition and Magnetron Sputtering Methods, J. Electrochem. Soc. 163 (2016) F88–F96 (licensed under CC BY-NC-ND).

IV. **M. Vestli**, G. Nurk, E. Lust, Electrical Properties of Tb and Sm Co-Doped Ceria Electrolyte at Different Oxygen Partial Pressures, ECS Trans. 35 (2011) 1219–1224.

V. **M. Vestli**, M. Maide, G. Nurk, E. Lust, Characterization of Doped Ceria Films as SOFC Electrolyte Prepared by Using Ultrasonic Spray Pyrolysis Method, ECS Trans. 57 (2013) 1159–1165.

VI. **M. Vestli**, G. Nurk, Characterization of Terbium and Samarium Co-Doped Ceria Films as SOFC Electrolyte Prepared by Using Ultrasonic Spray Pyrolysis Method, ECS Trans. 68 (2015) 359–367.

Author´s contribution:

Paper I: Performed the synthesis of samples. Participated in the analysis of data. Mainly responsible for the preparation of the manuscript.

Paper II: Participated in the ultrasonic spray pyrolysis deposition, analysis of data and preparation of the manuscript.

Paper III: Participated in the ultrasonic spray pyrolysis deposition, analysis of data and preparation of the manuscript.

Paper IV: Performed the synthesis of samples and electrochemical characterization. Participated in the analysis of data. Mainly responsible for the preparation of the manuscript.

Paper V: Performed the synthesis of samples and electrochemical characterization. Participated in the analysis of data. Mainly responsible for the preparation of the manuscript.

Paper VI: Performed the synthesis of samples and electrochemical characterization. Participated in the analysis of data. Mainly responsible for the preparation of the manuscript.

2. ABBREVATIONS AND SYMBOLS

a_{O_2}	oxygen activity
BCY	$BaCe_{0.9}Y_{0.1}O_{3-\delta}$
BZY	$BaZr_{0.9}Y_{0.1}O_{3-\delta}$
Ce_{Ce}^{x}	Ce^{4+} cation at a cerium site
Ce'_{Ce}	Ce^{3+} cation at a cerium site
DC	direct current
DSC	differential scanning calorimetry
DTA	differential thermal analysis
D_{Ce}^{x}	more easily reducible cation at a cerium site
E	cell potential
$E_{a,bulk}$	activation energy for mobility in bulk
$E_{a,gb}$	activation energy for mobility at grain boundary
$E_{a,tot}$	total activation energy
E_{act}	activation energy
EDS	energy dispersive X-ray spectroscopy
Endo	endothermal
Exo	exothermal
GDC	Gd-doped CeO_2
$h^{\cdot}$	electron hole
HR	high resolution
I	current density
IT	intermediate temperature
LSC	$La_xSr_{1-x}CoO_{3-\delta}$
LSCF	$La_xSr_{1-x}Co_yFe_{1-y}O_{3-\delta}$
MS	magnetron sputtering
n	flexible exponent value
Nd:YAG	Nd-doped yttrium aluminium garnet
P	power density
pO_2	oxygen partial pressure
PSC	$Pr_xSr_{1-x}CoO_{3-\delta}$
O_O^x	O^{2-} anion at an oxygen site
OCP	open circuit potential
$OH_O^{\cdot}$	positively charged protonic defect at an oxygen site
PLD	pulsed laser deposition
P_n	lower bound of electrolytic domain
R_a	average roughness
R_{pol}	polarization resistance
R_s	high-frequency series resistance
RF	radio frequency
S	substrate
ScSZ	Sc-stabilized ZrO_2

SDC	Sm-doped ceria
SEM	scanning electron microscopy
SIMS	secondary ion mass spectrometry
Sm'_{Ce}	Sm^{3+} cation at a cerium site
SOFC	solid oxide fuel cell
SP	ultrasonic spray pyrolysis
T	temperature
Tb^{x}_{Ce}	Tb^{4+} cation at a cerium site
Tb'_{Ce}	Tb^{3+} cation at a cerium site
TEM	transmission electron microscopy
TG	thermogravimetry
TOF	time-of-flight
TSDC	$Ce_{0.9}Sm_{0.1-x}Tb_xO_{2-\delta}$
$V^{\cdot\cdot}_{O}$	oxygen vacancy at an oxygen site
XRD	X-ray diffraction
YSZ	Y-stabilized ZrO_2
Z'	real part of impedance
Z''	imaginary part of impedance
σ	conductivity
σ^{0}_{el}	n-type electronic conductivity at log a_{O_2}= 0
σ_{ion}	ionic conductivity
σ^{tot}	total conductivity
ω	angular frequency

3. INTRODUCTION

Current world energy production is based mainly on extraction and burning of polluting hydrocarbon fuels (oil, coal, natural gas). The particulates and gaseous products (CO_2, NO_x, SO_x) emitted from combustion processes have negative impacts on health and environment. In the light of these issues, more environmentally friendly energy technologies are increasingly drawing more attention. Solid oxide fuel cell (SOFC) has been demonstrated to be a promising technology for efficient and cleaner power generation. Its attractiveness relies on high efficiency, and energy and power density. SOFC can be operated on a variety of fuels, including zero-emission hydrogen and renewable biofuels. Additionally, SOFC operated in reversible i.e. electrolyzer regime is suitable for energy storage application in smart-grids.

The operation of SOFC is based on electrochemical oxidation of fuel with an oxidant. The core of SOFC consists of a dense ion conducting solid electrolyte sandwiched between porous anode and cathode. Each component must meet a specific set of requirements. The key requirements for the SOFC electrolyte are high density, good ionic conductivity but negligible electronic conductivity. Additionally, the SOFC electrolyte must have mechanical compatibility with the electrode materials and chemical stability over a wide range of temperature and oxygen partial pressure.

Big efforts have been made to commercialize the SOFC technology by lowering its cost and extending lifetime of the SOFC systems. The main strategy is to lower the working temperature to intermediate temperature (IT) range (600–800 ºC), while maintaining the high performance. As the classical SOFC electrolytes based on stabilized ZrO_2 have poor ionic conductivity within IT range, alternative mainly ceria based electrolyte materials have been considered. Due to their higher ionic conductivity and good stability with the cathode materials, Sm-doped CeO_2 or Gd-doped CeO_2 are the potential replacements for stabilized ZrO_2 as an IT-SOFC electrolyte material. However, the main disadvantage of CeO_2 based solid electrolytes is the partial electronic conductivity at moderately and highly reducing conditions, resulting in efficiency losses of SOFC. Several approaches have been studied to assess the possibility of suppressing the partial electronic conductivity. Previous experimental studies have demonstrated possible electron trapping by some 4f-elements, like Tb, used as a co-dopant for Sm-doped CeO_2.

SOFC cathode materials like $La_xSr_{1-x}CoO_{3-\delta}$ (LSC), $Pr_xSr_{1-x}CoO_{3-\delta}$ (PSC) or $La_xSr_{1-x}Co_yFe_{1-y}O_{3-\delta}$ (LSCF) are suitable cathode materials for the IT range. However, the main drawback is their tendency to react with stabilized ZrO_2 at higher temperatures. This results in the formation of zirconates ($SrZrO_3$) with low oxide-ion conductivity at the electrolyte|cathode interface. Due to its good chemical stability with LSC, PSC or LSCF, doped CeO_2, usually $Ce_{0.9}Gd_{0.1}O_{2-\delta}$, has been used as a protective interlayer between the stabilized ZrO_2 electrolyte and the cathode to suppress the formation of zirconates.

Various proton conducting oxides are also proposed as electrolyte materials for the IT-SOFC application. They possess higher ionic conductivity and lower activation energy at the IT range compared with oxide-ion conducting materials like stabilized ZrO_2 and doped CeO_2. Additionally, fuel utilization is higher in the case of proton conducting electrolyte, as the fuel is not diluted with water at the anode side. Therefore, several cerates and zirconates with different dopants have been tested as potential IT-SOFC electrolyte materials. Although doped $BaCeO_3$ possesses the highest protonic conductivity, its chemical stability with respect to carbonate and hydroxide formation is rather poor in CO_2 and steam containing environment, respectively. One method for increasing the chemical stability of $BaCeO_3$ is to coat it with a thin-film protective layer. Chemically more stable doped $BaZrO_3$ has shown some good protective behaviour, although its ionic conductivity is lower.

Another strategy to compensate the decrease of ionic conductivity at the IT range is to reduce the thickness of SOFC electrolyte. Spray pyrolysis, based on atomization of the precursor solution, has turned up to be a cost-effective method for deposition of homogenous high quality oxide layers, compared with more complex chemical or physical vapor deposition techniques. Ultrasonic spray pyrolysis method has the advantage of building up an oxide layer with greater homogeneity.

The aim of this work was to evaluate the ultrasonic spray pyrolysis process as a method for deposition of oxide-ion and proton conducting electrolyte layers with different protective functions for IT-SOFC application and to prepare homogenous functional layers. $Ce_{0.9}Sm_{0.1-x}Tb_xO_{2-\delta}$ layers with protective properties against the electronic conductivity were deposited using the ultrasonic spray pyrolysis method. Influence of Tb dopant and thermal treatment on microstructural and electrical properties of the $Ce_{0.9}Sm_{0.1-x}Tb_xO_{2-\delta}$ layers was studied. The ultrasonic spray pyrolysis (SP) method was also used to deposit $Ce_{0.9}Gd_{0.1}O_{2-\delta}$ as a chemical barrier layer for separation of LSC cathode and YSZ electrolyte. CO_2 resistant $BaZr_{1-x}Y_xO_{3-\delta}$ protective layers were deposited by using the SP method onto proton conducting membrane. Mobility of cations during thermal treatment of spray-pyrolyzed raw layers was studied using secondary ion mass spectrometry and transmission electron microscopy with energy dispersive X-ray spectroscopy method. More complex pulsed laser deposition and magnetron sputtering methods were also applied for deposition of layers and comparative analysis has been conducted. Influence of deposition method characteristics and thermal treatment regimes on physical and electrical properties of the protective layers has been analyzed in detail.

4. LITERATURE OVERVIEW

4.1. SOFC

Fuel cells are an attractive devices for generating electricity from a variety of fuels, including sustainable biofuels. Although the principles and effects of fuel cell operation were discovered by Schoenbein, Sir William Robert Grove demonstrated the first operating fuel cell in 1839. Long-lasting development of solid oxide fuel cell (SOFC) technology started when W. Nernst discovered solid electrolyte in 1899. First operating SOFC at 1000 °C was demonstrated by Paur and Preis in 1937. Intensive research and overwhelming development of practical SOFCs began in the early 1960s [1–7].

SOFC is a solid-state energy conversion device that produces electricity and heat by electrochemical oxidation of fuel with an oxidant. Although the overall reaction is the same as that occurring in the combustion process, it is divided into two separate electrochemical reactions occurring at the opposite sides of the solid electrolyte separating anode and cathode electrode compartments. In the case of hydrogen fuel, the chemical reaction product is water. When hydrocarbon fuel is used, the exhaust gas contains also carbon dioxide. A single SOFC consists of two porous electrodes (anode and cathode) separated usually by an oxide-ion conducting solid electrolyte. The fuel is introduced to the anode, where it is oxidized by the oxide ions provided by the solid electrolyte. The oxidant (often oxygen from air) is fed to the cathode, where it is reduced to oxide ions. The electrons released in the anode are directed through the external circuit to the cathode producing direct-current in the electrical circuit. Current SOFC materials require high operating temperatures (600–1000 °C) for sufficient conductivity and high (moderate) electrode kinetics. A SOFC single cell produces less than 1 V potential difference (so-called cell potential), which is not sufficient for practical applications. In order to increase the SOFC electrical potential, SOFC stacks are built by connecting the single cells together with interconnects in electrical series [1–10].

In addition to hydrogen, available hydrocarbon fuels like gasoline, diesel, alcohol, methane, butane and synthetic gas can be used as a fuel in SOFC. High operating temperatures promote rapid reaction kinetics, allowing internal reforming of hydrocarbon fuels within the fuel cell without an additional fuel processing unit. SOFC has significantly high theoretical fuel-to-electricity conversion efficiency of 45–60% compared with that of traditional coal and natural gas power plants. Since the chemical energy of fuel is converted directly into electrical energy and heat without combustion, the usual losses involved in the intermediate steps of fuel conversion (chemical energy → heat → mechanical energy → electrical energy) are avoided. The efficiency can be further improved to 70–80%, when the by-product heat is used to drive a gas turbine in a combined cycle system. Emissions of pollutants such as NO_x, SO_x, unburned hydrocarbons and particulates are either negligible or extremely low.

Due to the higher conversion efficiency, CO_2 emissions generated from fossil fuels per kWh electricity are lower.

The use of a solid electrolyte in a SOFC eliminates problems related to liquid electrolyte management. Unlike combustion engines and gas turbines, SOFC systems can be made in different sizes (in a wide power range from milliwatts to megawatts) and operated at part-load conditions without affecting the efficiency. Since no moving parts (except air blower and valves in the system) are included, SOFC systems have low maintenance costs. Additionally, vibration and noise levels are very low during operation. These very big advantages allow to use SOFC in urban residential areas [1–5,7–9].

Each component serves several functions in the SOFC and must adhere a very specific combination of requirements. SOFC components must have adequate chemical, morphological and mechanical stability under operating conditions, chemical stability with the neighbouring components and proper electrical properties. Additionally, the coefficients of thermal expansion of the components must match to avoid separation or cracking during fabrication and operation, i.e., under fluctuating temperature conditions. The electrolyte must be a dense pure ion-conductor, while the electrodes must be porous with sufficient electrocatalytical activity and mixed conductivity. From a practical point of view, the SOFC components must have good fabricability and reasonable cost [1,2,5–7,10–13].

Despite excellent technical progress made in SOFC technology, further research activity is required in development of suitable materials and especially the cheap fabrication processes. Therefore, some novel stack designs are being developed. Issues related with time-stability, reliability and high cost of SOFC are hindering extensive commercialization of SOFC technology. Commercialization of SOFC systems for residential combined heat and power application has already begun. Multi-kilowatt SOFC systems have shown excellent performance with adequate time-stability [1,6,8,10,14].

4.2. Intermediate temperature SOFC

Current large-scale SOFC systems based on stabilized zirconia electrolyte are normally operated at temperatures of 800–1000 ºC in order to achieve adequate efficiency and power density. However, the high operating temperatures have several disadvantages. Higher thermal stresses are generated during thermal cycling of a multilayer device with the components having slightly different coefficients of thermal expansion. Additionally, larger temperature differences tend to develop and start-up time of the system is longer. Lowering the operating temperature to intermediate temperature range (600–800 ºC) reduces both the stresses and the start-up time, which is crucial for the commercialization of SOFC. Radiation heat losses from the fuel cell stack can be reduced with decreasing operating temperature. Another advantage is the reduced intensity of coarsening and sintering processes, which otherwise will

make rather difficult to maintain the high specific surface areas of electrodes at high temperatures. The chemical and mechanical stability of some materials like ceria can be increased at the intermediate temperature range. A temperature reduction would allow greater flexibility in the choice of SOFC materials. A switch can be made from ceramic to inexpensive ferritic steel interconnects. Other issues that can be addressed with lower operating temperature are elemental interdiffusion rate across interfaces, metallic corrosion, chromium vaporization from the interconnects and ceramic aging effects. Thus, IT-SOFC could have improved reliability, longer cell life and lowered cost [1,15–18]. Although, there have already been some thoughts about low temperature solid oxide fuel cells [19,20].

However, lowering the operating temperature causes some new problems. One is increased ohmic loss across the solid electrolyte, which would decrease SOFC performance. This problem has been addressed by replacing the stabilized zirconia by solid electrolytes possessing higher ionic conductivity. There is a variety of alternative materials proposed for SOFC electrolyte [5,17,18,21–23]. Another strategy to reduce the ohmic loss is decreasing thickness of the electrolyte. A number of methods have been used for preparation of electrolyte layers with the thickness smaller than 10 μm [1,14,24–32].

4.3. SOFC electrolyte

The solid electrolyte is the key component of SOFC. Its main function is the transport of ions under a gradient of chemical potentials between the electrodes. The flow of ions is balanced by the charge from the electron flow completing the electrical circuit in the fuel cell. The electrolyte also acts as a separator of the fuel and the oxidant compartments in the fuel cell. Thus, the electrolyte material must be stable in both reducing and oxidizing environments and have sufficient density in order to avoid electrical potential losses caused by gas cross-leakage. The electrolyte must have sufficient ionic conductivity and negligible electronic conductivity to prevent a decrease in the efficiency of SOFC due to the mixed conductivity of the electrolyte. The conductivity of the electrolyte must be time-stable. Also chemical and thermal compatibility with the other cell components are required from room temperature to the operating and fabrication temperatures [1,2,12,13].

The operation of SOFC is based on oxide materials with ionic conductivity via mobility of the charged species in the crystal lattice [1,33]. The electrolyte must have ionic conductivity for one of the elements present in the gaseous reactants. The SOFC electrolyte can be either an oxide-ion or proton conductor. For some materials both conductivity types can occur simultaneously at the specific operating conditions. Electrolyte selection determines the ion type (conductivity) involved in the redox reactions and the direction of ion flow in the electrolyte. The oxide-ion conductors require electroreduction of oxygen occurring at the cathode and following transport to the anode to be reacted with

the fuel. In the case of the proton conductors, the protons generated in the anode are transported to the cathode, where they react with oxygen [1,16,34]. This means that the water is produced at the oxidant side, thus the fuel dilution causing a decrease of open circuit potential (OCP) is avoided and fuel utilization is higher. The proton conductor SOFC is reported to have higher efficiency at lower temperatures compared with that of the oxide-ion conductor SOFC [35,36]. However, the stability issues in CO_2 containing environments can occur for some proton conducting materials, making problematic to use syngas and hydrocarbon fuels. Additionally, SOFC based on the proton conductors is not be able to electrochemically oxidize CO, one of the components in syngas [1,16,37–39].

The oxide-ion conductors have received much attention as SOFC electrolyte material. Present SOFC is almost exclusively based on stabilized zirconia, although doped ceria electrolyte has been also used, especially at the intermediate temperatures (600–800 °C). Implementation of the proton-conductor SOFC has been delayed by the low stability and quick degradation problems. Although these materials hold a lot of potential for future SOFC providing high power density values, further development work is required [1,16,34,39].

4.3.1. Doped ceria

An ideal SOFC electrolyte must be a pure oxide-ion conductor under normal SOFC operating conditions. Oxides with the fluorite structure are the classical ionic conductors and attractive materials as the SOFC electrolytes. The general formula of the fluorite structure is MO_2, where M is a large tetravalent cation. The materials with the fluorite structure are for example ceria (CeO_2), urania (UO_2) and thoria (ThO_2). Doping the MO_2 oxides by inserting cations with lower valence into the crystal lattice introduces the oxide-ion conductivity, because the oxygen vacancies are generated to maintain the overall charge neutrality and provide lattice sites for diffusion of the oxide ions in the crystal structure. Most oxide-ion conductors are actually mixed conductors having some degree of electronic conductivity. The electronic conductivity in an oxide-ion conductor occurs via electrons or electron holes with high mobility. Low oxygen partial pressure of the surrounding environment could reduce some oxide-ion conducting SOFC electrolytes like ceria to a degree that their ionic transference number (the ratio of the ionic conductivity to the total conductivity) is significantly reduced and the efficiency of SOFC is decreased due to the electronic shorting. Due to the high mobility even very low concentrations of the electronic charge carriers decrease the ionic transference number. Thus, at fixed temperatures the doped fluorite-type oxide-ion conductors can have sufficiently large ionic transference number over a certain range of oxygen partial pressures [1,2,13,40,41].

Pure CeO_2 exhibits n-type electronic conductivity with low oxide-ion conductivity. The n-type conductivity takes place by a small polaron hopping

mechanism. The oxide-ion conductivity can be increased remarkably at higher temperature by doping CeO_2 with a divalent or trivalent oxide. Rare-earth oxides like La_2O_3, Y_2O_3, Sm_2O_3, Gd_2O_3, and more cost-effective CaO and SrO, are just some examples of the dopants. The highest ionic conductivities have been reported for Sm_2O_3 and Gd_2O_3 dopants, which have the lowest ion size mismatch with CeO_2. The dissolution of Sm into the CeO_2 lattice can be written using the Kröger-Vink notation:

$$Sm_2O_3 = 2Sm'_{Ce} + 3O_O^x + V_O^{\cdot\cdot} \quad (1)$$

where Sm'_{Ce}, O_O^x and $V_O^{\cdot\cdot}$ represent a Sm^{3+} cation at a cerium site, an O^{2-} anion at an oxygen site and an oxygen vacancy at an oxygen site, respectively. For every dopant there is a specific optimal concentration for the maximum conductivity. Doped CeO_2 demonstrates the superior conductivity and the lower conduction activation energy compared with the stabilized zirconia (ZrO_2) [12,13,21,34,42].

However, the tendency of doped ceria to undergo the partial reduction ($Ce^{4+} \rightarrow Ce^{3+}$) at higher temperatures and lower oxygen partial pressures is the main issue, which limits its application as SOFC electrolyte material. The electronic conductivity of the ceria based electrolytes is caused by the hypostoichiometry-generated small polarons. The reduction reaction of ceria can be written as:

$$O_O^x + 2Ce_{Ce}^x = 1/2O_2 + V_O^{\cdot\cdot} + 2Ce'_{Ce} \quad (2)$$

where Ce_{Ce}^x and Ce'_{Ce} represent a Ce^{4+} cation and a Ce^{3+} cation at a cerium site, respectively. The n-type conductivity caused by the reduction of ceria lowers the SOFC performance as described above. Additionally, the partial reduction of ceria at the anode side causes additionally lattice expansion, which decreases the mechanical stability of the cell. Because of these problems, SOFC based on the doped CeO_2 electrolyte has been considered for the intermediate and low temperature regimes only [12,13,21,34,42–44].

Characteristics of the electrolytic domain boundaries of doped CeO_2 are influenced by the properties of dopant and temperature. It has been demonstrated that the reducibility of doped CeO_2 and its electronic conductivity is enhanced with increasing dopant concentration at intermediate temperatures [45,46]. The electronic conductivity of doped CeO_2 has been suppressed by using co-doping strategy [1,12,32]. It has been reported by Maricle et al. [47] that 3 mol% of Pr as a co-dopant for Gd-doped ceria (GDC) increases the membrane redox stability. Influence of Nd, La, Y, Sm and Pr ions as co-dopants for GDC have been studied comparatively with focus on the ionic and electronic properties of electrolytes [48]. The formation of an electron blocking BaO-CeO_2-Sm_2O_3 ternary composite interlayer between the Ba containing anode and the Sm-doped ceria (SDC) electrolyte has been reported by W. Sun et al. [49]. However, one promising approach to suppress the partial electronic

conductivity of the ceria based electrolyte has been demonstrated using some 4f-elements as electron traps [50]. In equal proportion with Sm, Tb was found to be an effective electron trap for the microcrystalline bulk specimen of ceria electrolyte. It was demonstrated by Yoo et al., that by co-doping of the SDC electrolyte with Tb, it is possible to suppress the partial electronic conductivity by half an order of magnitude compared with that established for the 10 mol% Gd-doped ceria [51]. This could result in the lower bound of its electrolytic domain (temperature and oxygen partial pressure range at which the material is dominantly an ionic conductor) extended by two orders of magnitude to lower oxygen partial pressures. It has been suggested that Tb (existing as a mixture of Tb^{4+} and Tb^{3+} valence states) as a co-dopant decreases the amount of Ce'_{Ce} species in reducing conditions. It was concluded that excess electrons are trapped on Tb due to its tendency to reduce more easily [51–53]. Trapping of electrons by more easily reducible species D^{x}_{Ce} could be expressed as:

$$Ce'_{Ce} + D^{x}_{Ce} = Ce^{x}_{Ce} + D'_{Ce} \quad (3)$$

Previous works have demonstrated that the magnitude of ionic and electronic conductivities are dependent on the Tb amount in electrolyte. In the case of small Tb concentrations doped ceria is still a pure ionic conductor. Considerably larger amounts of Tb caused the increase of electronic conductivity [32,54,55].

Doped ceria, usually $Ce_{0.9}Gd_{0.1}O_{2-\delta}$, is also proposed as a chemical barrier layer between YSZ and doped rare-earth cobaltite ($La_xSr_{1-x}CoO_{3-\delta}$, $Pr_xSr_{1-x}CoO_{3-\delta}$ or $La_xSr_{1-x}Co_yFe_{1-y}O_{3-\delta}$) cathodes [14,56–58]. Contrary to zirconia, ceria has good chemical stability with these cathode materials suitable for the IT-SOFC application [59]. The function of the barrier layer is to prevent chemical reaction and the consequent formation of zirconates ($SrZrO_3$) with low oxide-ion conductivity [60,61] between $La_xSr_{1-x}CoO_{3-\delta}$ (LSC), $Pr_xSr_{1-x}CoO_{3-\delta}$ (PSC) or $La_xSr_{1-x}Co_yFe_{1-y}O_{3-\delta}$ (LSCF) and yttria-stabilized zirconia (YSZ) layers. Previous studies have brought out different aspects about using the mentioned barrier layer [56–58]. Non-optimal preparation conditions of the GDC layer and cathode can result in interdiffusion of constituent cations between different layers resulting in the formation of new phases. High sintering temperature promotes diffusion of Sr and Zr cations causing the formation of $SrZrO_3$ between the cathode and GDC barrier layer [62]. Heat treatment of GDC at temperatures T>1200 ºC can also result in the formation of a less conductive solid solution between YSZ and GDC [57,63]. Sr diffusion is also influenced by the microstructure and thickness of GDC layer [57,58,64–70]. A positive influence of Sr on GDC densification has been reported [71]. The reaction rate and mass transfer parameters depend significantly on the method used for the preparation of GDC film, pretreatment of materials as well as on the heat treatment conditions like the duration and temperature of sintering and the thickness of the GDC barrier layer developed [31].

4.3.2. Proton conductors

Perovskite oxides with the general formula of ABO_3, where A is a divalent or trivalent cation and B is a tetravalent or trivalent cation, are attractive SOFC electrolyte materials because of their higher conductivity and lower activation energy at intermediate temperatures compared with the conventional oxide-ion conductors. Although hydrogen is not present in their chemical composition, some perovskite oxides have the proton conductivity in a wet atmosphere at high temperatures. Doped perovskites exhibit either pure oxide-ion or mixed conductivity depending on the oxygen partial pressure. Usually the B-site cation in ABO_3 is substituted with an appropriate cation possessing lower valency in order to introduce the oxygen vacancies. At high oxygen partial pressures, the oxygen vacancies are consumed by oxygen producing electron holes [1,17,38,72–74]. Under these conditions the material has both ionic and p-type conductivity. In a wet atmosphere, protonic defects are formed by water dissociation reaction. Hydroxide ions formed occupy the oxygen vacancies and the protons combine with the lattice oxygen creating $(OH)_O^{\cdot}$ defects with a positive charge:

$$H_2O + O_O^x + V_O^{\cdot\cdot} = 2(OH)_O^{\cdot} \quad (4)$$

The positively charged protonic defects are capable for migration via the oxygen vacancies or sites adjacent to the oxide ions. Depending on the perovskite composition, temperature and water vapor concentration, the material can be purely proton or mixed ion conductive. The oxide-ion conductivity is increased in the case of lower water vapor pressures [1,38,72–74].

$BaCeO_3$, $SrCeO_3$ and $BaZrO_3$, which are doped for example with Y, Gd or Yb cations, are the most studied perovskite oxides considered for SOFC application characterized with high proton conductivity [1,2,38,72,75–77]. Doped $BaCeO_3$ shows the highest proton conductivity, but also chemical instability. $BaCeO_3$ and $SrCeO_3$ are thermodynamically only weakly stabilized and the formation of carbonates and hydroxides takes place in the presence of CO_2 and steam, respectively. The stability towards CO_2 and humid atmospheres increases in the order of materials: cerate < zirconate < titanate, i.e., opposite to the direction of the increase of stability of protonic defects and as the B site cation electronegativity increases [30,74]. Some promising results have been achieved to overcome the instability problems with doping and/or mixing of different phase [76–79].

One of the promising approaches for achieving reasonable compromise between the chemical stability and conductivity is to prepare a bilayer membrane with a well-conducting supportive membrane and a thin chemically stable less-conducting layer on top of it. However, so far only few studies have examined a multilayer proton conducting single cell. A few studies have analyzed the $BaZr_{0.8}Y_{0.2}O_{3-\delta}$ protective layers with different thicknesses on the $BaCe_{0.8}Y_{0.2}O_{3-\delta}$ supportive membrane [30,80,81]. The authors pointed out that

the protective layers were chemically stable and power density of SOFC single cell depends on the layer thickness. The chemical stability of the $BaCe_{0.8}Y_{0.2}O_{3-\delta}$ membrane was increased when it was sandwiched between two $BaZr_{0.7}Pr_{0.1}Y_{0.2}O_{3-\delta}$ films [30,82].

4.4. Cation diffusion in fluorite-type structure

Diffusion (mass transfer) in crystalline ceramics is a process based on ionic motion driven by the concentration gradient. Diffusion may be viewed as periodic jumping of ions required to overcome an energy barrier (activation energy) in the process. Different diffusion mechanisms are possible, determined by the types of defects providing the pathway for mass transfer in the material. Bulk diffusion takes place in the lattice via point defects like vacancies and interstitials. The bulk diffusion coefficient depends on the concentration of defects [83]. In addition to temperature and pressure, the concentration of point defects may depend also on the oxygen partial pressure, influencing the oxygen stoichiometry and oxidation state of cations [84]. Grain boundary diffusion occurs through disordered grain boundary phases between the grains. Grain boundary diffusion is reported to have a higher rate compared with the bulk diffusion process (up to six orders of magnitude faster in the case of zirconia) due to its highly defective nature [83–85]. Grain boundary diffusivity is influenced by the grain size (microstructure) and charge effects [85]. Additionally, diffusion can occur within a thin surface layer of solids via vacancies and other types of defects. Thus, porosity of material could affect the diffusion of species [83,86].

Difference of dopant mobilities in bulk can be explained by size and charge effects of cations, which can distort their local environment depending on the size mismatch in respect to the host cation. Diffusion must take place in a manner that the overall stoichiometry and electroneutrality in the solid is maintained. Simultaneous diffusion of different ions is determined by the most slowly diffusing one. The potential gradient, developed by the transport of faster ions, inhibits their further motion, but accelerates at the same time the diffusion of slower ions [83,85].

It is confirmed that the cation diffusion in the fluorite with oxygen deficit occurs through interstitial mechanism [87,88]. The cation mobility can be influenced by the type of dopant and concentration of oxygen vacancies. Acceptor dopants introduced into ceria are known for providing oxygen vacancies, which determine the concentration of cation interstitials and thus, the cation diffusivity. Cations, despite their smaller size, have typically lower diffusion coefficient (up to ten orders of magnitude lower) compared with oxygen and thus, are the limiting species for the mass transfer in oxide materials [87,88]. In the case of zirconia, the similar diffusivities for oxygen and cations were obtained only with low dopant concentrations and very high temperatures [85]. Fast cation diffusion was observed in the reduced Gd-doped ceria due to the large concentration of oxygen vacancies and reduced size mismatch between

the dopant and host ion [84,88]. The high mobility of Sc^{3+} ion in ceria was ascribed to the smaller size of the dopant and to the resulting local lattice distortion [87]. The self-diffusion of large Ce^{3+} or Ce^{4+} ions in undoped ceria is limited by the low concentration of interstitial defect [89].

Several studies have reported the grain boundaries as pathway for the fast Sr diffusion [57,66,86]. Wang et al. demonstrated the enhanced Sr and Zr diffusion into the LSCF|GDC interface under polarization condition [62]. Wang et al. reported that Co and Fe, which diffused from the LSCF cathode into the grain boundaries of the GDC barrier layer prepared by pulsed laser deposition method, have a strong influence on the diffusion of Sr and Zr [90]. The diffusion of cations along the grain boundaries alters the grain boundary chemistry and thus, its electrical properties [91].

The size and valence of cation affects also the grain boundary mobility, thus influencing the rate of sintering and grain growth processes [87,88]. The slowest diffusing species will be rate-determining and determine the longevity and performance of the devices based on solid state ionics like SOFC. It has been demonstrated that the cations can diffuse in the length of hundreds of nanometers to a few micrometers along the grain boundaries within a few hours at 700–800 °C. Consequently, the grain boundary diffusion of cations may limit lifetime and performance of SOFC based on too thin electrolyte [91].

4.5. Methods for deposition of electrolyte layer

4.5.1. Spray pyrolysis

Spray pyrolysis involves forming small droplets by atomization of the precursor solution which are transported by carrier gas to the heated substrate. A wide variety of compounds like nitrates, chlorides and metal-organic salts containing the desirable metal ion can be used as precursor salts. After solvent evaporation and thermal decomposition the droplets of precursor solution form deposits on the surface of substrate. The film is built up by overlapping deposits during the spraying process for some period of time. In the case of the ultrasonic spray pyrolysis method, the atomization of the precursor solution results in a finer mist with a relatively narrow droplet size distribution compared to that formed using the simple pressurized spray pyrolysis method. As a result of the narrower droplet size distribution, the formation of defects and porosity in the raw film caused by differences in evaporation and deposition of the droplets with varying sizes noticeably can be suppressed. Therefore, the homogeneous thin films can be deposited in a more controlled manner [32,92–95].

Spray pyrolysis has proven to be a time- and cost-efficient method for deposition of homogenous high quality thin films with reasonable cost compared to chemical or physical vapor deposition methods [32,92,93,96]. In addition, the spray pyrolysis method is suitable for deposition of metal oxide films on objects (supports) with comparatively large areas such as planar SOFC components [14,32,92]. It has been demonstrated that the pressurized spray pyrolysis

method is a convenient way to deposit dense homogenous GDC thin films with thicknesses of 100–800 nm using corresponding nitrates and chlorides as precursors [32,97–99] and the ultrasonic spray pyrolysis method has been applied for preparation of nanostructured thin films using metal–organic precursors [32,92]. Very few studies can be found for preparation of doped $BaZrO_3$ thin film with spray pyrolysis method [100].

4.5.2. Pulsed laser deposition

Pulsed laser deposition (PLD) method is a physical vapor deposition process, carried out in a vacuum system. The method is based on laser-activated removal of material from the surface of target, and its subsequent collection and deposition onto a substrate [12,101]. High energy densities with an optimum wavelength are absorbed by a small volume of material, resulting in vaporization that is not dependent on the vapor pressure of the constituent cations. Each laser pulse vaporizes a small amount of the material creating a plasma plume, which provides a material flux collected onto the substrate surface. The laser pulse is required to be short in duration, high in energy density and highly absorbed by the target material. In the case of ceramic target, short wavelength lasers operated in the ultraviolet range are most commonly used. High-energy ultraviolet laser pulses can be generated using excimer lasers or frequency-tripled or quadrupled Nd:YAG solid-state lasers. Both single, stoichiometric targets of the material or multiple targets for each element can be used for deposition of multi-cation films [101].

A background gas is often introduced as a reactant (e.g. molecular oxygen for oxides) component of the flux [101]. Oxygen partial pressure with magnitude of 10^{-2} Pa or less is maintained, depending on the tendency for reduction of the deposit [102]. PLD requires temperatures of around 500–700 ºC to deposit high-quality crystalline films [27]. The amount of film growth per laser pulse will depend on multiple factors, including distance between target and substrate, background gas pressure, laser spot size and energy density. Each ablation pulse will typically provide material sufficient for the deposition of a sub-monolayer of the desired phase. Under typical conditions, the deposition rate per laser pulse can range from 0.001 to 1 Å /pulse [101]. Although very high deposition rates up to ~600 μm/h have been reported, however, rates of ~1 μm/h have been more typically employed when high quality, epitaxial thin films are desired [102,103].

PLD method is attractive for its ability to deposit almost any oxide compound regardless of the complexity of the crystal chemistry and preserve the required stoichiometry [27,101]. This method is applicable for deposition of a wide variety of materials, including many with relevance to SOFCs due to the low processing temperature and its capability to produce controlled nano-structures [12,102]. In various works doped ceria thin films with thicknesses of 0.2-5 μm were deposited using PLD method [25,99,104–106].

4.5.3. Magnetron sputtering

Magnetron sputtering is also a physical vapor deposition process. It takes place in an evacuated chamber filled with a sputtering gas at a pressure of 0.4 Pa typically. Typically, argon is used as an inert gas because of its relatively low cost [107]. A large negative voltage is applied to the cathode. The sputtering gas forms a self-sustained plasma, which is shaped with a magnetic field. Physical sputtering of the target occurs, when positive ions from the plasma, which are accelerated in the electric field, strike the target surface [107]. Material ejected by the incident ions is mostly uncharged and moves away from the target. During the transport the particles lose their kinetic energy by thermalization and finally condense on the substrate surface. The sputtering process can dissociate an oxidized target surface. Therefore, the sputtered material may consist of both metal atoms and metal oxide molecules. The metal, metal oxide and oxygen species that arrive at the substrate are adsorbed and they are ultimately incorporated into stable nuclei to form a continuous film. These processes are the major factors determining film chemistry, short-range atom order, crystallography and microstructure. In addition, magnetron sputtering provides ion irradiation of the film during deposition, which has been demonstrated to be important for obtaining high-density films at low temperatures [27]. In most cases, sputtering deposition results in a loss of more volatile material like oxygen from a compound target. Thus, oxygen is often included in the sputter gas mixture even when an oxide target is used, as a means of controlling the metal to oxygen ratio on the target [102,107]. Ceramic thin films may be deposited on various substrate materials. During sputtering the substrate temperature usually does not exceed 70 ºC, although the substrate can be additionally heated [27].

Direct current (DC) magnetron sputtering applies magnetic field, which maintains electrons near the target surface. Using an appropriate arrangement of magnets, the electrons can be made to circulate on a closed path onto the target. The high flux of electrons creates a high density plasma from which ions can be accelerated towards the target. This allows a high sputtering rate with a lower potential and both low and high sputtering pressures. Using pulsed power magnetron sputtering allows dissipation of charge build-up on the target [107]. Radio frequency (RF) sputtering allows use of a non-conductive target or a metal target surface that has become oxidized, because the target is capacitively coupled to the plasma process [27,108]. Typical film growth rates are 0.15–0.5 μm/h and depend on RF power, oxygen partial pressure, bias potential and other parameters. In the case of reactive magnetron sputtering, oxygen is introduced into the deposition chamber, which then reacts with the depositing particles in order to produce an oxide deposit on the substrate. One approach is to employ a single target consisting of an alloy of metals, another is to use multiple targets of the pure metals. By changing the sputtering sources and sputtering parameters, a wide variety of different compositions and structures with specific properties can be obtained. Film deposition rates mainly depend on the oxygen flow-rate. Homogeneous, large-area coatings can be obtained with this method.

Reactive magnetron sputtering with a metal target allows much higher deposition rates (2.5 μm/h) compared with RF sputtering using an oxide target [27,102].

The magnetron sputtering method has been widely applied to deposit a variety of films for different applications, components and protective coatings for SOFC. It is a versatile method that allows excellent control of composition and morphology with low processing temperatures [12,102]. RF magnetron sputtering using an oxide target have been utilized extensively to produce GDC films with thicknesses of 50–850 nm [109–112]. Pulsed DC and RF reactive magnetron sputtering (using metallic targets) have been also applied for deposition of GDC films with thicknesses of 0.3–5 μm [58,68,113,114]. Columnar feature of the film was obtained by using the metallic target. However, no apparent columnar structure was formed by using the oxide target [112]. Doped $BaZrO_3$ films with thicknesses of 200–750 nm have been deposited using RF-sputtering method [115–117].

5. EXPERIMENTAL

5.1. Preparation of $Ce_{0.9}Sm_{0.1-x}Tb_xO_{2-\delta}$ layer

$Ce_{0.9}Sm_{0.1-x}Tb_xO_{2-\delta}$ (x = 0-0.05) (TSDC) layers were deposited using an ultrasonic spray pyrolysis process (SP). The precursor solution was prepared by dissolving stoichiometric amounts of cerium nitrate hexahydrate ($Ce(NO_3)_3 \cdot 6H_2O$, 99.99% trace metals basis, Aldrich), samarium nitrate hexahydrate ($Sm(NO_3)_3 \cdot 6H_2O$, 99.999% trace metals basis, Aldrich) and terbium nitrate hexahydrate ($Tb(NO_3)_3 \cdot 6H_2O$, 99.999% trace metals basis, Aldrich) in mixed tetraethylene glycol (99%, Aldrich) and Milli-Q+ water solution. The volume ratio of water:tetraethylene glycol was fixed at 2:3. The final concentration of the precursor solution (with respect to metal salt) used was 0.1 M [32].

The SP TSDC layers were deposited onto a single-crystal MgO(100) substrate (MgO, Crystal GmbH) with a thermal expansion coefficient close to the one of $Ce_{0.9}Sm_{0.1}O_{2-\delta}$. Lateral dimensions and thickness of the substrate were 10x10 mm and 0.3 mm, respectively. The micro-roughness of the polished working surface was low: R_a<0.5 nm. A MicroSpray ultrasonic atomizing nozzle (120 kHz, flat tip, Sono-Tek Corporation) was used for atomizing the precursor solution. The distance between the nozzle and the substrate was fixed at 12 cm. The precursor solution was delivered to the nozzle by a syringe pump (Sono-Tek Model 997, Sono-Tek Corporation) with a flow rate of 0.15 ml/min. Argon as a carrier gas at a pressure of 10 kPa was used. The substrate was heated on a melted mixture of Pb and Sn metals using the heating plate with the temperature set to 390 °C. The temperature of the substrate was controlled with a surface-mounted K-type thermocouple under carrier gas flow in order to determine its cooling effect. A computer controlled X-Y movement stage combined by two positioning tables driven by a stepper motor along guide rails (T-LSR series, Zaber Technologies Inc.) was used for automated motion of the heated substrate during the spraying sequence in order to ensure the homogenous distribution of the precursor solution on the substrate surface. The ultrasonic spray pyrolysis set-up used is illustrated in Fig. 1. A single spray step with a duration of 130 s was carried out as a preliminary experiment in order to verify the film formation mechanism. A fixed amount (0.485 ml) of precursor solution was sprayed during a single spray step. Due to the assumed cooling effect of the carrier gas, every spray run was stopped for 2 s after every 47 s of deposition during each step and a 5 min pause was left between every spraying step in order to allow the substrate temperature to rise to its initial value. The deposition rate was 479 pm/s. The layers deposited were additionally heated in the middle of the spraying sequence on the molten Pb+Sn bath for 1 h at 500 °C in order to ensure the burn-out of intermediate products [32].

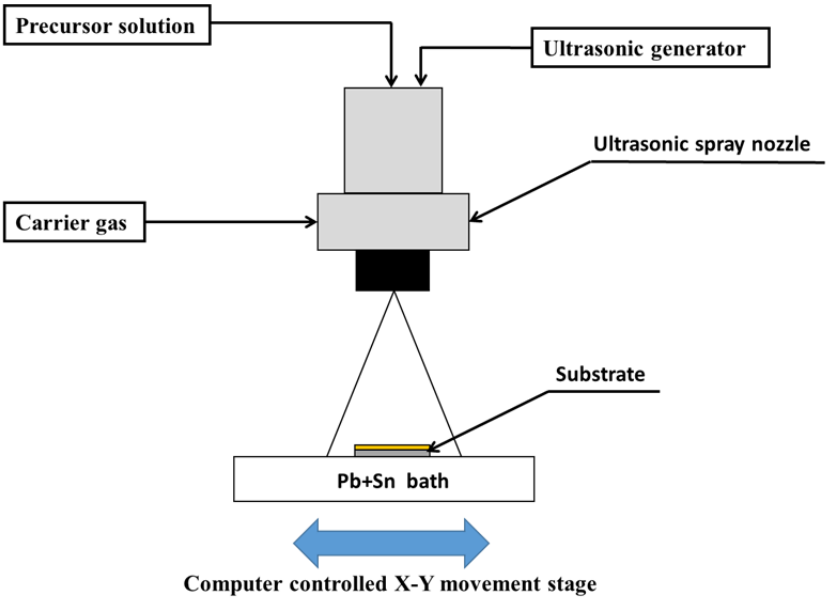

Figure 1. Ultrasonic spray pyrolysis set-up used for electrolyte layer deposition.

As-deposited SP TSDC layers were subjected to heat treatment in a high temperature furnace (HTF 1700, Carbolite). The layers were heated up to a temperature of 600 °C with a heating rate of 1 °C/min in order to ensure smooth burnout of residue compounds, then annealed up to a temperature of 1200 °C with a heating rate of 3 °C/min and thereafter cooled with the rate of 2 °C/min. In the preliminary experiments the temperatures of 900 and 1300 °C were also tested in order to investigate the influence of the sintering temperature on the microstructure of the layer prepared [32].

5.2. Preparation of single cells for analysis of $Ce_{0.9}Gd_{0.1}O_{2-\delta}$ chemical barrier layers

$Ce_{0.9}Gd_{0.1}O_{2-\delta}$ (GDC) barrier layers were deposited onto commercially available yttria-stabilized zirconia (YSZ) electrolyte (Kerafol) and onto Ni-YSZ|YSZ electrolyte half-cell using pulsed laser deposition (PLD), magnetron sputtering (MS) or ultrasonic spray pyrolysis (SP) methods [31].

5.2.1. Preparation of GDC layer using ultrasonic spray pyrolysis

The spray pyrolysis process used was described above. The precursor solution for the deposition of GDC layer was prepared similarly by using cerium nitrate hexahydrate ($Ce(NO_3)_3 \cdot 6H_2O$, 99.99% trace metals basis, Aldrich) and

gadolinium nitrate hexahydrate ($Gd(NO_3)_3 \cdot 6H_2O$, 99.99% trace metals basis, Aldrich). Due to the different thermal properties, the optimized deposition temperature for YSZ and Ni-YSZ|YSZ substrate was 405 and 500 °C, respectively [31].

As-deposited layers were heat treated in a high temperature furnace (HTF 1700, Carbolite). The films were heated up to a temperature of 600 °C with a heating rate of 1 °C/min in order to ensure smooth burn-out of residue compounds. Thereafter the samples were annealed at 950 °C with the heating up rate of 3 °C/min. The dwell time was 5 h. After the heat treatment step the samples were cooled with the rate of 2 °C/min [31].

5.2.2. Preparation of GDC layer using magnetron sputtering

The GDC target for magnetron sputtering was prepared by pressing $Ce_{0.9}Gd_{0.1}O_{2-\delta}$ powder into a 5.1 cm diameter and 2 mm thick disk and sintered at 1453 °C for 5 h. Finally the disk was silver-epoxy glued onto a copper plate. The GDC layer was deposited using a AJA International UHV magnetron sputtering system applying the following parameters: base vacuum $1.33 \cdot 10^{-4}$ mPa, 0.4 Pa Ar+O_2 pressure (Ar flow rate 35 ml/min, O_2 flow rate 1 ml/min), sample temperature 300 °C, 55 W radio frequency (RF) power. The deposition time during a single magnetron sputtering step was 19.6 h. The deposition rate was 5.7 pm/s. To analyze the effect of GDC layer thickness on the electrochemical activity in detail, the deposition step was repeated twice or three times (using some new samples) to obtain thicker chemical barrier layers [31].

5.2.3. Preparation of GDC layer using pulsed laser deposition

A KrF excimer laser (COMPexPro 205, Coherent, wavelength 248 nm, pulse width 25 ns) was used for the ablation of GDC material. The GDC layer was deposited using a laser pulse energy density of 3 J/cm^2 on the GDC target and the repetition rate was 10 Hz. The substrate temperature was 600 °C and the distance between the substrate and the target was fixed at 7.5 cm. Oxygen pressure in the deposition chamber was 0.1 Pa. The deposition rate of complex oxide was 31 pm/s [31].

5.2.4. Heat treatment of GDC layer

The first set of systems with the GDC barrier layers deposited without additional thermal treatment (PLD GDC prepared at 600 °C, MS GDC prepared at 300 °C, SP GDC pre-sintered at 950 °C) were studied. It should be noted that the preparation conditions and consequently the microstructures for as-prepared raw GDC layers vary because the different deposition methods applied require specific deposition regimes. The second set of samples with the GDC barrier

layers was subjected to the same heat treatment conditions by sintering for 3 h at 1300 °C, before printing and sintering of the cathode paste [31].

5.2.5. Preparation of LSC cathode

All differently synthesized and thermally treated Ni-YSZ|YSZ|GDC and YSZ|GDC systems (half-cells) were studied in contact with LSC cathode. The $La_{0.6}Sr_{0.4}CoO_{3-\delta}$ powder was prepared using the thermal combustion of nitrates based solution, where $La(NO_3)_3 \cdot 6H_2O$, $Sr(NO_3)_2$ (all from Aldrich, 99.9%) and $Co(NO_3)_2 \cdot 6H_2O$ (98%, Riedel de Haën) as precursors and glycine (99%, Sigma-Aldrich) as a reducing agent were used [118]. To prepare the viscous electrode pastes, terpineol, dispersant (Solsperse 3000), polyethylene glycol (as a binder) and polyvinyl butyral (as a plasticizer) were used. The LSC cathode printed was sintered at two different temperatures (950 and 1100 °C) in order to analyze the influence of cathode sintering temperature on the mobility of ions during this preparation step. To analyze the effect of GDC layer thickness on electrochemical activity, the LSC cathode was sintered at 1100 °C [31].

5.3. Preparation of single cells for analysis of $BaZr_{0.9}Y_{0.1}O_{3-\delta}$ layer

Thick supportive $BaCe_{0.9}Y_{0.1}O_{3-\delta}$ (BCY) membrane was prepared from powder synthesized using ultrasonic spray pyrolysis method. $BaZr_{0.9}Y_{0.1}O_{3-\delta}$ (BZY) layers were deposited onto these membranes using two different synthesis methods: the cost-effective ultrasonic spray pyrolysis (SP) and more time consuming magnetron sputtering (MS) method [30].

5.3.1. Synthesis of supportive $BaCe_{0.9}Y_{0.1}O_{3-\delta}$ membrane

Stoichiometric amounts of $Ba(NO_3)_2$ (99.95%, Alfa Aesar), $Ce(NO_3)_3 \cdot 6H_2O$ (99.99%, Alfa Aesar) and $Y(NO_3)_3 \cdot 6H_2O$ (99.9%, Alfa Aesar) were dissolved in Milli-Q+ water, whereby the concentration of Ba^{2+} in the solution was 2.5 mM. The solution was nebulized with a ultrasonic particle generator (Sonaer Model 241) applying 2.4 MHz ultrasonic frequency and introduced into a tubular furnace with two hot zones. In the first zone at 600 °C the generated aerosol of salt solution was dried and decomposed partially. In the second zone at 900 °C the salt powder decomposed finally and reacted mostly to form the composite oxide. The formed oxide powder was collected to a filter and calcined at 900 °C to finish the formation of the well-characterized complex oxide. Afterwards de-agglomeration was carried out in isopropanol. Particle size distribution of the powder was obtained using a Microtrac S3500 Bluewave particle size analyzer. Dried powder was pressed to a BCY pellet with diameter of 11 mm using 40 kN force [30].

The BCY pellet was sintered using the following optimized heating schedule: heating up to 400 °C with a rate of 3 °C/min, subsequently the temperature was raised with the rate of 7 °C/min to 1500 °C, where the temperature was held constant for 30 h and then decreased to room temperature with the rate of 2 °C/min. To avoid Ba loss from the surface layer, the sintering of BCY pellet was carried out between porous BCY pellets [30].

5.3.2. Deposition of $BaZr_{0.9}Y_{0.1}O_{3-\delta}$ layer using ultrasonic spray pyrolysis method

The SP BZY layer was prepared using precursor solutions made from $BaCl_2 \cdot 2H_2O$ (99.999%, Alfa Aesar), $Zr(C_5H_7O_2)_4$ (98%, Sigma Aldrich) and $YCl_3 \cdot 6H_2O$ (99.99%, Sigma Aldrich) with stoichiometric proportions. For all the salts the content of crystal water was controlled implementing thermal analysis in oxidizing conditions. Diethylene glycol butyl ether (≥99.2%, Sigma Aldrich) was used as an organic co-solvent in proportional amount with water. The precursor solutions were prepared by dissolving the salts in Milli-Q+ water and then adding the organic solvent to obtain 0.1 M solution. Thereafter the constant stirring for 24 h was applied. YSZ (Kerafol) and BCY substrate were used for the optimization of deposition parameters and preparation of coated membranes, respectively. The precursor solution was sprayed onto the substrate using ultrasonic atomizer (Sonaer 241PG ultrasonic particle generator, 2.4 MHz). Substrate was heated on the molten metal bath (described above) with the temperature fixed at 250 °C. Deposition was carried out applying 60 s long spraying cycles alternately with 60 s long thermal stabilization steps [30].

5.3.3. Deposition of $BaZr_{0.9}Y_{0.1}O_{3-\delta}$ layer using magnetron sputtering method

The MS BZY layer was deposited using a AJA International UHV magnetron sputtering system applying the following parameters: base vacuum $1.33 \cdot 10^{-4}$ mPa, 1.07 Pa Ar+O_2 pressure (Ar flow rate 50 ml/min, O_2 flow rate 5 ml/min), sample temperature was 250 °C, 15 W bias at the sample, 4 h 40 min deposition time and 18 cm distance from targets to the substrate. Reactive sputtering was carried out using simultaneously $Zr_{0.9}Y_{0.1}$ (>99.9%, AJA International) and Ba (99.5%, AJA International) targets with 7.62 cm diameter applying 170 W pulsed DC (3μs, 100 kHz) and 150 W RF sources, respectively. The deposition rate of BZY layer was 42 pm/s [30].

5.4. Physical characterization methods

5.4.1. Thermal analysis

Thermogravimetry (TG) and differential scanning calorimetry (DSC) curves were recorded for the solid salts and precursor solution used in order to study thermal decomposition characteristics in different gas environments. A SETARAM Labsys Evolution 1600 system was used for thermal analysis of solid cerium and terbium nitrates. TG and DSC curves were recorded within the temperature range from 20 to 610 °C with a heating rate of 10 °C/min and gas flow rate of 30 mL/min. The sample amount tested was 20 mg. A SETARAM Setsys Evolution 1750 was used for thermal analysis of the precursor solution. Before analysis the precursor solution was heated in air atmosphere at 80 °C for 3 hours in order to remove the water from the sample, to minimize the mass losses and thermal effects caused by water evaporation. TG and DSC curves were recorded in the temperature range up to 1000 °C with a heating rate of 10 °C/min and gas flow rate of 60 mL/min. The sample amount used was 20 μL [32].

A NETZSCH STA 449 F3 Jupiter system was used for thermogravimetry (TG) and differential thermal analysis (DTA) of barium chloride and zirconium acetylacetonate. 20 μL of salt solution was measured into the ceramic crucible with a volume of 30 μL and was heated up to 1200 °C with a heating rate of 10 °C/min and a gas flow rate of 60 mL/min in 21% O_2 + 79% N_2 gas [30].

5.4.2. X-ray diffraction

XRD analysis of the TSDC and BZY layers was carried out using a Bruker D8 Advanced Diffractometer with Cu Kα1 radiation (λ=1.540596 Å), Vario1 focusing primary monochromator, two 2.5° Soller slits and a LynxEye line detector. XRD patterns were analyzed using DIFFRAC*plus* Topas 4.1 software by Bruker AXS GmbH. The microstrain was determined from full width at half maximum using the Williamson-Hall method [119] after subtracting the instrumental peak broadening contribution. The latter was determined by measuring Al_2O_3 (NIST SRM 1976) data [30,32].

XRD analysis for the GDC barrier layers was performed at room temperature on a materials research X-ray diffractometer (SmartLab, Rigaku^{TM}) using CuKα radiation, poly-capillary focusing optics (CBOf) and a 0.2 mm collimator in θ/2θ scan technique. The X-ray optics enabled to analyze the sample surface in lateral resolution of about 0.3 mm [31].

5.4.3. Atomic force microscopy

The grain size of the SP TSDC layers was analyzed using the atomic force microscopy method on an Agilent Technologies 5500 scanning probe microscope applying the non-contact mode method [32].

5.4.4. Electron microscopy

Scanning electron microscopy (SEM) images of TSDC single deposits, BCY membrane and BZY layer were obtained using a Zeiss EVO® MA 15 scanning electron microscope. A Helios™ NanoLab 600 (FEI) high resolution (HR) scanning electron microscope was used for collection of detailed images with nanoscale features for the TSDC and GDC barrier layers. EDS analysis was carried out from spots with diameter of 15 nm by using a high resolution (HR) transmission electron microscope Tecnai 12 instrument with lateral resolution of <0.2 nm [30–32].

5.4.5. Time-of-flight secondary ion mass spectrometry

The cross sections of all the single cells with GDC barrier layer were analyzed by a time-of-flight secondary ion mass spectrometry (TOF-SIMS, PHI TRIFT V nanoTOF) method before and after the thermal treatment of samples. A positive primary Ga^{+} ion beam and the accelerating voltage of 30 keV were applied. The data were collected within a raster of 10×10 μm. Concentration profiles for Zr^{4+}, Ce^{4+} and Sr^{2+} cations were recorded in GDC and/or YSZ phase [31].

5.5. Electrochemical characterization methods

5.5.1. Four probe DC technique

The total conductivity σ^{tot} of the SP TSDC layers deposited onto MgO substrate were measured at different oxygen partial pressures and temperatures using the conventional four probe DC technique. The experimental setup for precise adjustment of oxygen partial pressure(s) for conductivity measurements was similar as described in reference [120], where 1% H_2 mixture in Ar gas was used with a flow rate of 1.5 ml/min and oxygen was pumped electrochemically through the ScSZ membrane into the gas stream. An oxygen sensor based on a ScSZ membrane with Pt electrodes and an R-type thermocouple was set up with a distance of approximately 5 mm from the sample surface studied. A multichannel Solartron 1470E Cell Test system was used for pumping oxygen for conductivity measurements. The oxygen activity in the gas stream was measured using a Fluke 8846A 6-1/2 Digital Precision Multimeter. Electrical contacts on the 10x10 mm films were made 1 mm wide and with 3 mm distance between voltage measuring electrodes using Pt paste for brush application (Mateck) [32].

5.5.2. Impedance spectroscopy

The cell potential was controlled and electrochemical measurements were performed using a Solartron 1287A potentiostat/galvanostat and a SI 1260 frequency response analyzer. All electrochemical measurements for the single cells with the GDC barrier layers were performed using 20% O_2 + 80% N_2 in cathode gas stream and 97% H_2 + 3% H_2O in anode gas stream. Electrochemical characterization for the supportive BCY membrane and BZY layers was performed in the atmosphere of humidified mixtures of 95% Ar + 5% H_2. Porous electrodes made from platinum paste (Mateck) were used [30,31].

6. RESULTS AND DISCUSSION

6.1. Optimization of ultrasonic spray pyrolysis process

According to the TG curve obtained, the thermal decomposition of $Ce(NO_3)_3 \cdot 6H_2O$ (Fig. 2) in argon atmosphere was mostly complete at 297 °C with a corresponding mass loss of 56%. Complete thermal decomposition of $Ce(NO_3)_3 \cdot 6H_2O$ into ceria is recommended, if the layers deposited are based on ceria. It will help to avoid stress build-up in the layer caused by the continuing decomposition processes. The mass loss value indicated that some nitrates or intermediate products were still present in the samples. The decomposition process of $Ce(NO_3)_3 \cdot 6H_2O$ was endothermic. Switching the gas atmosphere from argon to air did not have any major effect on the nature of the decomposition process [32].

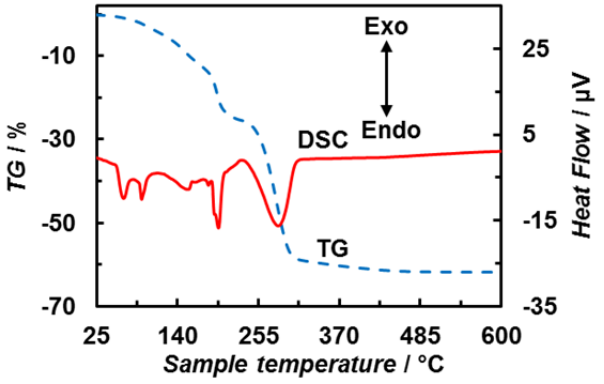

Figure 2. Thermogravimetry and differential scanning calorimetry curves for $Ce(NO_3)_3 \cdot 6H_2O$ in argon.

Using a purely aqueous precursor solution for the deposition process, the layers deposited were cracked with dried droplets occurring all over the surface. Based on the results of previous studies in the field of spray pyrolysis [94,98], tetraethylene glycol was added as the high boiling point solvent in order to suppress the Leidenfrost effect and use sufficiently high deposition temperature ensuring complete decomposition of precursors. According to the TG curve, obtained for the precursor solution used for the deposition of SP TSDC layers (Fig. 3), most of the mass loss (92%) had occurred at below 313 °C, which can be attributed mainly to the vaporization of tetraethylene glycol. However, the final mass loss value 97% at 1000 °C indicated that some nitrates or carbon residues were still present in the sample after the decomposition process. It has been demonstrated by Rupp et al. that residual carbon impurities are inevitably present at temperatures up to 1000 °C in the films deposited using spray pyrolysis method [119].

As opposed to the argon atmosphere, the decomposition of tetraethylene glycol and nitrates in air atmosphere is far more exothermic illustrated by 3 major exothermic peaks in the DSC curve at 294, 310 and 347 °C, respectively (Fig. 3). The more exothermic nature of the decomposition process in the air atmosphere can be explained with the oxygen component in ambient gas promoting an additional oxidative decomposition of the organic solvent. Argon was chosen as carrier gas for the ultrasonic spray pyrolysis process to avoid the additional exothermic effects caused by oxidative decomposition of the organic solvent, which could affect the deposition conditions on the substrate surface [32].

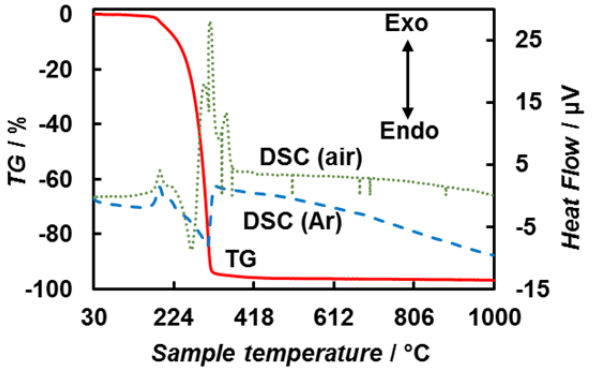

Figure 3. Thermogravimetry and differential scanning calorimetry curves for precursor solution used for deposition of SP TSDC layers in argon and in air.

Thermal analysis revealed that during the deposition process it is critical to maintain the surface temperature of the substrate above 300 °C. At lower surface temperature, the decomposition of main components of the precursor solution, which are the organic solvent and $Ce(NO_3)_3 \cdot 6H_2O$, would not be sufficient during the deposition process. This will result in layer cracking caused by the continuing slow decomposition and drying processes of the material deposited [32].

A single spray step with duration of 130 s, carried out as a preliminary experiment, produced perceptible deposits (Fig. 4) on the heated MgO substrate. The irregular shape of the deposits indicated their possible movement on the substrate due to the evaporation as it has been reported by Muecke et al. [32,98].

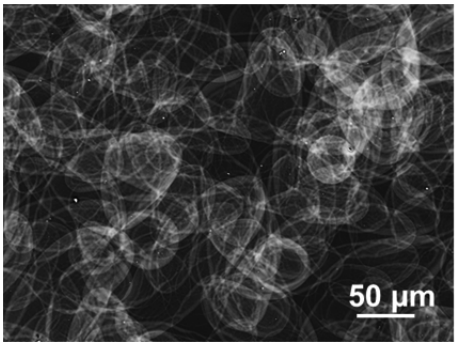

Figure 4. Overall SEM image of deposits formed on the heated MgO substrate as a result of ultrasonic spray pyrolysis process with duration of 130 s.

One critical parameter of the deposition process was the distance between the nozzle and the substrate. Too small distance resulted in too large amount of precursor solution sprayed on the substrate surface. A wet layer was formed, which cracked during drying. Initially the substrate was heated on the surface of heating plate. Great variations occurred in the quality of as-deposited raw layers, when the sample surface was observed from one edge to another. It was concluded that the substrate did not have complete contact with the heating surface and thus, heat-transfer was not even across the sample. Hereafter the substrate was heated on a melted mixture of Pb and Sn metals, which guaranteed a good contact between the substrate and heating surface. Several deposition regimes were tested in which a fixed amount of precursor solution (0.485 ml) was sprayed in a single spray step. Influence of interruptions in the deposition process and the number of deposition steps on the microstructure of layer was then studied (Fig. 5). Blocking the spray for 2 s after every 47 s of deposition during a step prevented delamination of the layer deposited (Fig. 5b). The interruption promoted increase of surface temperature during the process, thus, the additional decomposition of the intermediate products in the material already deposited. Additionally, reducing the number of deposition steps from 16 to 10 ensured obtaining defect-free raw layers (Fig. 5c) with the certain thickness, which is not yet accompanied by stresses exceeding the fracture strength of the material [32,98].

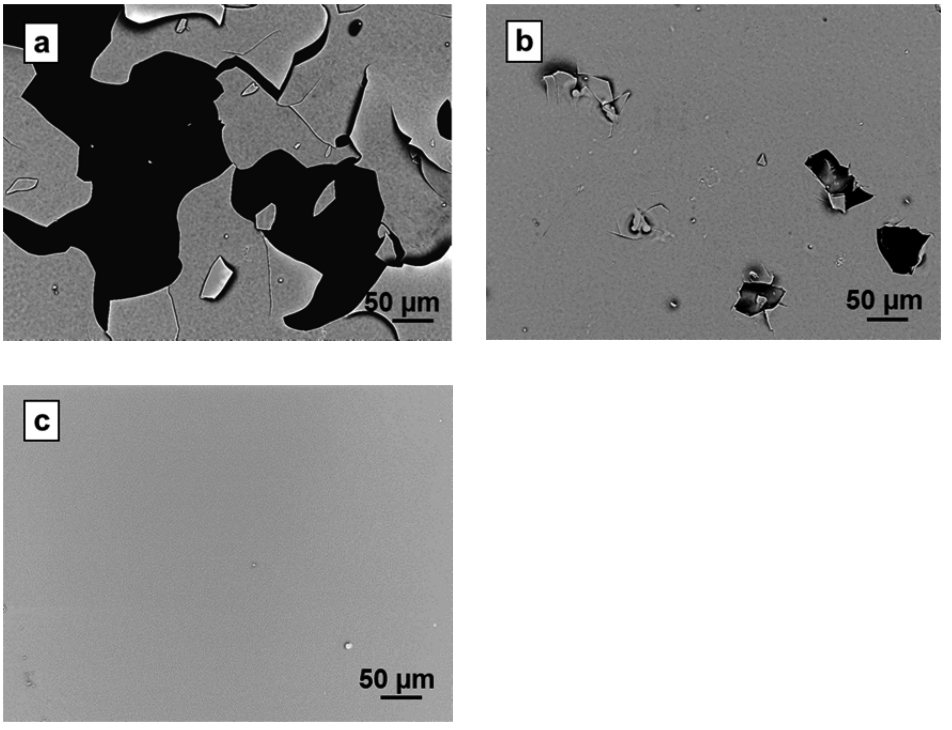

Figure 5. Overall SEM images of as-deposited SP TSDC layers prepared with different deposition regimes: without spray blocking and 16 deposition steps (a), with spray blocking for 2 s and 16 deposition steps (b) and with spray blocking for 2 s and 10 deposition steps (c).

According to the detailed analysis of the SEM data (Figs. 6a and b), crack-free homogenous SP TSDC raw layers with average thickness of 0.96 µm were deposited. After the heat treatment at 1200 ºC the average thickness of the layer was reduced to 0.7 µm (Fig. 6c). The decrease of layer thickness was 27%, which could be attributed to the burn-out of residual species and densification processes at higher temperatures. Good contact between MgO and STDC can be seen and the layers deposited had a crack-free structure with increased grain size (Figs. 6d and e) [32].

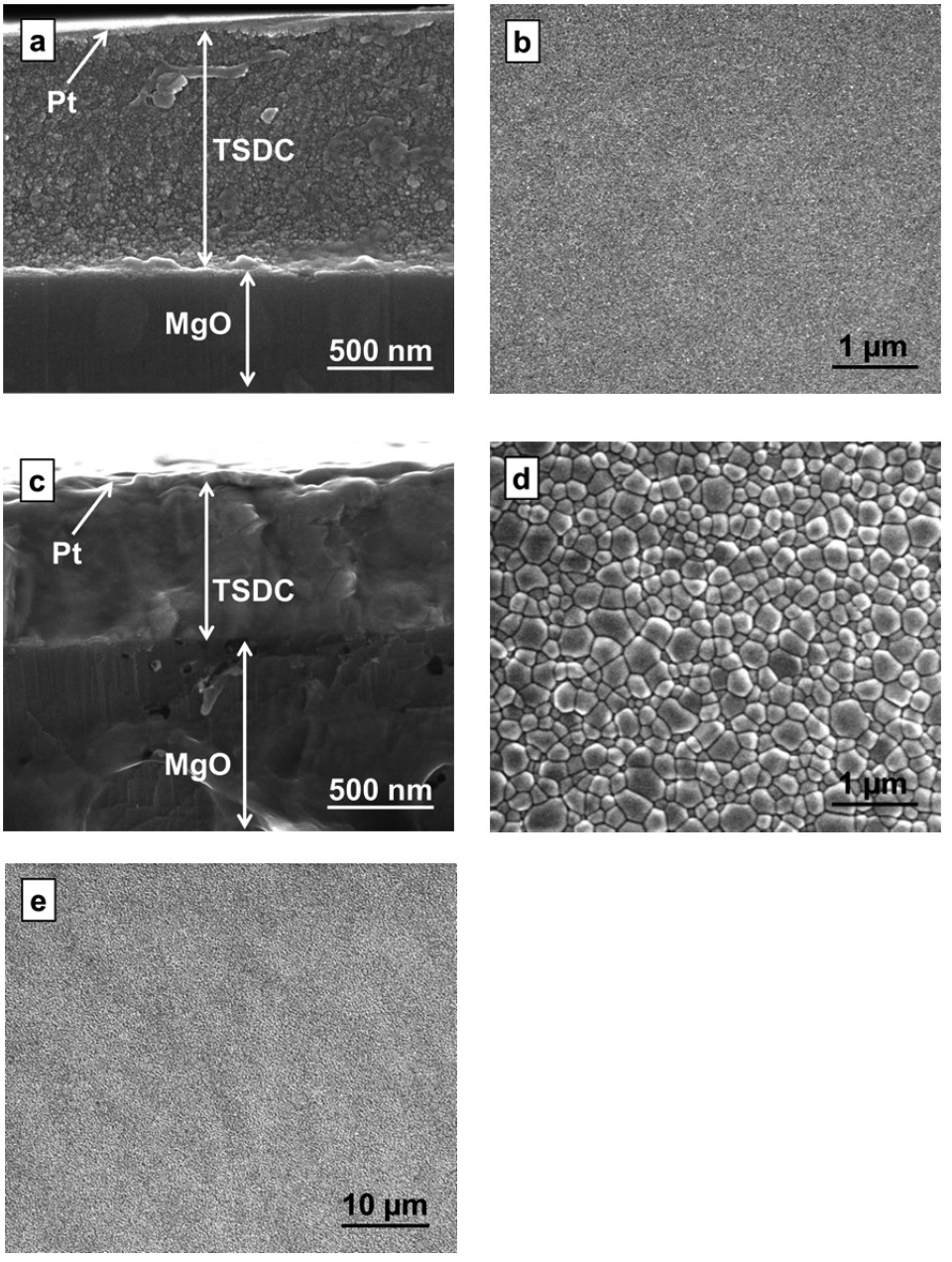

Figure 6. Detailed SEM images of SP TSDC layer deposited onto the MgO substrate: cross-section (a) and surface (b) of as-deposited raw layer, cross-section (c) and surface (d, e) of heat treated (T = 1200 °C) layer.

TG curves obtained for $Zr(C_5H_7O_2)_4$ (Fig. 7) and $BaCl_2 \cdot 2H_2O$ (Fig. 8) indicate that the thermal decomposition process is mostly complete at 530 and 160 °C, respectively. The substrate temperature used for the deposition of BZY layer was fixed at 250 °C, well below the decomposition temperature of $Zr(C_5H_7O_2)_4$, which was one of the main components in the precursor solution.

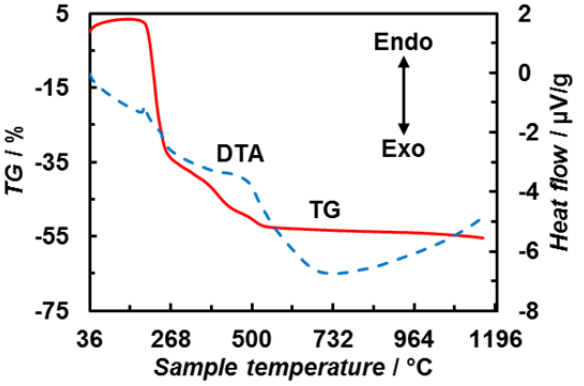

Figure 7. Thermogravimetry and differential thermal analysis curves for $Zr(C_5H_7O_2)_4$ in air.

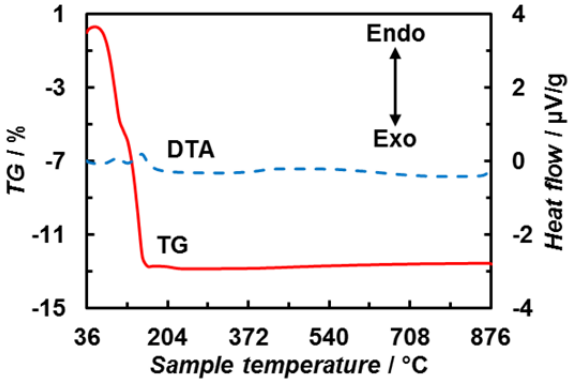

Figure 8. Thermogravimetry and differential thermal analysis curves for $BaCl_2 \cdot 2H_2O$ in air.

Optimization of the deposition process for BZY layer was started with the MicroSpray ultrasonic atomizing nozzle (120 kHz, flat tip, Sono-Tek Corporation). However, the size of droplets generated by this nozzle was sufficiently large, that precipitation of the precursor salts with low solubility occurred before complete evaporation of droplets. The deposits formed were not homogenous. In the next step the precursor solution was sprayed onto the substrate

using the ultrasonic atomizer (Sonaer 241PG ultrasonic particle generator, 2.4 MHz). The droplets generated were smaller by one order of magnitude compared with the ones generated by the MicroSpray ultrasonic atomizing nozzle. Thus, the evaporation of droplets was faster, allowing the formation of deposits with homogenous composition.

As it can be seen from Fig. 9a, raw BZY layer deposited using the ultrasonic spray pyrolysis method (SP BZY) was homogenous and approximately 1.1 μm thick with some surface roughness. In the case of heat treated SP BZY layers, some closed porosity could be observed (Figs. 9b and c). The porosity could be caused by significant amounts of gaseous by-products formed at the following heat treatment step due to incomplete thermal decomposition of precursor salts during the deposition of SP BZY layer. Additionally, the poor sinterability of BZY should be mentioned here [121,122]. The heat treatment at 1150 °C reduced the thickness of BZY layer to 0.7 μm (Fig. 9b) compared with the raw layer, which was most likely caused by the decomposition of some residual carbonaceous compounds. The decrease of layer thickness was 36% [30].

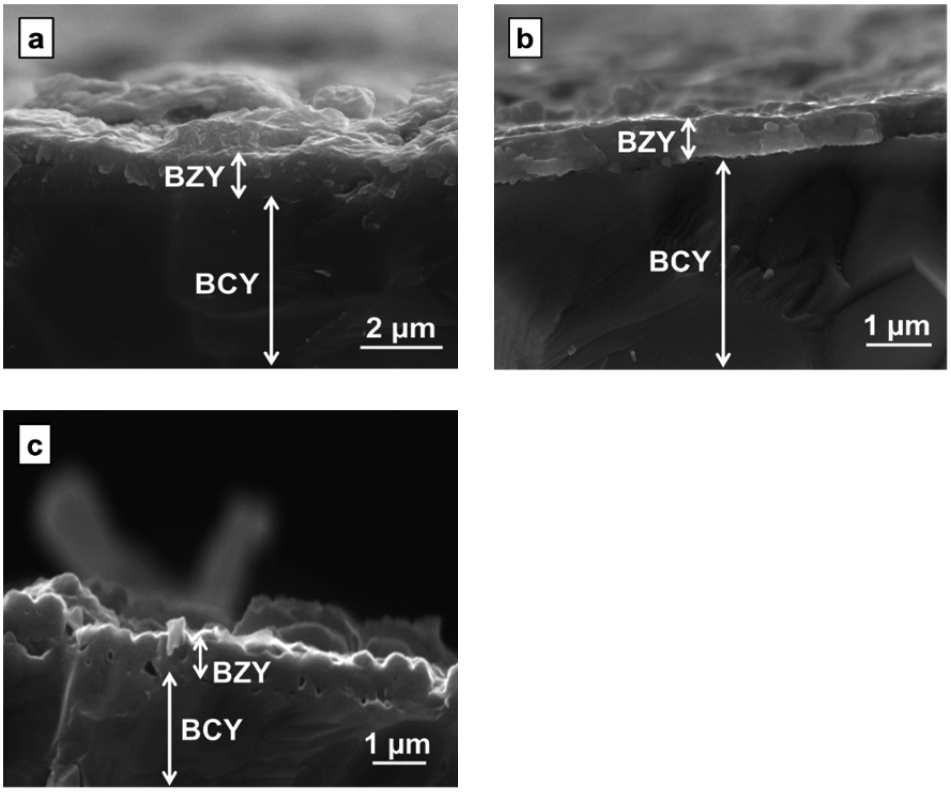

Figure 9. SEM cross-section images of SP BZY layer, deposited onto the BCY substrate: as-deposited raw layer (a), heat treated layer at T = 1150 °C (b) and T = 1350 °C (c).

Thus, the substrate surface temperature is the most important parameter for spray pyrolysis process as it has been mentioned in previous works [93,95]. Kinetics of the thermal decomposition of precursor salts and solution deposited onto the substrate is influenced by the surface temperature. Morphology of layer can be significantly affected by the burn-out processes of precursor species. Unfinished thermal decomposition in the layer has a negative effect on obtaining a ceramic with high density, which is one of the requirements for the SOFC electrolyte.

6.2. Analysis of layer microstructure

The grain diameter in the microstructure of heat treated SP TSDC layers exhibited nearly Gumbel distribution (Fig.10) [32].

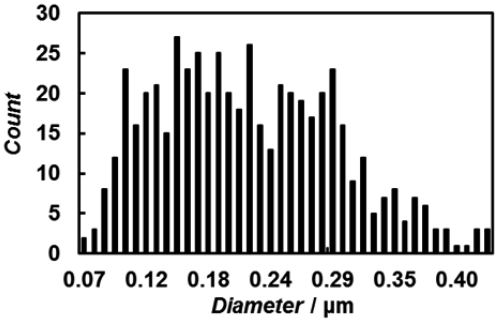

Figure 10. Grain diameter distribution histogram for SP TSDC layer, heat treated at T=1200 °C.

It is a well-known fact that the diffusion based sintering process is temperature dependent and accompanied by thermally activated densification and grain growth in the material. Additionally, the heat treatment causes crystallization of material with reduced concentration of defects in the lattice [83,119]. Although the spray pyrolysis method allegedly allows to obtain amorphous layers, the nanograins in the cross-section (Fig.6a) indicate the onset of the crystallization processes already at the deposition conditions. Higher sintering temperatures resulted in increased size of grain obtained for TSDC, GDC and BZY materials (Table 1).

Table 1. Dependence of grain diameter on heat treatment temperature for the layers deposited using ultrasonic spray pyrolysis method.

Layer type	Heat treatment temperature (°C)	Grain diameter (nm)
SP TSDC	900	25
SP GDC	950	75
SP BZY	1150	110
SP TSDC	1200	210
SP TSDC	1300	360
SP GDC	1300	730

In the case of the SP GDC layer sintered at 1300 °C, the grain growth was anisotropic. Larger grains were developed at the expense of the smaller ones [83]. Although the parameters of heat treatment and properties of materials varied, an obvious tendency can be observed between the grain size and heat treatment temperature. A considerable decrease of grain size from 495 to 360 nm was observed at 1300 °C with increase of Tb content from 0 to 3 mol% (Fig. 11) [32].

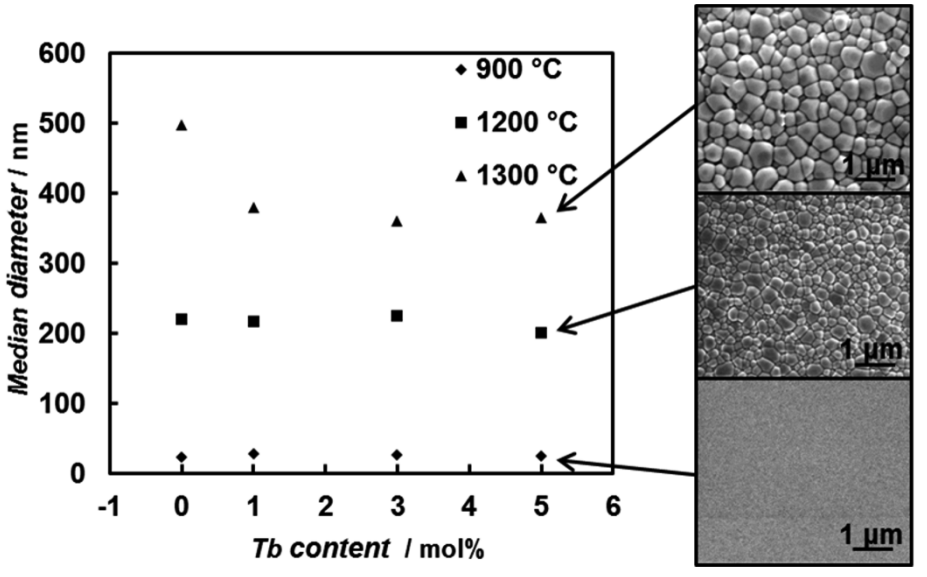

Figure 11. Dependence of grain median diameter on Tb dopant content and heat treatment temperature, given in the figure.

It has been demonstrated in previous works that an increasing amount of dopant has a retarding effect on the sintering of doped ceria [52,123]. The established change in grain size can be explained by the effect of dopant cation and heat treatment temperature on the mobility of grain boundary of ceria. The decrease of grain median diameter with the increase of Tb dopant concentration can be explained with the so-called solute drag effect, which has been previously reported by Rupp et al. [119] and is more effective in the case of a solid solution compared to undoped material. The substitution of Sm as trivalent dopant with Tb, existing both in Tb^{4+} and Tb^{3+} valence states, could decrease the concentration of oxygen vacancies, thus, lowering the cation diffusion, and therefore the mobility of the grain boundary [52,87,124]. The increased microstrain at higher Tb dopant concentration could also be responsible for impeded grain growth similarly as it has been suggested for the doped ceria [52,125]. The decrease of grain size at higher sintering temperatures due to increasing Tb dopant amount can be ascribed to a higher fraction of Tb^{4+} and a resulting increase in microstrain [52]. HR-TEM EDS analysis (Fig. 12) of spots with diameter of 15 nm in the middle of grains and at the grain boundary did not show any differences in the ratios of signal intensities of Ce and Tb [32].

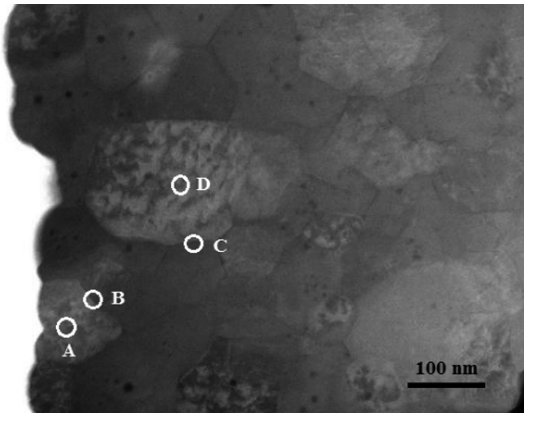

Figure 12. HR-TEM EDS analysis data for TSDC with 5 mol% of Tb dopant. The circles A, B, C and D mark the probed area.

The microstructure of SOFC electrolyte deposited using ultrasonic spray pyrolysis method was influenced both by the heat treatment regime and dopant concentration. Although the grain structure was already present in the as-deposited raw layer, the final grain size was determined by the final heat treatment, which causes the considerable grain growth. The effect of dopant on the layer microstructure was notable at the highest heat treatment temperature, where the grain growth was probably limited by the respective changes in crystal lattice influencing the grain boundary mobility. The final microstructure of

layer can have a considerable effect on the mobility of cations originating from the adjacent SOFC component during heat treatment step, as grain boundary can provide a fast pathway for cation diffusion.

6.3. Analysis of crystal structure

With the increase of the sintering temperature applied, the peaks in the XRD patterns (Fig.13), recorded for the SP TSDC layer with 5 mol% of Tb, exhibited an increase of intensity (compared with the as-deposited SP TSDC layer) referring to higher degrees of crystallinity. There was also a change in orientation of crystal structure with varying the sintering temperature. In the case of the as-deposited raw layer and sintering temperature 900 °C, the highest peak observed corresponds to the (111) plane. However, at sintering temperatures 1200 and 1300 °C used, the (200) peak dominated. A similar tendency in grain orientation dependency on sintering temperature has been previously reported by Rupp et al. [119]. The Tb dopant caused minor shifts in the XRD peaks, indicating changes in the lattice parameters [32].

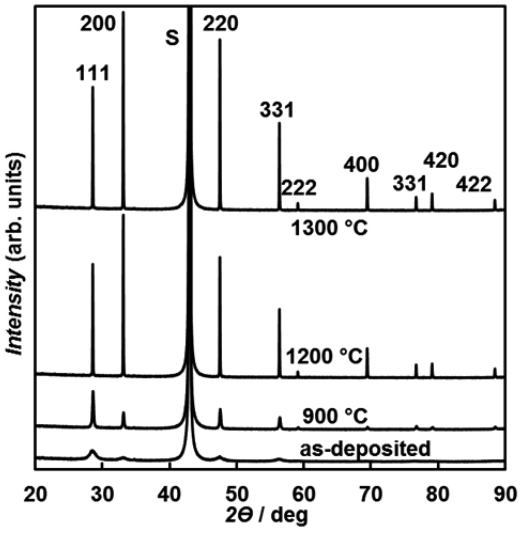

Figure 13. XRD patterns of as-deposited and heat treated SP TSDC layer, respectively (noted in the figure). All the XRD peaks, expect the one labelled with „S“ (substrate), can be attributed to the cubic fluorite structure of ceria.

According to the detailed analysis of XRD data (Fig. 14), the lattice parameter of TSDC decreased from 5.4306 to 5.4109 Å, when the Tb dopant content increased up to 5 mol%. The decrease of lattice parameter is expected due to the different ionic radii of dopants introduced into the ceria lattice. The ionic radii

of Sm^{3+}, Tb^{3+} and Tb^{4+} ions are 1.08, 1.04 and 0.88 Å, respectively [123,126,127]. The microstrain (describing the local variations in lattice spacing and ionic bond lengths [128]), calculated for the SP TSDC layers sintered at 1200 °C, increased with Tb dopant concentration (with an exceptionally high value at the lowest Tb concentration). This effect can be explained with the substitution of Sm as dopant with Tb having a considerably smaller ionic radius. One reason for this effect could be the increasing fraction of Tb^{4+} ions of overall Tb amount having smaller radius compared with Tb^{3+} ions. It has been demonstrated that the fraction of Tb^{4+} ions increases with increasing Tb:Ce ratio and sintering temperature [32,52,54,129].

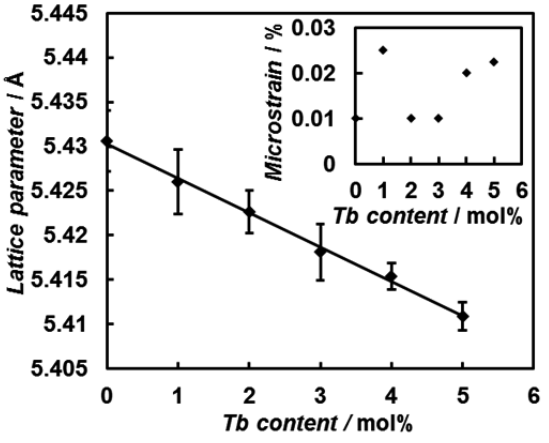

Figure 14. Dependence of lattice parameter and microstrain on Tb dopant content of heat treated (at T=1200 ^{0}C) SP TSDC layer.

The XRD results of the SP BZY layer after sintering at 1150 °C indicated that the lattice parameters were very close to the theoretical reference values. The corresponding lattice parameter values calculated for the SP BZY layers are presented in Table 2 [30]. The lattice parameter for the SP GDC barrier layer sintered at 950 °C decreased after the heat treatment at 1300 °C from 5.413 to 5.360 Å, approaching the standard lattice parameter for bulk GDC. It is a well-known fact that there are some residual stresses in an as-deposited raw layer, which are also affecting its lattice parameter. Post-deposition heat treatment can be used to remove these residual stresses from the layer, resulting in the change of the lattice parameter. The decrease of lattice parameter could be also explained by the substitution of Ce^{4+} ions (0.97 Å) by Zr^{4+} ions with a smaller ionic radius (0.84 Å) in the interlayer [31]. An opposite to this process, where Zr^{4+} ions in the SP BZY layer are substituted by Ce^{4+} ions from the BCY sub-strate, could be the reason for the increase of BZY lattice parameters, when heat treatment temperatures higher than 1150 °C were applied (Table 2) [30]. The ionic substitution between different phases initiated cation mobility.

Table 2. Dependence of lattice parameters of BZY on heat treatment temperature for SP BZY layer.

	Lattice parameter (Å)		
Phase	1150 °C	1250 °C	1350 °C
$BaY_{0.1}Zr_{0.9}O_{3-\delta}$ (100)	4.197	4.204	4.213
$BaY_{0.1}Zr_{0.9}O_{3-\delta}$ (110)	2.968	2.973	2.979
$BaY_{0.1}Zr_{0.9}O_{3-\delta}$ (111)	2.424	2.427	2.432
$BaY_{0.1}Zr_{0.9}O_{3-\delta}$ (200)	2.098	2.102	2.107
$BaY_{0.1}Zr_{0.9}O_{3-\delta}$ (210)	1.877	1.880	1.884
$BaY_{0.1}Zr_{0.9}O_{3-\delta}$ (211)	1.714	1.716	1.720
$BaY_{0.1}Zr_{0.9}O_{3-\delta}$ (220)	1.484	1.488	1.490

The XRD data obtained confirmed the effect of dopant on the lattice parameter and microstrain of the SP TSDC layers. Heat treatment caused the increase of crystallinity and change of orientation in the crystal lattice. The lattice parameters changed also with the increasing heat treatment temperature, which can be ascribed to the relaxation of residual stresses or cation interdiffusion between different phases.

6.4. Cation mobility

Diffusion of cations has been studied using the HR-SEM and TOF-SIMS methods for the SP GDC barrier layers and SP BZY layers deposited onto the YSZ and BCY substrates, respectively. When the LSC cathode was sintered at 950 °C, a slight accumulation of Sr was detected in the interface between YSZ and GDC (Figs. 15a and 17a) in the case of the raw SP GDC barrier layer, which had, without the additional sintering, a fine-grained structure (Fig. 16). When the cathode sintering step at 1100 °C was carried out with the raw SP GDC barrier layer, the mobility of Sr^{2+}, Ce^{4+} and Zr^{4+} ions increased significantly finalizing with a remarkable accumulation of Sr into the interface between YSZ and GDC and in the GDC phase (Figs. 15b and 17b) [31].

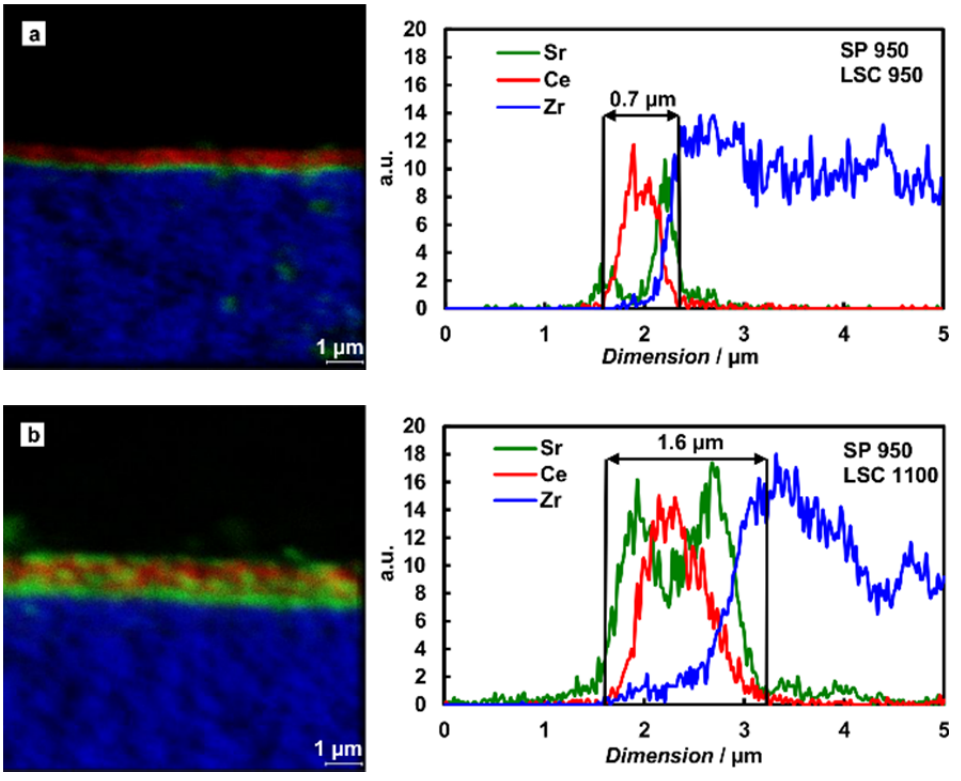

Figure 15. TOF-SIMS distribution maps and element profiles for YSZ|SP GDC systems heat treated at 950 °C with LSC cathode sintered at 950 °C (a) and 1100 °C (b).

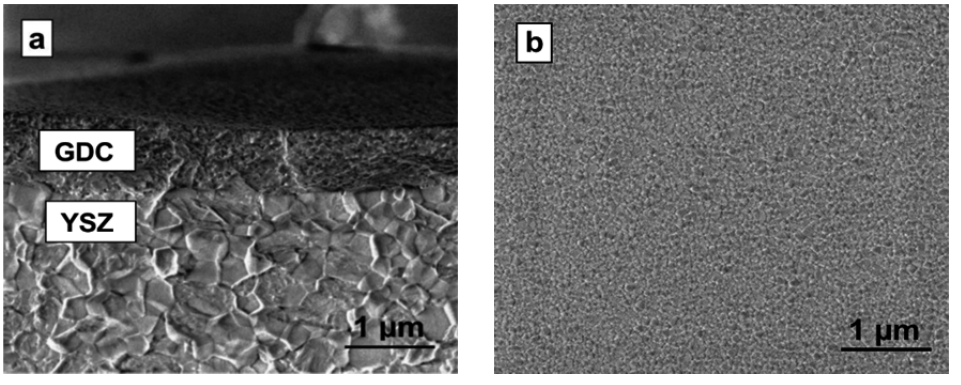

Figure 16. SEM images of raw SP GDC layer: cross-section (a) and surface (b) of layer.

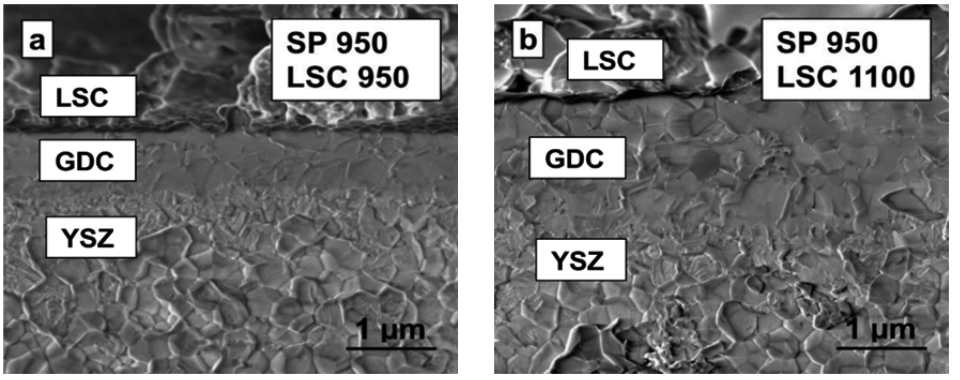

Figure 17. SEM images of YSZ|SP GDC system heat treated at 950 °C with LSC cathode sintered at 950 °C (a) and 1100 °C (b).

The high-temperature treatment had a significant influence on the structure and behaviour of the SP GDC barrier layer. If a non-sintered SP GDC barrier layer was used, then the mobility of Zr^{4+}, Sr^{2+} and Ce^{4+} ions has been established at both cathode sintering temperatures (950 and 1100 °C) (Figs. 15a and b). After the heat treatment at 1300 °C the visible thickness of the SP GDC barrier layer increased (Fig. 18a) from 0.7 to 1.1 μm because of the diffusion of Zr^{4+} ions into GDC with sub-micrograiny structure (Fig. 16) and Ce^{4+} ions into YSZ [31].

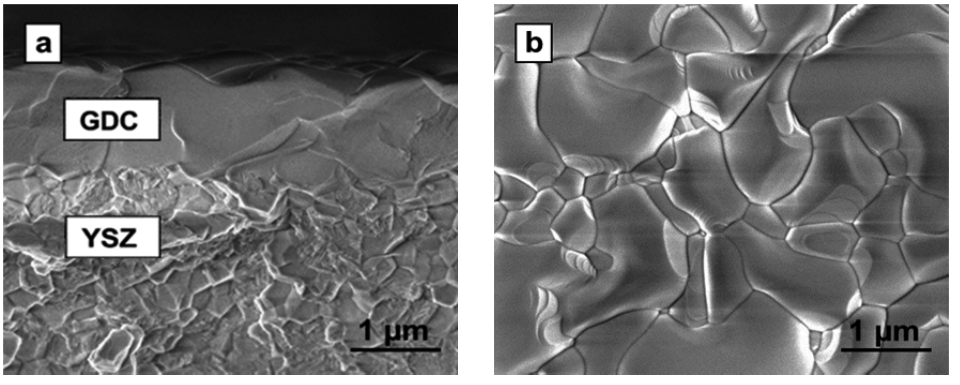

Figure 18. SEM images of SP GDC layer heat treated at 1300 °C: cross-section (a) and surface (b) of layer.

The heat treatment of the SP GDC barrier layer at 1300 °C enhanced Sr blocking effect in the case of the LSC cathode sintered at 950 °C (Fig. 19a). It can be explained by decreased amount of grain boundaries (less pathways for the Sr diffusion) due to the anisotropic grain growth in the SP GDC barrier layer (Fig. 18b). If the heat treatment of the SP GDC layer was carried out at

1300 °C, followed by the LSC cathode sintering at 1100 °C, a significant increase of barrier layer thickness was observed (Fig. 20b). The increase of SP GDC barrier layer thickness was 121%. It was most likely caused by the mobility (mass transfer) of Zr^{4+} ions into GDC and Ce^{4+} ions into YSZ (Fig. 19b) and the formation of $SrZrO_3$ crystallites into the GDC barrier layer or less conductive solid solution between YSZ and GDC. No intensive Sr accumulation at the interface between GDC and YSZ was established (Fig. 19b). It is likely that the relatively high concentration of Zr^{4+} ions in the GDC phase "consumes" mobile Sr^{2+} ions and Sr does not arrive to the YSZ interface to form denser $SrZrO_3$ layer. The diffusion of Sr into the GDC barrier layer was accompanied by microstructural changes in the GDC and also in YSZ phase. Two distinctive sub-layers are occurring in the case of the SP GDC barrier layers sintered at 1300 °C with the LSC cathode sintered at 1100 °C (Fig. 20b). According to the TOF-SIMS data, the smoother sub-layer at the YSZ|GDC interface contains mainly Zr^{4+} and Ce^{4+} ions (Fig. 19b). A slightly coarser layer on top also contained a significant amount of Sr^{2+} ions. The presence of Ce seems to lead to a smoother texture (bigger grains) of YSZ [31].

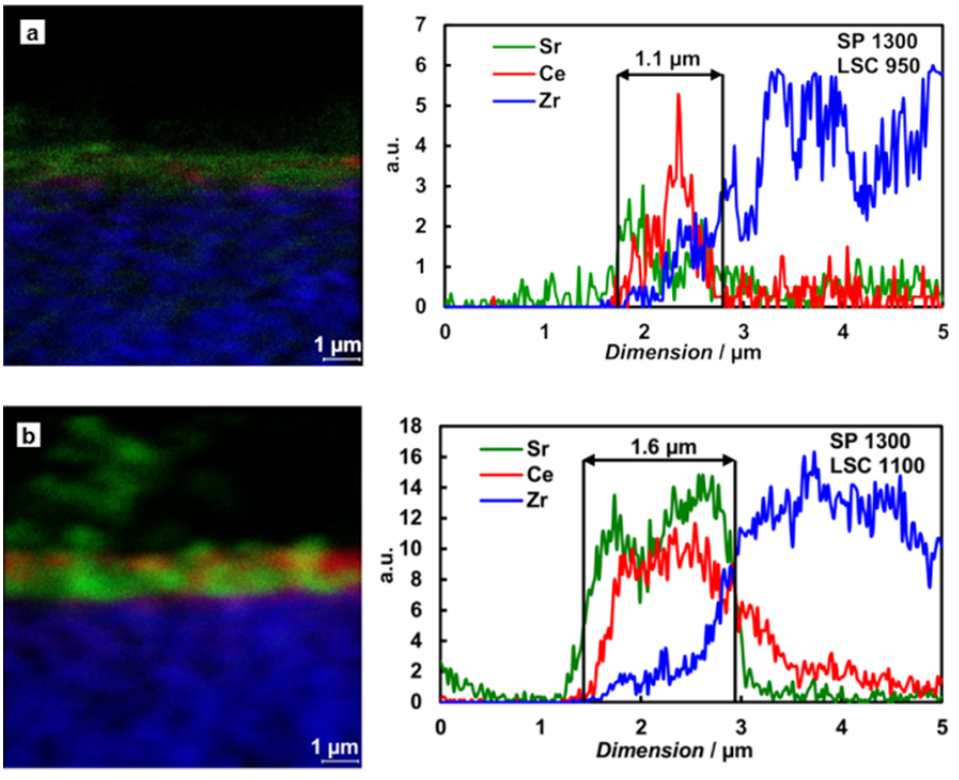

Figure 19. TOF-SIMS distribution maps and element profiles for YSZ|SP GDC systems heat treated at 1300 °C with LSC cathode sintered at 950 °C (a) and 1100 °C (b).

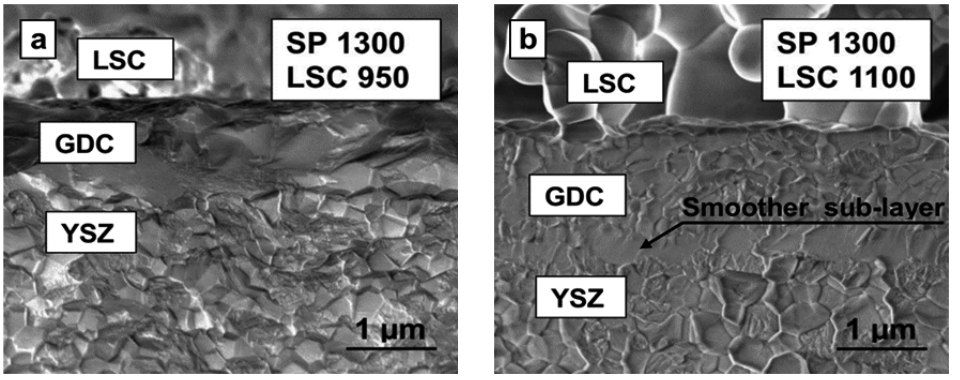

Figure 20. SEM images of YSZ|SP GDC systems heat treated at 1300 °C with LSC cathode sintered at 950 °C (a) and 1100 °C (b).

The XRD patterns for the SP GDC barrier layer with the LSC cathode heat treated at 1100 °C contained four new reflections at the angles of 30.8, 44.1, 54.7 and 64° (2θ), respectively, (Fig. 21) that can be attributed to the cubic $SrZrO_3$ or the cubic $Sr_2LaZrO_{5.5}$. Both phases are equally probable because their distinctive reflections at about 36 and 38° (2θ) are too weak for reliable identification [31].

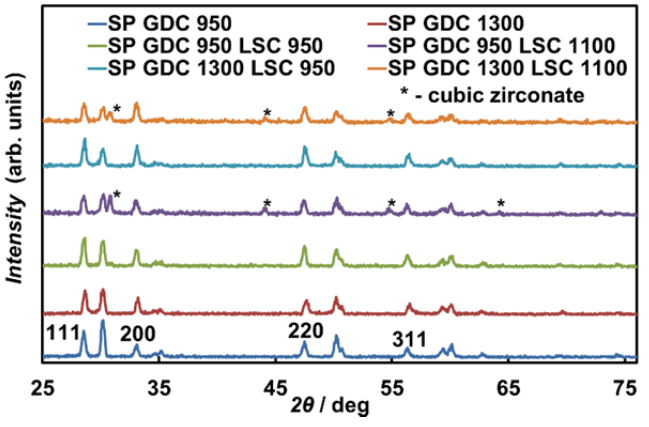

Figure 21. XRD patterns of YSZ|SP GDC systems with LSC cathode. Processing conditions and Miller indexes of four reflections presenting GDC phase are given in the figure.

Diffusion of Ce^{4+} and Zr^{4+} ions between the BZY and BCY phases was confirmed by the results of TOF-SIMS analysis obtained for the cross-sections of BCY|BZY systems heat treated at temperatures $T \geq 1150$ °C. At lower temper-

atures the active interdiffusion was not observed. These results are in good accordance with Fabbri et al. [81] who found that at 1100 °C there is no segregation of BZY and BCY phases [30].

The TOF-SIMS data obtained demonstrated the influence of GDC barrier layer microstructure and heat treatment on the cation mobility. A fine-grained structure (characteristic of the spray-pyrolyzed layer after a moderate heat treatment) facilitated the efficient Sr diffusion during the cathode sintering due to the large fraction of grain boundaries. The diffusion was more intensive, if the sintering was carried out at higher temperature. The grain growth, achieved with the additional high-temperature treatment, effectively suppressed the Sr mobility in the case of moderate sintering temperature for the cathode. The high-temperature treatment was accompanied by the increase of layer thickness and formation of sub-layers in some cases. The mixing of cations from the protective layer and its support was observed at high heat treatment temperatures, confirmed previously by the XRD data.

6.5. Comparison of different deposition methods

While the visible thickness of the SP GDC barrier layer increased after the heat treatment at 1300 °C, the thickness of the PLD and MS GDC layers decreased (Figs. 22a, 22b, 23a and 23b) from 0.7 to 0.6 μm and from 0.4 to 0.2 μm, respectively. The reason for this was probably a slight densification of the PLD GDC layer and a significant densification of the MS GDC layer as a result of the additional heat treatment. On the other hand the average thickness of as-deposited MS BZY layer (approximately 0.7 μm) (Fig. 24) did not change during the heat treatment, which indicates its high density. It should be mentioned that the reactive sputtering method was used for the deposition of MS BZY layer, which was not the case for the MS GDC barrier layer [31].

While the surface of the SP GDC layer annealed at 950 °C exhibited the fine-grained structure (Fig. 16b), the surface of the raw PLD and MS GDC barrier layers was smooth and the microstructure of the substrate can be observed (Figs. 22c and 23c). As in the case of the SP GDC layer, the heat treatment at 1300 °C caused the grain growth for both the PLD and MS barrier layers (Figs. 22d and 23d) [31].

Lattice parameters obtained for the MS BZY layer heat treated at 600 °C were similar to the ones of SP BZY layer [30]. On the other hand, the GDC barrier layers deposited using different methods had non-matching lattice parameter values (Table 3). The dependence of lattice parameter on the synthesis method of GDC have been previously discussed by Rupp et al. [31,128].

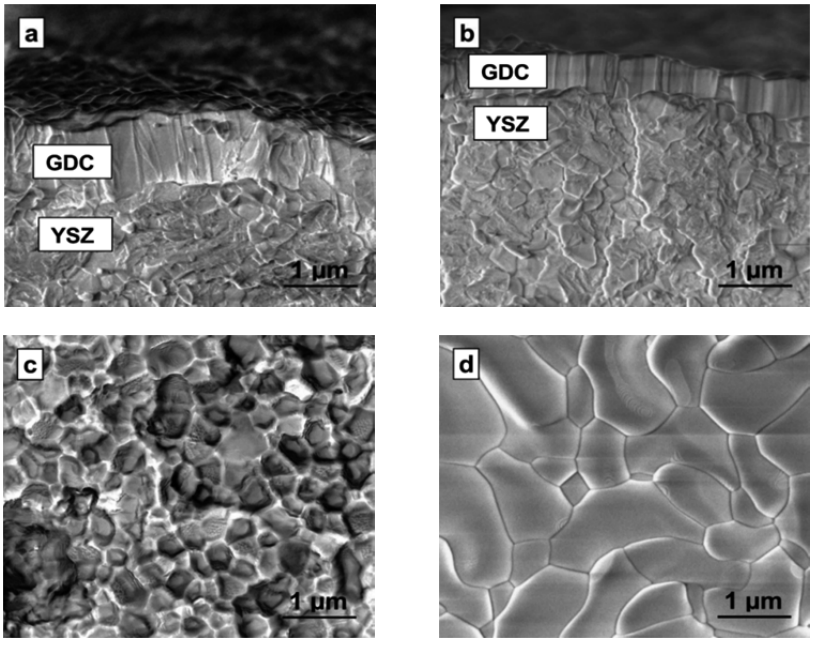

Figure 22. SEM images of PLD GDC layer: cross-section of raw (a) and heat treated (T=1300 ^{0}C) (b) layer, surface of raw (c) and heat treated (T=1300 ^{0}C) (d) layer.

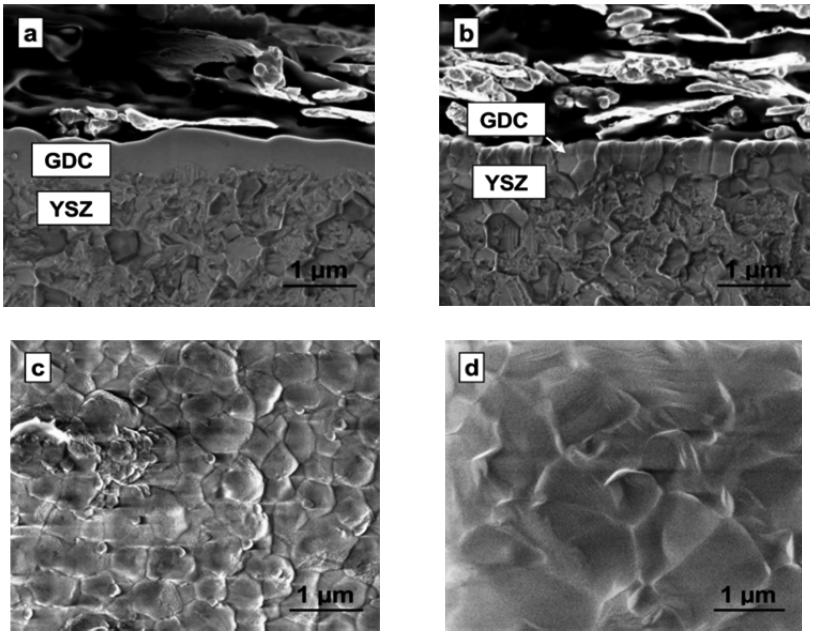

Figure 23. SEM images of MS GDC layer: cross-section of raw (a) and heat treated (T=1300 ^{0}C) (b) layer, surface of raw (c) and heat treated (T=1300 ^{0}C) (d) layer.

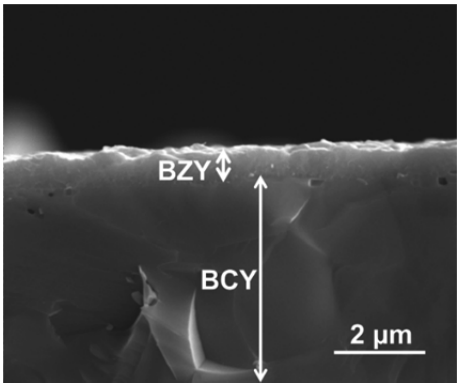

Figure 24. SEM cross-section image of MS BZY layer.

Table 3. Lattice parameter values calculated for the SP, PLD and MS GDC barrier layers.

	Lattice parameter (Å)	
GDC layer type	Raw layer	Heat treated at 1300 °C
SP GDC	5.413	5.360
PLD GDC	5.430	5.400
MS GDC	5.490	5.320

Although the PLD and MS GDC barrier layers were macroscopically quite homogenous (Figs. 22c and 23c) compared with the SP GDC barrier layer before the additional high-temperature treatment at 1300 °C, the sintering of the LSC cathode at 950 °C caused the Sr diffusion into the YSZ|GDC interface (Fig. 25e) in the case of the MS layer. A significant decrease of MS GDC barrier layer thickness (Figs. 26e and f) during the heat treatment of the LSC cathode at 950 °C as well as at 1100 °C suggests again the poor density of the as-prepared MS GDC barrier layer. The PLD GDC barrier layer as the densest one behaves during the LSC cathode thermal treatment at 950 °C as a relatively effective mass transfer blocking barrier (Fig. 25a). As in the case of the SP GDC barrier layer, the cathode sintering temperature of 1100 °C resulted in a remarkable accumulation of Sr at the YSZ|GDC interface and in the GDC phase (Figs. 25b and f), when the GDC barrier layers deposited using the PLD and MS methods were not additionally heat treated at 1300 °C [31].

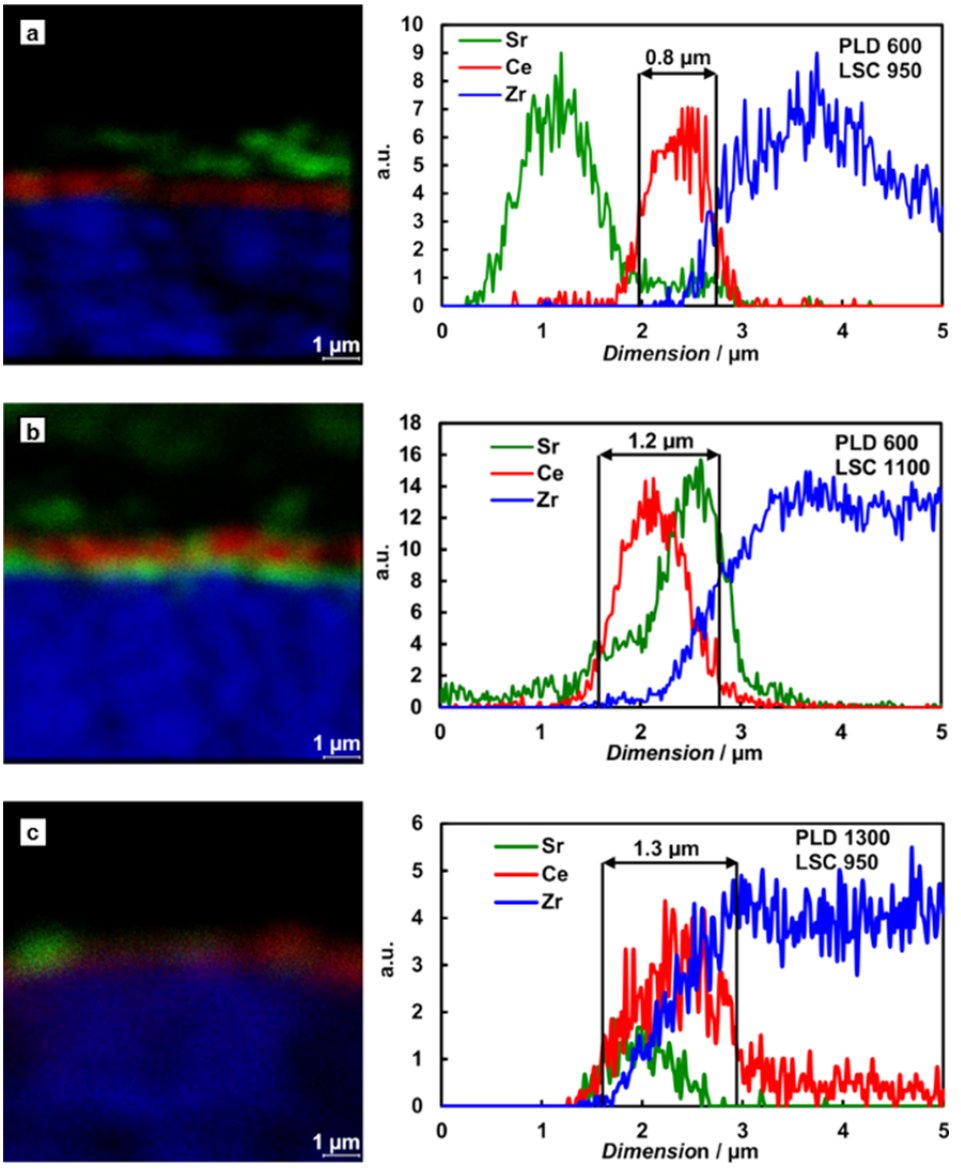
a
1 µm
Sr
Ce
Zr
0.8 µm
PLD 600
LSC 950
a.u.
Dimension / µm
b
1 µm
Sr
Ce
Zr
1.2 µm
PLD 600
LSC 1100
a.u.
Dimension / µm
c
1 µm
Sr
Ce
Zr
1.3 µm
PLD 1300
LSC 950
a.u.
Dimension / µm

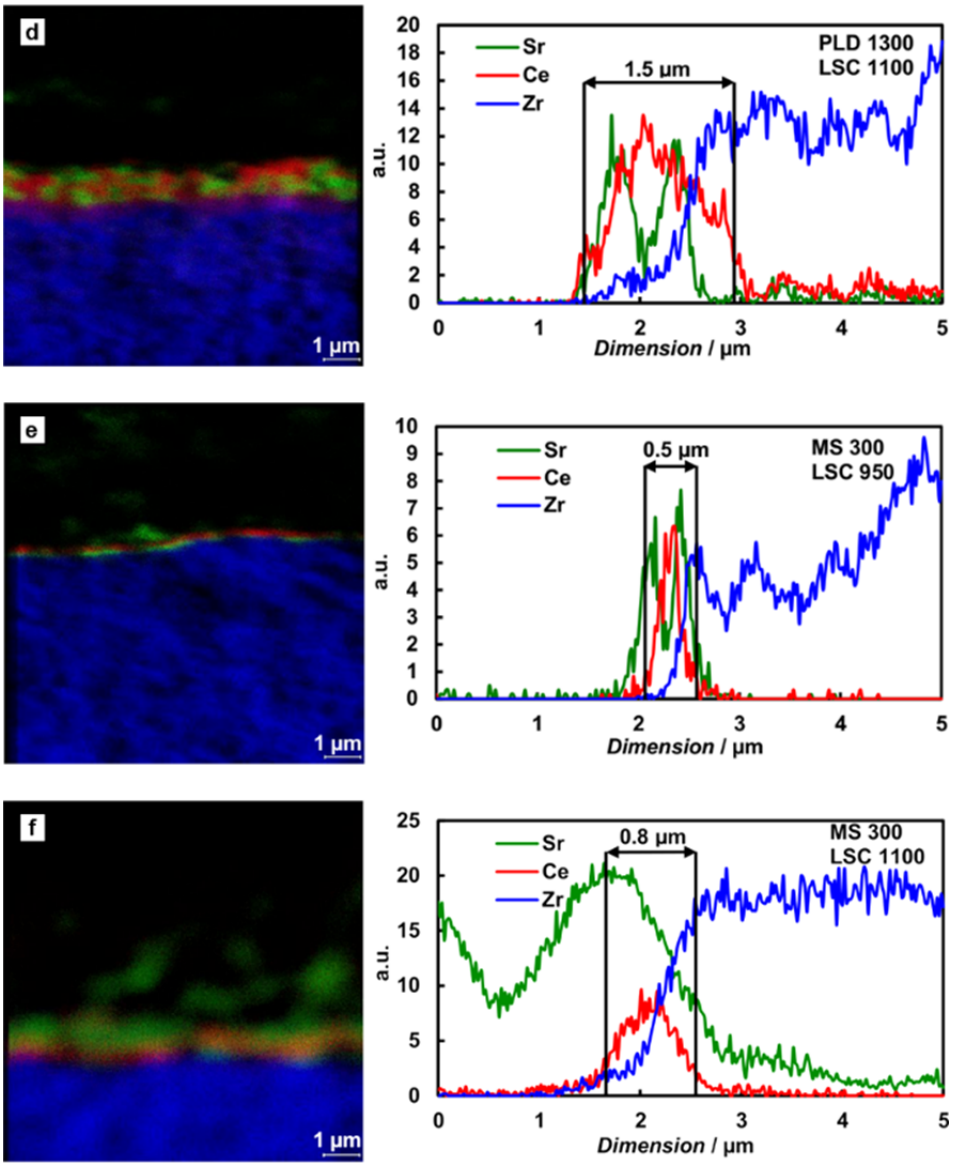
d
1 µm
Sr
Ce
Zr
1.5 µm
PLD 1300
LSC 1100
a.u.
Dimension / µm
e
1 µm
Sr
Ce
Zr
0.5 µm
MS 300
LSC 950
a.u.
Dimension / µm
f
1 µm
Sr
Ce
Zr
0.8 µm
MS 300
LSC 1100
a.u.
Dimension / µm

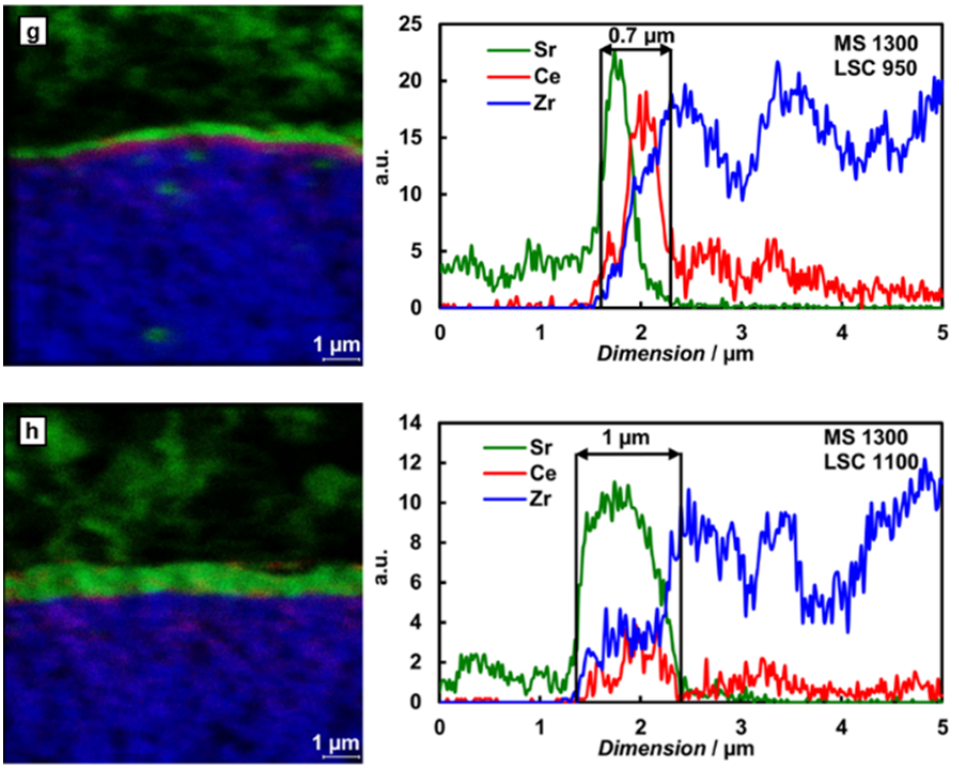

Figure 25. TOF-SIMS distribution maps and element profiles for YSZ|GDC systems with LSC cathode: YSZ|PLD GDC|LSC (a-d), YSZ|MS GDC|LSC (e-h). Processing conditions are given in the figure.

If the heat treatment of the GDC layer was carried out at 1300 °C followed by the cathode sintering at 1100 °C, a significant increase of barrier layer thickness was observed (Figs. 26d and h). The increase of thickness was 114 and even 175% for the PLD and MS GDC barrier layer, respectively. The increase of SP GDC barrier layer thickness was 121%, which was comparable with the one observed for the PLD GDC barrier layer. The additional heat treatment at 1300 °C had the same positive influence on the behaviour of MS GDC barrier as in the case of the SP GDC barrier layer, if the heat treatment temperature for the LSC cathode was limited to 950 °C (Figs. 25g). The PLD GDC barrier layer was already effective without the additional heat treatment (Fig. 25a), which resulted only in mixing of Zr^{4+} and Ce^{4+} ions in the YSZ|GDC interface (Fig. 25c) [31].

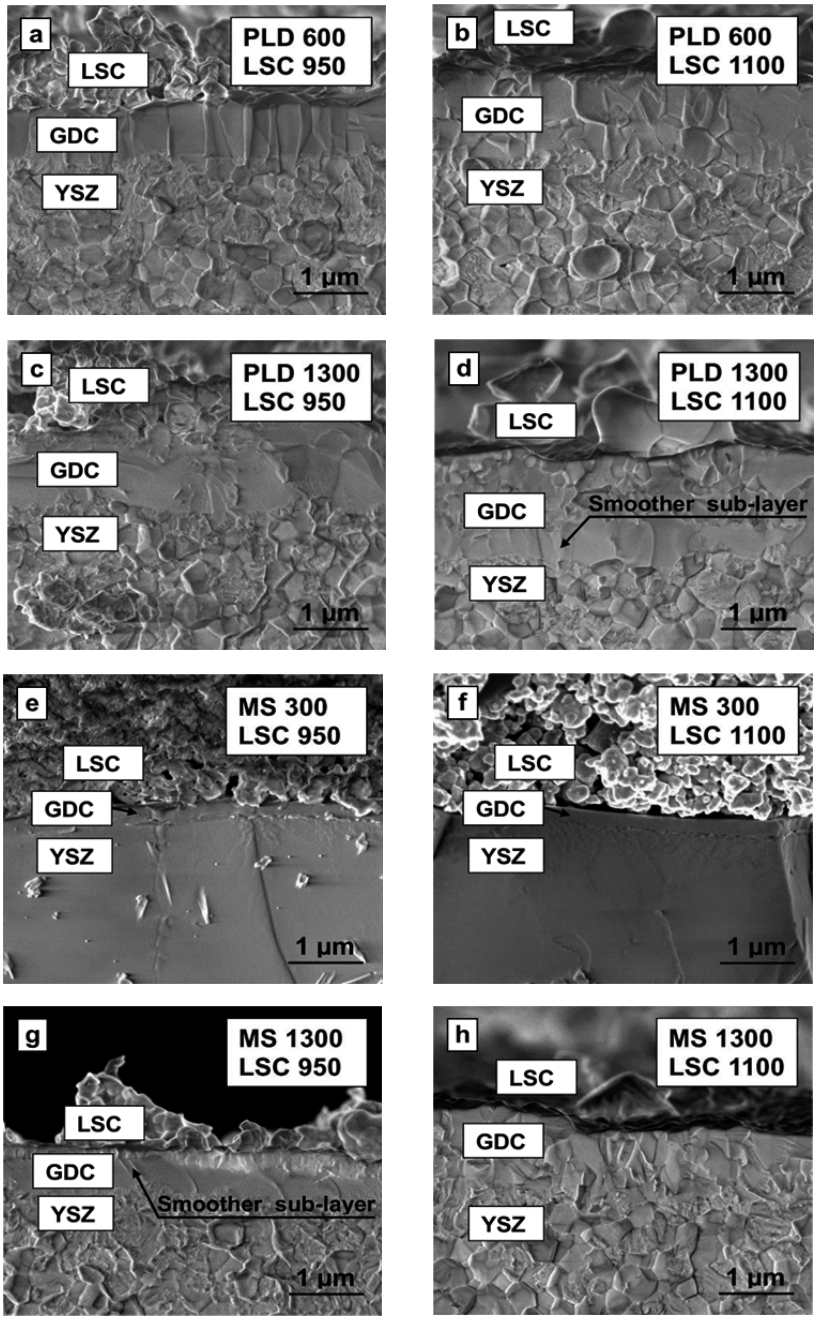

Figure 26. SEM images of YSZ|GDC systems with LSC cathode: YSZ|PLD GDC|LSC (a-d), YSZ|MS GDC|LSC (e-h). Processing conditions are given in the figure.

As in the case of the SP GDC barrier layer, two distinctive sub-layers were also occurring in the PLD GDC barrier layer heat treated at 1300 °C with the LSC cathode sintered at 1100 °C (Fig. 26d). A distinctive smooth sub-layer appears similarly between YSZ and Sr rich MS GDC barrier layer sintered at 1300 °C with the LSC cathode sintered at 950 °C (Figs. 25g and 26g). When the LSC cathode was sintered at 1100 °C, the cations were homogenously distributed throughout the MS GDC barrier layer (Fig. 25h) [31].

As in the case of the samples prepared using the SP method, the XRD patterns for the PLD and MS GDC barrier layers with the LSC cathode heat treated at 1100 °C indicated the formation of the cubic $SrZrO_3$ or cubic $Sr_2LaZrO_{5.5}$ (Figs. 27). Additionally, the sample with the MS GDC barrier layer and the LSC cathode heat treated at 1300 and 950 °C, respectively, showed a weak reflection at 30.8°, confirming the formation of the new $SrZrO_3$ or $Sr_2LaZrO_{5.5}$ phase (Fig. 27b). This observation can be explained by the lower thickness and density of the MS GDC barrier layer, compared with the SP and PLD barrier layers, resulting in a higher diffusion rate of Zr into and through the GDC phase [31].

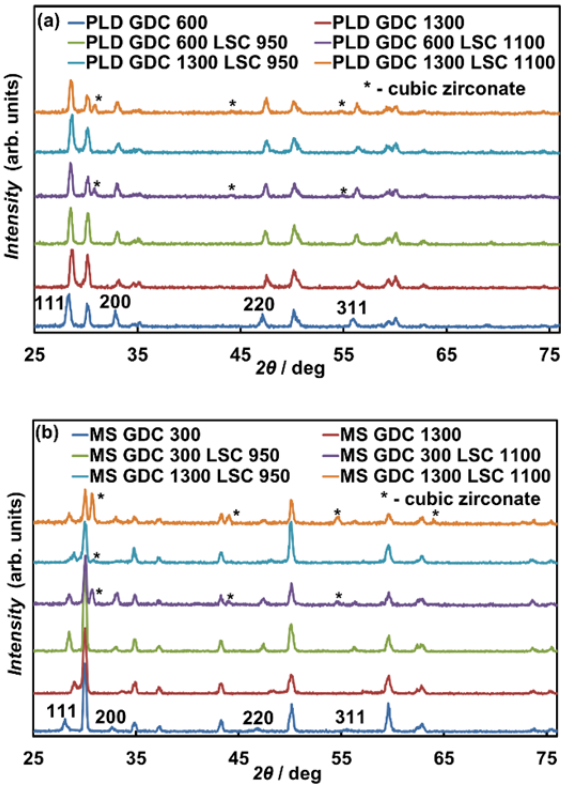

Figure 27. XRD patterns for YSZ|GDC systems with LSC cathode: YSZ|PLD GDC|LSC (a), YSZ|MS GDC|LSC (b). Processing conditions and Miller indexes of four reflections presenting GDC phase are given in the figure.

The comparison demonstrated that opposite to the SP GDC barrier layer the as-deposited PLD and MS GDC barrier layers did not have the fine-grained structure. This difference in the microstructures can explain the opposite behaviour of the PLD and MS GDC barrier layers during high-temperature treatment, where instead of the phase mixing the final layer thickness was determined by the densification. The overall effect of high-temperature treatment on the Sr mobility was similar, irrespective of the deposition method used, although some exceptions occurred in the case of the MS GDC barrier layer treated additionally at high temperature with the cathode sintered at 950 °C.

6.6. Influence of protective layers on electrical performance

6.6.1. TSDC layers

The experimental data obtained (log σ^{tot} vs. log a_{O_2} dependencies) was fitted to the curve calculated using Eq. 5 with a flexible exponent value n. The results obtained are given in Fig. 28 [32].

$$\sigma^{tot} = \sigma_{ion} + \sigma_{el}^{0}(pO_2)^{-n} \tag{5}$$

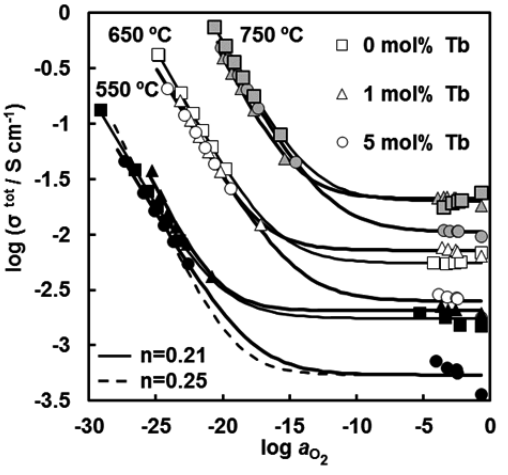

Figure 28. Dependence of total conductivity of SP TSDC layers on the oxygen activity at different temperatures and Tb concentrations, presented in the figure. Dashed and solid lines describe fitting results for different n values. Shape of the symbols in the figure indicates Tb concentration.

Activation energy (seeming) values for ionic (from fitting and from experiment at pO_2 = 0.21 atm) and electronic contribution for the SP TSDC layers with varying Tb concentration were obtained and are presented in Fig. 29. The activation energy of the ionic contribution depends on the Tb concentration. The

minimal value of activation energy at the lowest Tb concentration (1 mol%) can be explained with the suppression of oxygen vacancy ordering caused by the co-doping [130]. The activation energy increases at higher Tb concentrations. Similar dependence was observed for $(Ce_{0.85}Sm_{0.15})_{1-x}Tb_xO_{2-\delta}$ [131] and has been explained with the formation of associates between $V_O^{\cdot\cdot}$ and Tb'_{Ce} as well as Sm'_{Ce} at higher Tb concentrations resulting in a decrease in the concentration of $V_O^{\cdot\cdot}$. Another reason for the increase of activation energy could be the decrease in the concentration of $V_O^{\cdot\cdot}$ with the increase of Tb^{4+} amount [32,52,54].

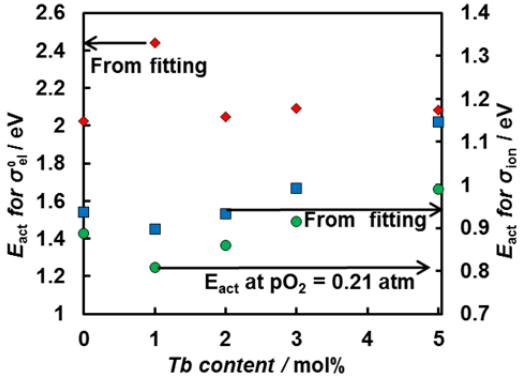

Figure 29. Dependence of activation energy E_{act} calculated for ionic (E_{act} for σ_{ion}) and electronic (E_{act} for σ^0_{el}) conductivity of SP TSDC layer on Tb concentration.

The difference between the activation energy values of ionic conductivity, based on the fitting results and experimental data at fixed pO_2 = 0.21 atm, is caused by the downward deviation of experimental results compared with the fitting values at high oxygen partial pressures (Fig. 28). This tendency increases with the increase of Tb concentration and decrease of temperature. At the highest Tb concentration and at the lowest temperature the decrease of conductivity is approximately half an order of magnitude, very similar to the results presented by Yoo et al. [51]. One possible reason could be related to the oxygen incorporation process into the lattice at high oxygen partial pressures [51,132], leading to the consumption of oxygen vacancies ($V_O^{\cdot\cdot}$) and formation of electron holes ($h^{\cdot}$) in the Sm-doped ceria system without Tb dopant, given as Eq. 6:

$$1/2O_2 + V_O^{\cdot\cdot} = O_O^x + 2h^{\cdot} \quad (6)$$

If the Tb'_{Ce} defects are present in the lattice, it is possible that they trap the electron holes, resulting in the formation of Tb^x_{Ce} species and shifting the reaction in

the direction of vacancy consumption. The dependence of the onset and magnitude of p-type conductivity on temperature at high oxygen partial pressures in doped ceria [132] and the higher decrease of conductivity at higher Tb concentrations support this approach (Fig. 28) [32].

The electronic activation energy for the SP TSDC layer (Fig. 29) does not depend on the Tb concentration or has a very slight tendency to increase at higher Tb concentrations. A significantly higher electronic activation energy value was obtained for the lowest Tb concentration (1 mol%). This interesting electrical behaviour of the layer with the lowest Tb concentration is difficult to explain based on the data currently available, but is confirmed by the XRD data (Fig. 14), where an exceptional microstrain value (statistically reproducible) has been obtained for the SP TSDC layer with 1 mol% Tb [32].

The highest electronic activation energy value for the SP TSDC layer with the lowest Tb concentration is confirmed to be meaningful also in context of the temperature dependence of the lower bound of the electrolytic domain P_n (Fig. 30), where P_n is defined as oxygen activity (atm) at the point, where the ionic conductivity is equal to the electronic conductivity. P_n of the SP TSDC layer with 1 mol% Tb is one order of magnitude lower compared with the SP TSDC layer with 0 mol% Tb at 750 °C. However, the activation energy of ionic conductivity for 1 mol% Tb layer is relatively similar with the ionic activation energy values for the SP TSDC layers containing 0 mol% and 2 mol% Tb. Thus, the lower P_n might appear only if the electronic conductivity is strongly suppressed and its activation energy is high, as we see in the case of the SP TSDC layer with 1 mol% Tb. Further increase of Tb concentration leads to shifting of P_n to the higher oxygen partial pressures, which seems to be caused mainly by an increase of ionic activation energy and a decrease of ionic conductivity, whereas the electronic activation energy remains constant.

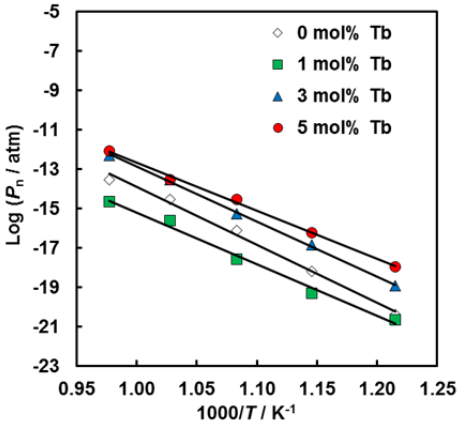

Figure 30. Lower bound of electrolytic domain vs. reciprocal temperature for SP TSDC layers with Tb concentrations given in the figure.

Considering the changes in crystal lattice and coinciding changes in microstrain and electrical properties, the role of Tb as co-dopant introduced in quite small amounts (1 mol%) must be emphasized, as it enhances the protective properties of the SP TSDC layer by shifting the lower bound of the electrolytic domain towards lower oxygen activity by up to one order of magnitude. It should be stressed that the activation energy values and lower bound of the electrolytic domain are characteristics of the SP TSDC layers studied as having specific composition and microstructure [32].

6.6.2. GDC barrier layers

The high-frequency series resistance $Z'(\omega\rightarrow\infty)=R_s$ values calculated from the impedance spectra (Fig. 31a) depend noticeably on the deposition method as well as heat treatment temperature of GDC barrier layers used for their deposition on the Ni-YSZ|YSZ half-cells. The R_s value for the single cell containing the SP GDC barrier layer heat treated at 1300 °C and the LSC cathode sintered at 950 °C was approximately 20% higher compared with the one obtained for the PLD GDC barrier layer with the same treatment, which exhibited the most lowest R_s value. Approximately 30% higher R_s value was measured for the single cell containing the raw PLD GDC barrier layer and the LSC cathode sintered at 950 °C. Electrochemical performance of the single cells containing the GDC barrier layers without the additional sintering at 1300 °C with the LSC cathode sintered at 1100 °C was the lowest. The single cell with the raw MS GDC barrier layer and LSC cathode sintered at 1100 °C exhibited a slightly higher R_s value compared with the one containing the raw PLD GDC and LSC cathode sintered at 950 °C. The single cell with the SP GDC layer heat treated at 950 °C and LSC cathode sintered at 1100 °C demonstrated the highest series resistance R_s value (Fig. 31a). The lower performance of the SP GDC barrier layer could be related to its characteristic fine-grained microstructure, which enabled more efficient cation diffusion throughout it. The single cells prepared using the higher cathode sintering temperature exhibited the lowest O_2 electroreduction activity. Comparison of the data (Figs. 31b and c) demonstrates very low influence of the applied cell potential on the total polarization resistance R_{pol} values. Thus, the slow rate-determining step was most likely controlled by a slow mass transfer rate [31].

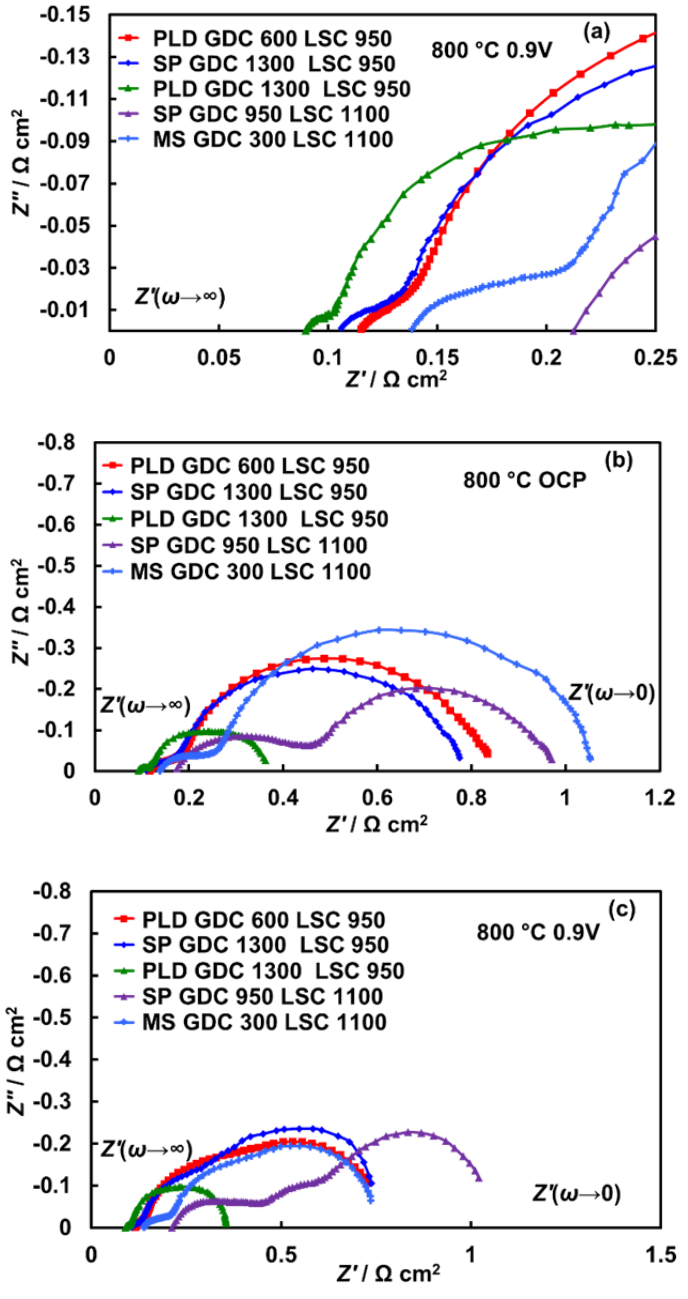

Figure 31. Nyquist plots for differently synthesized and thermally treated GDC barrier layers based single cells at T=800 °C: at E=0.9 V in high-frequency range (a), at OCP (b) and at E=0.9 V (c). Synthesis method, thermal treatment temperatures and cathode sintering temperatures are given in the figure.

Cell potential and current density (*E, I*) curves (Fig. 32) show that the open circuit potential (within experimental potential measurement errors) was practically independent of the barrier layer properties, i.e. independent of the method used for the deposition of GDC onto the half-cell (Ni-YSZ|YSZ) surface. Power density dependencies on the GDC barrier layer as well as LSC cathode preparation and heat treatment conditions coincided with the tendencies of the R_s values calculated using the impedance data. Relatively low power density (*P*) values were measured for the single cells containing the as-deposited SP GDC barrier and LSC cathode sintered at 1100 °C. The additional heat treatment of SP GDC barrier layer at 1300 °C and lowering the cathode sintering temperature to 950 °C somewhat increased the power density value. The PLD deposition method completed with the high-temperature (1300 °C) heat treatment step and moderate (950 °C) cathode sintering step resulted in the best single cell with the highest power density accompanied by the lowest R_s value [31].

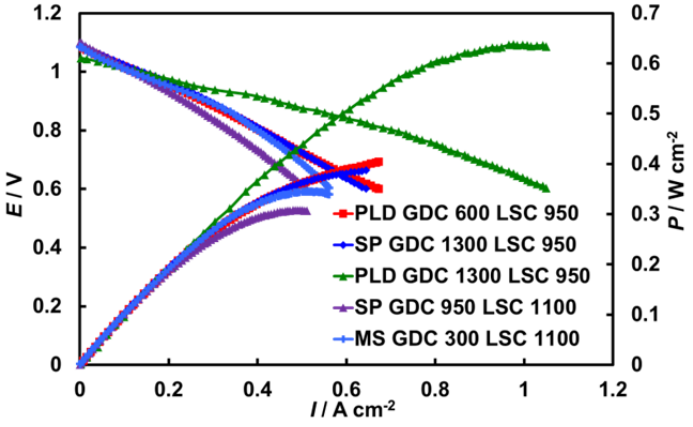

Figure 32. Cell potential and power density vs. current density plots for differently synthesized and thermally treated GDC barrier layers based single cells. Synthesis method, thermal treatment temperatures and cathode sintering temperatures are given in the figure.

In good accordance with the impedance data, the influence of the GDC barrier layer sintering temperature on the Sr mobility is very well visible in TOF-SIMS pictures (Figs. 15, 19 and 25). When the LSC cathode was sintered at 950 °C onto the SP GDC barrier layer heat treated additionally at 1300 °C, some Sr mobility was observed (Fig. 19a), but the electrochemical performance was relatively good and not much influenced by the small concentration of Sr in the barrier layer. However, the PLD and MS GDC barrier layers with the same heat treatment exhibited larger resistance to the Sr mobility in the case of LSC cathode sintered at 950 °C (Figs. 25c and g) [31].

Single cell performance was also influenced by the thickness of GDC barrier layer. The increase of GDC layer thickness from 0.7 to 1.4 µm decreased R_s value nearly 35% (Fig. 33). At the same time, R_{pol} value decreased nearly 60%, demonstrating that the increase of the GDC barrier layer thickness had a positive effect on the O_2 electroreduction rate. However, further increase of GDC barrier layer thickness had a less pronounced influence. As it could be seen in Fig. 33, the layer thickness between 1.4 to 2.1 µm is nearly sufficient and further increase of GDC layer thickness did not decrease the high-frequency resistance as well as the total polarization (charge transfer) resistance value for the system under discussion. Thus, charge transfer resistance was very strongly influenced by the thickness of GDC barrier layer. In the case of too thin barrier layer, the mobility of Sr and Zr was more intensive causing the contamination of YSZ|GDC interface, GDC|LSC interface as well as at the three-phase boundary for LSC cathode, GDC barrier layer and O_2 phase by the formation of $SrZrO_3$ or mixed phases (demonstrated in Figs. 21 and 27 by the XRD data) [31].

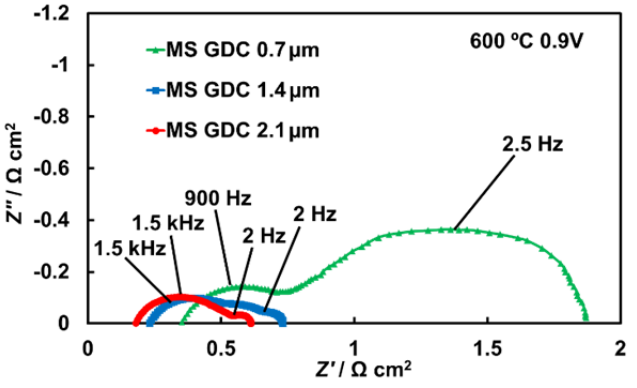

Figure 33. Dependence of single cell impedance on thickness of GDC barrier layer at T=600 °C and E=0.9 V. LSC cathode was sintered at 1100 °C.

In general, the results of the electrochemical tests are in good accordance with the results obtained using XRD, TOF-SIMS and SEM analysis and show that better homogeneity and higher thickness of the GDC barrier layer prevents the mobility and accumulation of Sr onto/into the interlayer between GDC and YSZ electrolyte. The as-deposited SP GDC barrier layer was the most susceptible to cation diffusion probably because of its fine-grained microstructure. The additional high-temperature treatment somewhat suppressed the cation mobility by reducing the fraction of grain boundary in the layer. The growth of $SrZrO_3$ crystallites in the GDC layer during the high-temperature (1300 °C) treatment is probably less harmful than the accumulation of Sr rich layer onto the interface of GDC and YSZ layers, which initiates the formation of relatively dense non-conductive $SrZrO_3$ layer [31].

6.6.3. BZY layers

In the Arrhenius plots constructed for the BCY|BZY samples typically two characteristic linear regions were detected. This behaviour indicates that processes with different nature take place at temperature ranges with different slopes. Several previous studies [133,134] have proposed that the low temperature process (at temperatures ~400–600 °C) is characteristic of the proton conduction behaviour, while the mixed conduction of protons and oxide ions takes place at higher temperatures [30].

All activation energies presented in this work (Table 4) are characteristic of proton conduction process in temperature range from 550 to 650 °C. Total activation energy value for proton mobility in BCY was 0.35 eV, which was also obtained by Fabbri et al. [81]. The influence of BZY layer on the total activation energy was very low, showing tendency to slight increase when the layer was heat treated at a very high temperature (1350 °C), where the interdiffusion of Zr^{4+} and Ce^{4+} ions and mixing of BCY and BZY phases occurred. The activation energy values for bulk process $E_{a,bulk}$ in the bilayer membranes, sintered at 1350 °C, were slightly higher compared to $E_{a,bulk}$ for BCY. This phenomenon could be explained by the fact that too high heat treatment temperatures can lead to formation of $BaCe_{0.9-x}Zr_xY_{0.1}O_{3-\delta}$ phase, which at certain x values have higher activation energies [135]. If Zr starts to dissolve from BZY into the surface of BCY, a layer with certain stoichiometry and higher activation energy is probably formed at certain depth [30].

Activation energies for proton mobility in grain boundary region $E_{a,gb}$ were slightly higher for the systems sintered at lower temperatures (600 and 1150 °C) and lower for the systems sintered at 1350 °C. Very strong influence of grain size on the grain boundary resistance in the case of BZY samples has been described in several studies [74,136] and it was suggested to be related to the effect of grain size on the conduction properties of grain boundary region. Specific conductivities calculated for BCY substrates with and without the BZY layer used in this work are presented in Table 4. Variation of conductivity by one order of magnitude as a function of grain boundary structure of material is a well-known phenomenon and has been studied in details in the case of BZY [30,137].

Stability test was carried out for differently deposited and heat treated BZY barrier layers at 700 °C in CO_2 atmosphere. When the BZY barrier layer was sintered at 600 or 1150 °C, the formation of $BaCO_3$ and CeO_2 was not observed. The formation of $BaCO_3$ and CeO_2 crystals occurred when the BCY substrate or BCY substrate with the BZY barrier layer, sintered at 1350 °C, were used. This behaviour confirms the chemical stability of BZY barrier layer in CO_2 atmosphere, if the BZY and BCY phases are not mixed. Based on these experiments, it can be accentuated that the sintering of BZY barrier layer on top of BCY at higher temperatures than 1150 °C is not possible without the loss of BZY protective properties [30].

Table 4. Activation energies characteristic of processes at temperature range from 550 to 650 °C and specific conductivities at 600 °C measured in 4.8% H_2 + 3% H_2O + 92.2% Ar atmosphere.

Substrate	$E_{a,bulk}$ (eV)	$E_{a,gb}$ (eV)	$E_{a,tot}$ (eV)	σ (S cm^{-1})
BCY	0.35	0.34	0.35	$1.6 \cdot 10^{-3}$
BCY with MS BZY (600 °C)	0.25	0.39	0.35	$1.7 \cdot 10^{-3}$
BCY with SP BZY (1150 °C)	0.33	0.59	0.35	$1.4 \cdot 10^{-3}$
BCY with MS BZY (1350 °C)	0.36	0.33	0.36	$1.7 \cdot 10^{-3}$
BCY with SP BZY (1350 °C)	0.39	0.26	0.36	$1.1 \cdot 10^{-3}$

The protective properties of BZY layer were achieved by applying optimal heat treatment regime which is not accompanied by phase mixing. Although the higher heat treatment temperatures resulted in the grain growth with reduced activation for grain boundary process, the formation of new phase probably increased the activation energy for bulk process. Higher activation energy values obtained for the SP BZY can be ascribed to its lower density. It can be concluded that the protective BZY layers deposited using the SP and MS methods had only a minor influence on the total conductivity of BCY|BZY bilayer membrane, if the particular BCY membranes are used [30].

7. SUMMARY

Ultrasonic spray pyrolysis method was successfully used for deposition of up to 1.1 μm thick oxide-ion and proton conducting electrolyte layers with different protective functions for IT-SOFC application. Although the method is attractive for its low cost and simplicity of experimental set-up, the deposition process of the specific layer must be thoroughly optimized prior to application. As the layer formation is based on thermal decomposition of the precursor salts, the most important parameter for the spray pyrolysis process is the surface temperature of the substrate. For the deposition of homogenous ceramic layers, which was one of the aims of this work, the complete thermal decomposition of precursor material was required in order to ensure high density of the layer. Relatively moderate heat treatment temperatures were required to achieve the high density of layers, which might be a positive aspect, if an additional high temperature treatment of supportive electrolyte|protective layer system should be avoided in order to avoid interdiffusion of cations.

The microstructure and crystal lattice of layers deposited using ultrasonic spray pyrolysis method was influenced both by the dopant concentration and the thermal treatment regime. Effect of Tb co-dopant on the microstructure of $Ce_{0.9}Sm_{0.1-x}Tb_xO_{2-\delta}$ layer was notable at higher thermal treatment temperatures, where the grain growth was probably limited by the respective changes in crystal lattice influencing mobility of the grain boundary. The XRD data obtained confirmed the effect of Tb co-dopant on the lattice parameter and microstrain of $Ce_{0.9}Sm_{0.1-x}Tb_xO_{2-\delta}$ layer. The heat treatment caused the considerable grain growth and some changes in the crystal structure determining the final microstructure of the layer. The lattice parameter change with the increasing heat treatment temperature, observed for the $Ce_{0.9}Gd_{0.1}O_{2-\delta}$ and $BaZr_{1-x}Y_xO_{3-\delta}$ protective layers, can be ascribed to relaxation of residual stresses or cation interdiffusion between the different phases.

The XRD, TOF-SIMS and SEM data obtained demonstrated the considerable effect of final microstructure of $Ce_{0.9}Gd_{0.1}O_{2-\delta}$ barrier layer on the cation mobility. Due to the large fraction of grain boundaries providing a fast pathway for cation motion, the fine-grained structure (characteristic of the spray-pyrolyzed layer after a moderate heat treatment) facilitated the efficient Sr diffusion from $La_xSr_{1-x}CoO_{3-\delta}$ cathode during the sintering process at temperatures 950 and 1100 °C. The diffusion was more intensive at higher sintering temperatures. Additional high-temperature treatment at 1300 °C accompanied by the grain growth effectively suppressed the Sr mobility in the case of moderate sintering temperature for the cathode. The Ce and Zr interdiffusion caused by the high-temperature treatment was accompanied by the increase of layer thickness and formation of sub-layers in some cases. The mixing of Ce and Zr was also observed between the $BaZr_{0.9}Y_{0.1}O_{3-\delta}$ protective layer and $BaCe_{0.9}Y_{0.1}O_{3-\delta}$ support at higher heat treatment temperatures.

Opposite to the ultrasonic spray pyrolysis method, the deposition of $Ce_{0.9}Gd_{0.1}O_{2-\delta}$ barrier layer using pulsed laser deposition and magnetron sput-

tering methods resulted in homogenous material without the fine grains. The high-temperature treatment was accompanied by the layer densification, reducing its thickness without any significant phase mixing. It can be explained with different layer microstructures formed. The overall effect of high-temperature treatment on the Sr mobility was similar, irrespective of the deposition method used, although some exceptions occurred. The differences in the microstructure, crystal lattice and behaviour of the barrier layers (location and appearance of $SrZrO_3$ phase) demonstrated the significant influence of deposition method on SOFC materials.

The lowest amount (1 mol%) of Tb as a co-dopant turned out to be beneficial for Sm-doped ceria electrolyte applied as a protective layer, lowering its lower bound of electrolytic domain by up to one order of magnitude toward lower oxygen partial pressures. The activation energy for the ionic conductivity component was lowered in that case, while the activation energy for electronic conductivity component was increased. The lowered electrolytic domain boundary characteristics mean lower electronic conductivities at redox conditions occurring in SOFC anode|electrolyte systems and leads to higher power density and total efficiency of the SOFC system.

In general, the results of the electrochemical tests are in a good accordance with the results obtained using XRD, TOF-SIMS and SEM analysis for the $Ce_{0.9}Gd_{0.1}O_{2-\delta}$ chemical barrier layers. The SOFC single cell with the raw $Ce_{0.9}Gd_{0.1}O_{2-\delta}$ barrier layer deposited using the ultrasonic spray pyrolysis method exhibited the lowest power density values probably due to the Sr diffusion. The additional high-temperature treatment at 1300 °C somewhat enhanced its electrochemical properties by reducing the fraction of grain boundaries in the layer.

The performance of $Ce_{0.9}Gd_{0.1}O_{2-\delta}$ barrier layer was influenced also by its thickness. The increase of thickness from 0.7 to 1.4 μm improved significantly the properties of $Ce_{0.9}Gd_{0.1}O_{2-\delta}$ barrier layer. The growth of $SrZrO_3$ crystallites in the $Ce_{0.9}Gd_{0.1}O_{2-\delta}$ barrier layer during the high-temperature treatment is probably less harmful than the accumulation of Sr at/into the $Ce_{1-x}Gd_xO_{2-\delta}|Zr_{1-x}Y_xO_{2-\delta}$ interface, which initiates the formation of relatively dense non-conductive $SrZrO_3$ layer. In order to obtain the best performance of SOFC, application of different deposition methods require specifically optimized thicknesses and specific thermal treatment conditions of the $Ce_{0.9}Gd_{0.1}O_{2-\delta}$ barrier layer. The sintering temperature of cathode containing mobile cations should be also optimized.

The protective properties of $BaZr_{0.9}Y_{0.1}O_{3-\delta}$ layer were achieved by applying the optimal thermal treatment regime which is not yet accompanied by the phase mixing. Activation energy and total conductivity values depended on the deposition method and heat treatment conditions used, i.e. on the structure of $BaZr_{0,9}Y_{0,1}O_{3-\delta}$ layer. Although the higher heat treatment temperatures resulted in the grain growth with the reduced activation energy for the grain boundary process (decreased fraction of resistive intergranular phase), formation of new phase by the interdiffusion of Ce and Zr probably increased the activation

energy for the bulk process and degraded the required CO_2 tolerant chemical properties. Higher activation energy values obtained for the $BaZr_{0.9}Y_{0.1}O_{3-\delta}$ layer deposited using the ultrasonic spray pyrolysis can be ascribed to its lower density. It can be concluded that the protective $BaZr_{0.9}Y_{0.1}O_{3-\delta}$ layers deposited had only a minor influence on the total conductivity of $BaCe_{0.9}Y_{0.1}O_{3-\delta}|BaZr_{0.9}Y_{0.1}O_{3-\delta}$ bilayer membrane, if the particular $BaCe_{0.9}Y_{0.1}O_{3-\delta}$ membranes were used.

8. REFERENCES

[1] N.Q. Minh, T. Takahashi, Science and Technology of Ceramic Fuel Cells, Elsevier, 1995.

[2] K. Kendall, M. Kendall, High-temperature Solid Oxide Fuel Cells for the 21st Century: Fundamentals, Design and Applications, Elsevier, 2015.

[3] O. Yamamoto, Solid oxide fuel cells: fundamental aspects and prospects, Electrochim. Acta 45 (2000) 2423–2435.

[4] N. Christiansen, Future Fuel Cells, in: J.T.S. Irvine, P. Connor (Eds.), Solid Oxide Fuels Cells: Facts and Figures, Springer London, 2013.

[5] N. Mahato, A. Banerjee, A. Gupta, S. Omar, K. Balani, Progress in material selection for solid oxide fuel cell technology: A review, Prog. Mater. Sci. 72 (2015) 141–337.

[6] A.B. Stambouli, E. Traversa, Solid oxide fuel cells (SOFCs): a review of an environmentally clean and efficient source of energy, Renew. Sustain. Energy Rev. 6 (2002) 433–455.

[7] K. Huang, J.B. Goodenough, Solid Oxide Fuel Cell Technology: Principles, Performance and Operations, Elsevier, 2009.

[8] J. Yan, Handbook of Clean Energy Systems, 6 Volume Set, John Wiley & Sons, 2015.

[9] G. Kaur, Solid Oxide Fuel Cell Components: Interfacial Compatibility of SOFC Glass Seals, Springer, 2016.

[10] S.C. Singhal, Solid oxide fuel cells for power generation, WIREs Energy Environ. 3 (2014) 179–194.

[11] J.T.S. Irvine, P. Connor, Alternative Materials for SOFCs, Opportunities and Limitations, in: J.T.S. Irvine, P. Connor (Eds.), Solid Oxide Fuels Cells: Facts and Figures, Springer London, 2013.

[12] J. Fergus, R. Hui, X. Li, D.P. Wilkinson, J. Zhang, Solid Oxide Fuel Cells: Materials Properties and Performance, CRC Press, 2009.

[13] J. Schoonman, I. Riess, Oxygen Ion and Mixed Conductors and Their Technological Applications, Springer Science & Business Media, 2000.

[14] P. Holtappels, U. Vogt, T. Graule, Ceramic Materials for Advanced Solid Oxide Fuel Cells, Adv. Eng. Mater. 7 (2005) 292–302.

[15] D.J.L. Brett, A. Atkinson, N.P. Brandon, S.J. Skinner, Intermediate temperature solid oxide fuel cells, Chem. Soc. Rev. 37 (2008) 1568.

[16] T. Ishihara, Perovskite Oxide for Solid Oxide Fuel Cells, Springer Science & Business Media, 2009.

[17] A. Tarancón, Strategies for Lowering Solid Oxide Fuel Cells Operating Temperature, Energies 2 (2009) 1130–1150.

[18] B.C.H. Steele, Material science and engineering: The enabling technology for the commercialisation of fuel cell systems, J. Mater. Sci. 36 (2001) 1053–1068.

[19] Z. Gao, L.V. Mogni, E.C. Miller, J.G. Railsback, S.A. Barnett, A perspective on low-temperature solid oxide fuel cells, Energy Environ. Sci. 9 (2016) 1602–1644.

[20] J. Huang, F. Xie, C. Wang, Z. Mao, Development of solid oxide fuel cell materials for intermediate-to-low temperature operation, Int. J. Hydrogen Energy 37 (2012) 877–883.

[21] J.W. Fergus, Electrolytes for solid oxide fuel cells, J. Power Sources 162 (2006) 30–40.

[22] J.A. Kilner, M. Burriel, Materials for Intermediate-Temperature Solid-Oxide Fuel Cells, Annu. Rev. Mater. Res. 44 (2014) 365–393.
[23] Y. Zhao, C. Xia, L. Jia, Z. Wang, H. Li, J. Yu, Y. Li, Recent progress on solid oxide fuel cell: Lowering temperature and utilizing non-hydrogen fuels, Int. J. Hydrogen Energy 38 (2013).
[24] F. Han, R. Mücke, T. Van Gestel, A. Leonide, N.H. Menzler, H.P. Buchkremer, D. Stöver, Novel high-performance solid oxide fuel cells with bulk ionic conductance dominated thin-film electrolytes, J. Power Sources 218 (2012) 157–162.
[25] Z. Lu, J. Hardy, J. Templeton, J. Stevenson, D. Fisher, N. Wu, A. Ignatiev, Performance of anode-supported solid oxide fuel cell with thin bi-layer electrolyte by pulsed laser deposition, J. Power Sources 210 (2012) 292–296.
[26] N. Jordan, W. Assenmacher, S. Uhlenbruck, V.A.C. Haanappel, H.P. Buchkremer, D. Stöver, W. Mader, $Ce_{0.8}Gd_{0.2}O_{2-\delta}$ protecting layers manufactured by physical vapor deposition for IT-SOFC, Solid State Ion. 179 (2008) 919–923.
[27] J. Will, Fabrication of thin electrolytes for second-generation solid oxide fuel cells, Solid State Ion. 131 (2000) 79–96.
[28] D. Beckel, A. Bieberle-Hütter, A. Harvey, A. Infortuna, U.P. Muecke, M. Prestat, J.L.M. Rupp, L.J. Gauckler, Thin films for micro solid oxide fuel cells, J. Power Sources 173 (2007) 325–345.
[29] N.H. Menzler, F. Han, T. van Gestel, W. Schafbauer, F. Schulze-Küppers, S. Baumann, S. Uhlenbruck, W.A. Meulenberg, L. Blum, H.P. Buchkremer, Application of Thin-Film Manufacturing Technologies to Solid Oxide Fuel Cells and Gas Separation Membranes, Int. J. Appl. Ceram. Tec. 10 (2013) 421–427.
[30] M. Maide, O. Korjus, M. Vestli, T. Romann, J. Aruväli, K. Kirsimäe, G. Nurk, Comparative Study of $BaY_{0.1}Zr_{0.9}O_{3-\delta}$ Protective Layers Deposited to $BaY_{0.1}Ce_{0.9}O_{3-\delta}$ Membrane Using Ultrasonic Spray Pyrolysis and Magnetron Sputtering Methods, J. Electrochem. Soc. 163 (2016) F443−F447 (licensed under CC BY-NC-ND).
[31] G. Nurk, M. Vestli, P. Moller, R. Jaaniso, M. Kodu, H. Mandar, T. Romann, R. Kanarbik, E. Lust, Mobility of Sr in Gadolinia Doped Ceria Barrier Layers Prepared Using Spray Pyrolysis, Pulsed Laser Deposition and Magnetron Sputtering Methods, J. Electrochem. Soc. 163 (2016) F88–F96 (licensed under CC BY-NC-ND).
[32] M. Vestli, E. Lust, G. Nurk, Characterization of Terbium and Samarium Co-Doped Ceria Films Prepared Using Ultrasonic Spray Pyrolysis, J. Electrochem. Soc. 162 (2015) F812–F820.
[33] V. Kharton, F. Marques, A. Atkinson, Transport properties of solid oxide electrolyte ceramics: a brief review, Solid State Ion. 174 (2004) 135–149.
[34] M. Biswas, K.C. Sadanala, Electrolyte Materials for Solid Oxide Fuel Cell, J. Powder Metall. Min. 2014 (2014).
[35] M. Ni, The effect of electrolyte type on performance of solid oxide fuel cells running on hydrocarbon fuels, Int. J. Hydrogen Energy 38 (2013) 2846–2858.
[36] N. Sammes, Fuel Cell Technology: Reaching Towards Commercialization, Springer Science & Business Media, 2006.
[37] N. Bonanos, Perovskite solid electrolytes: Structure, transport properties and fuel cell applications, Solid State Ion. 79 (1995) 161–170.

[38] E.C.C. de Souza, R. Muccillo, Properties and applications of perovskite proton conductors, Mater. Res. 13 (2010) 385–394.
[39] B.C.H. Steele, A. Heinzel, Materials for fuel-cell technologies, Nature 414 (2001) 345–352.
[40] S.J. Skinner, J.A. Kilner, Oxygen ion conductors, Mater. Today 6 (2003) 30–37.
[41] K. Yamaji, Y. Xiong, H. Kishimoto, T. Horita, M.E. Brito, H. Yokokawa, Electronic Conductivity and Efficiency of SOFC Electrolytes, ECS Trans. 12 (2008) 317–322.
[42] M. Mogensen, Physical, chemical and electrochemical properties of pure and doped ceria, Solid State Ion. 129 (2000) 63–94.
[43] S.R. Bishop, D. Marrocchelli, C. Chatzichristodoulou, N.H. Perry, M.B. Mogensen, H.L. Tuller, E.D. Wachsman, Chemical Expansion: Implications for Electrochemical Energy Storage and Conversion Devices, Annu. Rev. Mater. Res. 44 (2014) 205–239.
[44] M. Gödickemeier, Engineering of Solid Oxide Fuel Cells with Ceria-Based Electrolytes, J. Electrochem. Soc. 145 (1998) 414–421.
[45] B. Steele, Appraisal of $Ce_{1-y}Gd_yO_{2-y/2}$ electrolytes for IT-SOFC operation at 500°C, Solid State Ion. 129 (2000) 95–110.
[46] W. Zając, J. Molenda, Properties of doped ceria solid electrolytes in reducing atmospheres, Solid State Ion. 192 (2011) 163–167.
[47] D. Maricle, T. Swarr, S. Karavolis, Enhanced ceria — a low-temperature SOFC electrolyte, Solid State Ion. 52 (1992) 173–182.
[48] N. Kim, B.-H. Kim, D. Lee, Effect of co-dopant addition on properties of gadolinia-doped ceria electrolyte, J. Power Sources 90 (2000) 139–143.
[49] W. Sun, W. Liu, A novel ceria-based solid oxide fuel cell free from internal short circuit, J. Power Sources 217 (2012) 114–119.
[50] S.-H. Park, Ph.D. Thesis, Seoul National University, 2008.
[51] H.-I. Yoo, S.-H. Park, J. Chun, Suppression of Electronic Conductivity of CeO_2-Based Electrolytes by Electron Traps, J. Electrochem. Soc. 157 (2010) B215.
[52] A. Martínez-Arias, A.B. Hungría, M. Fernández-García, A. Iglesias-Juez, J.C. Conesa, G.C. Mather, G. Munuera, Cerium–terbium mixed oxides as potential materials for anodes in solid oxide fuel cells, J. Power Sources 151 (2005) 43–51.
[53] W. Huang, Hydrothermal synthesis and properties of terbium- or praseodymium-doped $Ce_{1-x}Sm_xO_{2-x/2}$ solid solutions, Solid State Ion. 113–115 (1998) 305–310.
[54] P. Shuk, M. Greenblatt, M. Croft, Hydrothermal Synthesis and Properties of Mixed Conducting $Ce_{1-x}Tb_xO_{2-\delta}$ Solid Solutions, Chem. Mater. 11 (1999) 473–479.
[55] R. Chockalingam, S. Basu, $Tb_xCe_{0.95-X}Gd_{0.05}O_{2-\delta}$ ($0.15 \leq x \leq 0.40$) Cathode Materials Prepared through Solid State Route for Low Temperature SOFC, ECS Trans. 57 (2013) 1811–1820.
[56] X. Zhou, Electrical conductivity and stability of Gd-doped ceria/Y-doped zirconia ceramics and thin films, Solid State Ion. 175 (2004) 19–22.
[57] R. Knibbe, J. Hjelm, M. Menon, N. Pryds, M. Søgaard, H.J. Wang, K. Neufeld, Cathode-Electrolyte Interfaces with CGO Barrier Layers in SOFC: Cathode-Electrolyte Interfaces in IT-SOFCs, J. Am. Ceram. Soc. 93 (2010) 2877–2883.

[58] S. Sønderby, T. Klemensø, B.H. Christensen, K.P. Almtoft, J. Lu, L.P. Nielsen, P. Eklund, Magnetron sputtered gadolinia-doped ceria diffusion barriers for metal-supported solid oxide fuel cells, J. Power Sources 267 (2014) 452–458.
[59] J. Richter, P. Holtappels, T. Graule, T. Nakamura, L.J. Gauckler, Materials design for perovskite SOFC cathodes, Monatshefte Für Chem. – Chem. Mon. 140 (2009) 985–999.
[60] H. Yokokawa, N. Sakai, T. Horita, K. Yamaji, M.E. Brito, H. Kishimoto, Thermodynamic and kinetic considerations on degradations in solid oxide fuel cell cathodes, J. Alloy Compd. 452 (2008) 41–47.
[61] A. Tsoga, A. Gupta, A. Naoumidis, P. Nikolopoulos, Gadolinia-doped ceria and yttria stabilized zirconia interfaces: regarding their application for SOFC technology, Acta Mater. 48 (2000) 4709–4714.
[62] F. Wang, M.E. Brito, K. Yamaji, D.-H. Cho, M. Nishi, H. Kishimoto, T. Horita, H. Yokokawa, Effect of polarization on Sr and Zr diffusion behavior in LSCF/GDC/YSZ system, Solid State Ion. 262 (2014) 454–459.
[63] A. Tsoga, Total electrical conductivity and defect structure of ZrO_2–CeO_2–Y_2O_3–Gd_2O_3 solid solutions, Solid State Ion. 135 (2000) 403–409.
[64] S. Uhlenbruck, T. Moskalewicz, N. Jordan, H.-J. Penkalla, H.P. Buchkremer, Element interdiffusion at electrolyte–cathode interfaces in ceramic high-temperature fuel cells, Solid State Ion. 180 (2009) 418–423.
[65] S. Uhlenbruck, N. Jordan, D. Sebold, H.P. Buchkremer, V.A.C. Haanappel, D. Stöver, Thin film coating technologies of $(Ce,Gd)O_{2-\delta}$ interlayers for application in ceramic high-temperature fuel cells, Thin Solid Films 515 (2007) 4053–4060.
[66] S. Sønderby, P.L. Popa, J. Lu, B.H. Christensen, K.P. Almtoft, L.P. Nielsen, P. Eklund, Strontium Diffusion in Magnetron Sputtered Gadolinia-Doped Ceria Thin Film Barrier Coatings for Solid Oxide Fuel Cells, Adv. Energy Mater. 3 (2013) 923–929.
[67] P. Plonczak, M. Joost, J. Hjelm, M. Søgaard, M. Lundberg, P.V. Hendriksen, A high performance ceria based interdiffusion barrier layer prepared by spin-coating, J. Power Sources 196 (2011) 1156–1162.
[68] T. Klemensø, J. Nielsen, P. Blennow, Å.H. Persson, T. Stegk, B.H. Christensen, S. Sønderby, High performance metal-supported solid oxide fuel cells with Gd-doped ceria barrier layers, J. Power Sources. 196 (2011) 9459–9466.
[69] F.P. Van Berkel, Y. Zhang-Steenwinkel, G. Schoemakers, M. Van Tuel, B.G. Rietveld, Enhanced ASC Performance at 600{degree sign}C by Ceria Barrier Layer Optimisation, ECS Trans. 25 (2009) 2717–2726.
[70] R. Kanarbik, P. Moller, I. Kivi, E. Lust, Application of FIB-TOF-SIMS and FIB-SEM-EDX Methods for the Analysis of Element Mobility in Solid Oxide Fuel Cells, ECS Trans. 57 (2013) 581–587.
[71] B.S. M., J. Roy, The effect of strontium doping on densification and electrical properties of $Ce_{0.8}Gd_{0.2}O_{2-\delta}$ electrolyte for IT-SOFC application, Ionics 18 (2012) 291–297.
[72] T. Schober, Applications of oxidic high-temperature proton conductors, Solid State Ion. 162–163 (2003) 277–281.
[73] N. Bonanos, Oxide-based protonic conductors: point defects and transport properties, Solid State Ion. 145 (2001) 265–274.
[74] K.D. Kreuer, Proton-Conducting Oxides, Annu. Rev. Mater. Res. 33 (2003) 333–359.

[75] R. O'Hayre, S.-W. Cha, W. Colella, F.B. Prinz, Fuel Cell Fundamentals, John Wiley & Sons, 2016.
[76] D. Medvedev, A. Murashkina, E. Pikalova, A. Demin, A. Podias, P. Tsiakaras, $BaCeO_3$: Materials development, properties and application, Prog. Mater. Sci. 60 (2014) 72–129.
[77] Z. Tao, Z. Zhu, H. Wang, W. Liu, A stable $BaCeO_3$-based proton conductor for intermediate-temperature solid oxide fuel cells, J. Power Sources 195 (2010) 3481–3484.
[78] K.H. Ryu, S.M. Haile, Chemical stability and proton conductivity of doped $BaCeO_3$–$BaZrO_3$ solid solutions, Solid State Ion. 125 (1999) 355–367.
[79] E. Fabbri, A. Depifanio, E. Dibartolomeo, S. Licoccia, E. Traversa, Tailoring the chemical stability of $Ba(Ce_{0.8-x}Zr_x)Y_{0.2}O_{3-\delta}$ protonic conductors for Intermediate Temperature Solid Oxide Fuel Cells (IT-SOFCs), Solid State Ion. 179 (2008) 558–564.
[80] J. Qian, W. Sun, Q. Zhang, G. Jiang, W. Liu, Fabrication and performance of $BaCe_{0.8}Y_{0.2}O_{3-\delta}$–$BaZr_{0.8}Y_{0.2}O_{3-\delta}$ bilayer electrolyte for anode-supported solid oxide fuel cells, J. Power Sources 249 (2014) 131–136.
[81] E. Fabbri, D. Pergolesi, A. D'Epifanio, E. Di Bartolomeo, G. Balestrino, S. Licoccia, E. Traversa, Design and fabrication of a chemically-stable proton conductor bilayer electrolyte for intermediate temperature solid oxide fuel cells (IT-SOFCs), Energy Environ. Sci. 1 (2008) 355–359.
[82] L. Bi, E. Traversa, A Tri-Layer Proton-Conducting Electrolyte for Chemically Stable Operation in Solid Oxide Fuel Cells, ECS Trans. 57 (2013) 1037–1044.
[83] M.N. Rahaman, Sintering of Ceramics, CRC Press, 2007.
[84] M. Martin, Oxygen and cation diffusion processes in oxygen ion conductors, Diffus. Fundam. 6 (2007) 1–16.
[85] R. Riedel, I.-W. Chen, Ceramics Science and Technology, Structures, John Wiley & Sons, 2015.
[86] M. Izuki, M.E. Brito, K. Yamaji, H. Kishimoto, D.-H. Cho, T. Shimonosono, T. Horita, H. Yokokawa, Interfacial stability and cation diffusion across the LSCF/GDC interface, J. Power Sources 196 (2011) 7232–7236.
[87] P.-L. Chen, I.-W. Chen, Role of Defect Interaction in Boundary Mobility and Cation Diffusivity of CeO2, J. Am. Ceram. Soc. 77 (1994) 2289–2297.
[88] V. Esposito, D.W. Ni, Z. He, W. Zhang, A.S. Prasad, J.A. Glasscock, C. Chatzichristodoulou, S. Ramousse, A. Kaiser, Enhanced mass diffusion phenomena in highly defective doped ceria, Acta Mater. 61 (2013) 6290–6300.
[89] C.L. Perkins, M.A. Henderson, C.H.F. Peden, G.S. Herman, Self-diffusion in ceria, J. Vac. Sci. Technol. A 19 (2001) 1942–1946.
[90] F. Wang, M. Nishi, M.E. Brito, H. Kishimoto, K. Yamaji, H. Yokokawa, T. Horita, Sr and Zr diffusion in LSCF/10GDC/8YSZ triplets for solid oxide fuel cells (SOFCs), J. Power Sources 258 (2014) 281–289.
[91] S.J. Litzelman, R.A. De Souza, B. Butz, H.L. Tuller, M. Martin, D. Gerthsen, Heterogeneously doped nanocrystalline ceria films by grain boundary diffusion: Impact on transport properties, J. Electroceram. 22 (2009) 405–415.
[92] Z. Shao, W. Zhou, Z. Zhu, Advanced synthesis of materials for intermediate-temperature solid oxide fuel cells, Prog. Mater. Sci. 57 (2012) 804–874.
[93] D. Perednis, L.J. Gauckler, Thin Film Deposition Using Spray Pyrolysis, J. Electroceram. 14 (2005) 103–111.

[94] U.P. Muecke, G.L. Messing, L.J. Gauckler, The Leidenfrost effect during spray pyrolysis of nickel oxide-gadolinia doped ceria composite thin films, Thin Solid Films 517 (2009) 1515–1521.
[95] D. Perednis, O. Wilhelm, S.E. Pratsinis, L.J. Gauckler, Morphology and deposition of thin yttria-stabilized zirconia films using spray pyrolysis, Thin Solid Films 474 (2005) 84–95.
[96] J. Rupp, L. Gauckler, Microstructures and electrical conductivity of nanocrystalline ceria-based thin films, Solid State Ion. 177 (2006) 2513–2518.
[97] A. Stoermer, J. Rupp, L. Gauckler, Spray pyrolysis of electrolyte interlayers for vacuum plasma-sprayed SOFC, Solid State Ion. 177 (2006) 2075–2079.
[98] U.P. Muecke, N. Luechinger, L. Schlagenhauf, L.J. Gauckler, Initial stages of deposition and film formation during spray pyrolysis — Nickel oxide, cerium gadolinium oxide and mixtures thereof, Thin Solid Films 517 (2009) 1522–1529.
[99] J.L.M. Rupp, A. Infortuna, L.J. Gauckler, Thermodynamic Stability of Gadolinia-Doped Ceria Thin Film Electrolytes for Micro-Solid Oxide Fuel Cells, J. Am. Ceram. Soc. 90 (2007) 1792–1797.
[100] K. Somroop, R. Pornprasertsuk, S. Jinawath, Fabrication of Y_2O_3-doped $BaZrO_3$ thin films by electrostatic spray deposition, Thin Solid Films 519 (2011) 6408–6412.
[101] R. Eason, Pulsed laser deposition of thin films: applications-led growth of functional materials, Wiley-Interscience, 2007.
[102] L.R. Pederson, P. Singh, X.-D. Zhou, Application of vacuum deposition methods to solid oxide fuel cells, Vacuum 80 (2006) 1066–1083.
[103] M. Suzuki, Oxide ionic conductivity of doped lanthanum chromite thin film interconnectors, Solid State Ion. 96 (1997) 83–88.
[104] H.-S. Noh, K.J. Yoon, B.-K. Kim, H.-J. Je, H.-W. Lee, J.-H. Lee, J.-W. Son, The potential and challenges of thin-film electrolyte and nanostructured electrode for yttria-stabilized zirconia-base anode-supported solid oxide fuel cells, J. Power Sources 247 (2014) 105–111.
[105] H.-S. Noh, K.J. Yoon, B.-K. Kim, H.-J. Je, H.-W. Lee, J.-H. Lee, J.-W. Son, Thermo-mechanical stability of multi-scale-architectured thin-film-based solid oxide fuel cells assessed by thermal cycling tests, J. Power Sources 249 (2014) 125–130.
[106] L.G. Coccia, G.C. Tyrrell, J.A. Kilner, D. Waller, R.J. Chater, I.W. Boyd, Pulsed laser deposition of novel materials for thin film solid oxide fuel cell applications: $Ce_{0.9}Gd_{0.1}O_{1.95}$, $La_{0.7}Sr_{0.3}CoO_y$ and $La_{0.7}Sr_{0.3}Co_{0.2}Fe_{0.8}O_y$, Appl. Surf. Sci. 96–8 (1996) 795–801.
[107] D.M. Mattox, Handbook of Physical Vapor Deposition (PVD) Processing, William Andrew, 2010.
[108] H.S. Nalwa, Deposition and Processing, Academic Press, 2001.
[109] S. Ji, Y.H. Lee, T. Park, G.Y. Cho, S. Noh, Y. Lee, M. Kim, S. Ha, J. An, S.W. Cha, Doped ceria anode interlayer for low-temperature solid oxide fuel cells with nanothin electrolyte, Thin Solid Films 591 (2015) 250–254.
[110] T. Park, Y.H. Lee, G.Y. Cho, S. Ji, J. Park, I. Chang, S.W. Cha, Effect of the thickness of sputtered gadolinia-doped ceria as a cathodic interlayer in solid oxide fuel cells, Thin Solid Films 584 (2015) 120–124.

[111] J. Park, I. Chang, J.Y. Paek, S. Ji, W. Lee, S.W. Cha, J.-M. Lee, Fabrication of the large area thin-film solid oxide fuel cells, CIRP Ann. – Manuf. Techn. 63 (2014) 513–516.
[112] S.-E. Lin, Y.-L. Kuo, C.-H. Chou, W.-C.J. Wei, Characterization of electrolyte films deposited by using RF magnetron sputtering a 20 mol% gadolinia-doped ceria target, Thin Solid Films 518 (2010) 7229–7232.
[113] E. Gourba, P. Briois, A. Ringuedé, M. Cassir, A. Billard, Electrical properties of gadolinia-doped ceria thin films deposited by sputtering in view of SOFC application, J. Solid State Electrochem. 8 (2004) 633–637.
[114] Y.-L. Kuo, C. Lee, Y.-S. Chen, H. Liang, Gadolinia-doped ceria films deposited by RF reactive magnetron sputtering, Solid State Ion. 180 (2009) 1421–1428.
[115] R. Pornprasertsuk, O. Kosasang, K. Somroop, M. Horprathum, P. Limnonthakul, P. Chindaudom, S. Jinawath, Proton conductivity of Y-doped $BaZrO_3$: Pellets and thin films, Solid State Sci. 13 (2011) 1429–1437.
[116] X. Chen, L. Rieth, M.S. Miller, F. Solzbacher, Comparison of Y-doped $Bazro_3$ thin films for high temperature humidity sensors by RF sputtering and pulsed laser deposition, Sensor Actuat. B Chem. 148 (2010) 173–180.
[117] X. Chen, L. Rieth, M.S. Miller, F. Solzbacher, High temperature humidity sensors based on sputtered Y-doped $BaZrO_3$ thin films, Sensor Actuat. B Chem. 137 (2009) 578–585.
[118] I. Kivi, E. Anderson, P. Moller, G. Nurk, E. Lust, Influence of Microstructural Parameters of LSC Cathodes on the Oxygen Reduction Reaction Parameters, J. Electrochem. Soc. 159 (2012) F743–F750.
[119] J.L.M. Rupp, A. Infortuna, L.J. Gauckler, Microstrain and self-limited grain growth in nanocrystalline ceria ceramics, Acta Mater. 54 (2006) 1721–1730.
[120] A. Burgermeister, A. Benisek, W. Sitte, Electrochemical device for the precise adjustment of oxygen partial pressures in a gas stream, Solid State Ion. 170 (2004) 99–104.
[121] L. Bi, E. Traversa, Synthesis strategies for improving the performance of doped-$BaZrO_3$ materials in solid oxide fuel cell applications, J. Mater. Res. 29 (2014) 1–15.
[122] D. Pergolesi, E. Fabbri, A. D'Epifanio, E. Di Bartolomeo, A. Tebano, S. Sanna, S. Licoccia, G. Balestrino, E. Traversa, High proton conduction in grain-boundary-free yttrium-doped barium zirconate films grown by pulsed laser deposition, Nat. Mater. 9 (2010) 846–852.
[123] J.A. Rodriguez, X. Wang, J.C. Hanson, G. Liu, A. Iglesias-Juez, M. Fernández-García, The behavior of mixed-metal oxides: Structural and electronic properties of $Ce_{1-x}Ca_xO_2$ and $Ce_{1-x}Ca_xO_{2-x}$, J. Chem. Phys. 119 (2003) 5659.
[124] P.-L. Chen, I.-W. Chen, Grain Growth in CeO_2: Dopant Effects, Defect Mechanism, and Solute Drag, J. Am. Ceram. Soc. 79 (1996) 1793–1800.
[125] Y. Kuru, S.R. Bishop, J.J. Kim, B. Yildiz, H.L. Tuller, Chemomechanical properties and microstructural stability of nanocrystalline Pr-doped ceria: An in situ X-ray diffraction investigation, Solid State Ion. 193 (2011) 1–4.
[126] M. Balaguer, C. Solís, J.M. Serra, Study of the Transport Properties of the Mixed Ionic Electronic Conductor $Ce_{1-x}Tb_xO_{2-\delta}$ + Co (x = 0.1, 0.2) and Evaluation As Oxygen-Transport Membrane, Chem. Mater. 23 (2011) 2333–2343.
[127] R. Hui, J. Roller, X. Zhang, C. Decès-Petit, Y. Xie, R. Maric, D. Ghosh, Various Approaches To Enhance The Ionic Conductivity For Selected Oxide Electrolytes, in: S. C. Singhal and J. Mizusaki (Eds.), Solid oxide fuel cells IX

(SOFC-IX): proceedings of the international symposium, The Electrochemical Society, New Jersey, 2005.
[128] J.L.M. Rupp, E. Fabbri, D. Marrocchelli, J.-W. Han, D. Chen, E. Traversa, H.L. Tuller, B. Yildiz, Scalable Oxygen-Ion Transport Kinetics in Metal-Oxide Films: Impact of Thermally Induced Lattice Compaction in Acceptor Doped Ceria Films, Adv. Funct. Mater. 24 (2014) 1562–1574.
[129] X. Wang, J.C. Hanson, G. Liu, J.A. Rodriguez, A. Iglesias-Juez, M. Fernández-García, The behavior of mixed-metal oxides: physical and chemical properties of bulk $Ce_{1-x}Tb_xO_2$ and nanoparticles of $Ce_{1-x}Tb_xO_y$, J. Chem. Phys. 121 (2004) 5434–5444.
[130] H. Yamamura, E. Katoh, M. Ichikawa, K. Kakinuma, T. Mori, H. Haneda, Multiple doping effect on the electrical conductivity in the $(Ce_{(1-x-y)}La_{(x)}M_{y})O_{2-delta}$ (M = Ca, Sr) system, Electrochemistry 68 (2000) 455–459.
[131] D. Yan, X. Liu, D. Xu, C. Zhu, W. Ma, J. Niu, Y. Liu, W. Su, Effect of Tb co-dopant on the electrical conductivity of Sm-doped ceria electrolyte, Solid State Ion. 179 (2008) 995–999.
[132] D. Pérez-Coll, P. Núñez, J.R. Frade, Effect of samarium content on onset of minor p-type conductivity in ceria-based electrolytes, J. Power Sources 227 (2013) 145–152.
[133] Q. Chen, A. Braun, S. Yoon, N. Bagdassarov, T. Graule, Effect of lattice volume and compressive strain on the conductivity of BaCeY-oxide ceramic proton conductors, J. Eur. Ceram. Soc. 31 (2011) 2657–2661.
[134] A. Grimaud, J.M. Bassat, F. Mauvy, P. Simon, A. Canizares, B. Rousseau, M. Marrony, J.C. Grenier, Transport properties and in-situ Raman spectroscopy study of $BaCe_{0.9}Y_{0.1}O_{3-\delta}$ as a function of water partial pressures, Solid State Ion. 191 (2011) 24–31.
[135] K. Katahira, Y. Kohchi, T. Shimura, H. Iwahara, Protonic conduction in Zr-substituted $BaCeO_3$, Solid State Ion. 138 (2000) 91–98.
[136] S.B.C. Duval, P. Holtappels, U.F. Vogt, U. Stimming, T. Graule, Characterisation of $BaZr_{0.9}Y_{0.1}O_{3-\delta}$ Prepared by Three Different Synthesis Methods: Study of the Sinterability and the Conductivity, Fuel Cells 9 (2009) 613–621.
[137] P. Babilo, T. Uda, S.M. Haile, Processing of yttrium-doped barium zirconate for high proton conductivity, J. Mater. Res. 22 (2007) 1322–1330.

9. SUMMARY IN ESTONIAN

Ultraheli-pihustuspürolüüsi meetodiga sadestatud elektrolüüdikihid kesktemperatuursele tahkeoksiidsele kütuseelemendile

Käesolevas doktoritöös rakendati ultraheli-pihustuspürolüüsi meetodit erinevate kesktemperatuurses tahkeoksiidses kütuseelemendis kasutust leidvate kaitsvate homogeensete kihtide sadestamiseks ning uuriti sünteesimeetodiga kaasnevaid piiranguid. Hinnati valmistatud $Ce_{0.9}Sm_{0.1-x}Tb_xO_{2-\delta}$, $Ce_{0.9}Gd_{0.1}O_{2-\delta}$ ja $BaZr_{0.9}Y_{0.1}O_{3-\delta}$ elektrolüüdikihtide kaitsvaid omadusi, mis toimivad vastavalt elektronjuhtivuse, Sr difusiooni ja CO_2 kahjuliku toime vastu. Ultraheli-pihustuspürolüüsi meetodit kasutati kuni 1.1 µm paksusega kihtide sadestamiseks. Kuigi antud meetod on atraktiivne oma odavuse ja lihtsuse tõttu, on soovitud omadustega kihi saamiseks vajalik eelnev sadestamisprotsessi optimeerimine. Kuna antud meetodi puhul põhineb kihi moodustumine lähteainete termilisel lagunemisel kuumutatud substraadil, on kõige olulisem kontrollitav parameeter substraadi pinnatemperatuur. Ühtlaste tihedate keraamiliste kihtide sadestamiseks tuleb saavutada lähteainete täielik lagunemine. Antud meetodi puhul on positiivne, et tiheda kihi saamiseks on vajalik töötlustemperatuur küllaltki mõõdukas, mis aitab vältida soovimatut katioonide difusiooni kandva elektrolüüdi ja kaitsva elektrolüüdikihi vahel.

Ultraheli-pihustuspürolüüsi meetodiga sadestatud kihtide mikro- ja kristallstruktuur sõltus nii dopandi kontsentratsioonist kui ka termilise töötluse parameetritest. Kaasdopandi Tb mõju $Ce_{0.9}Sm_{0.1-x}Tb_xO_{2-\delta}$ kihi mikrostruktuurile tuli välja kõrgematel töötlustemperatuuridel, kus sadestise tera kasv oli nähtavasti takistatud vastavatest muutustest materjali kristallstruktuuris, mis omakorda mõjutasid terade vahelise piirpinna omadusi, kaasa arvatud ioonide liikuvust. Röntgenstruktuuranalüüs kinnitas kaasdopandi Tb mõju $Ce_{0.9}Sm_{0.1-x}Tb_xO_{2-\delta}$ kihi kristallstruktuurile. Termiline töötlus määras kihi lõpliku mikrostruktuuri läbi tera kasvu ja muutunud kristallstruktuuri. $Ce_{0.9}Gd_{0.1}O_{2-\delta}$ ja $BaZr_{1-x}Y_xO_{3-\delta}$ kihtide puhul termilise töötluse käigus toimunud võreparameetrite muutused saab omistada kihi moodustumisel materjali sisse jäänud pingete relakseerumisele või katioonide difusioonile erinevate faaside vahel.

Röntgenstruktuuranalüüs, lennuaja sekundaarioonide massi-spektromeetria ja elektronmikroskoopia näitasid mikrostruktuuri märkimisväärset mõju katioonide liikuvusele $Ce_{0.9}Gd_{0.1}O_{2-\delta}$ barjäärkihis. Suur terade vahelise piirpinna osakaal mikrostruktuuris hõlbustas katioonide difusiooni. Seetõttu toimus peeneteralise mikrostruktuuri (iseloomulik omadus pihustuspürolüüsi meetodiga sadestatud kihtide puhul, mida on töödeldud mõõdukatel temperatuuridel) korral intensiivne Sr difusioon $La_xSr_{1-x}CoO_{3-\delta}$ katoodi termilisel töötlemisel. Katoodi töötlustemperatuuri tõstmine 950 °C-lt 1100 °C-le tõstis Sr difusiooni intensiivsust veelgi. Täiendava kõrgtemperatuurse töötlemisega temperatuuril

1300 °C kaasnenud tera kasv $Ce_{0.9}Gd_{0.1}O_{2-\delta}$ barjäärkihis vähendas märkimisväärselt Sr difusiooni juhul, kui katood oli töödeldud mõõdukal temperatuuril. Mõningatel juhtudel põhjustas kõrgtemperatuurse töötlemisega kaasnenud Ce and Zr omavaheline segunemine $Ce_{0.9}Gd_{0.1}O_{2-\delta}$ barjäärkihi paksuse kasvamist ja erinevate koostiste ning struktuuridega alamkihtide moodustumist selle sees. Ce ja Zr omavaheline segunemine oli samuti märgatav kõrgematel töötlemistemperatuuridel $BaZr_{0.9}Y_{0.1}O_{3-\delta}$ kaitsekihi ja $BaCe_{0.9}Y_{0.1}O_{3-\delta}$ membraani vahel.

Erinevalt ultraheli-pihustuspürolüüsi meetodist moodustus impulss-laser- ja magnetronsadestamise meetodite puhul $Ce_{0.9}Gd_{0.1}O_{2-\delta}$ barjäärkiht, millel oli mitteteraline homogeenne mikrostruktuur. Kõrgtemperatuurse töötlusega kaasnes materjali tihenemine, mis viis kihi paksuse vähenemiseni. Märkimisväärset Ce and Zr omavahelist segunemist ei esinenud impulss-laser- ja magnetronsadestamise meetodite puhul, mis on seletatav sadestatud $Ce_{0.9}Gd_{0.1}O_{2-\delta}$ barjäärkihtide erineva mikrostruktuuriga. Täiendava kõrgtemperatuurse töötluse mõju Sr difusioonile $Ce_{0.9}Gd_{0.1}O_{2-\delta}$ barjäärkihis oli koos mõningate eranditega üldiselt sama, sõltumata kasutatud sadestusmeetodist. $Ce_{0.9}Gd_{0.1}O_{2-\delta}$ barjäärkihtide varieeruv mikrostruktuur, kristallstruktuur ja käitumine barjäärkihina (Sr and Zr omavahelise segunemise käigus moodustunud $SrZrO_3$ faasi jaotus $Ce_{0.9}Gd_{0.1}O_{2-\delta}$ faasis) erinevate sadestusmeetodite korral toovad välja sadestusmeetodi valiku mõju tahkeoksiidse kütuseelemendi komponendi omadustele.

Madalaim (1 mool%) kaasdopandi Tb kontsentratsioon parandas Sm-dopeeritud tseeriumoksiidse elektrolüüdi omadusi, laiendades selle tööpiirkonda kuni ühe suurusjärgu võrra madalamatele hapniku osarõhkudele. Ioonjuhtivuse aktivatsioonienergia antud juhul alanes, kuid samas elektronjuhtivuse aktivatsioonienergia kasvas. Elektrolüüdi tööpiirkond madalamatel hapniku osarõhkudel tähendab väiksemat elektronjuhtivust anood|elektrolüüt sektsioonis valitsevates redokstingimustes ning tahkeoksiidse kütuseelemendi suuremat võimustihedust ja efektiivsust.

Üldiselt on $Ce_{0.9}Gd_{0.1}O_{2-\delta}$ barjäärkihtide kohta elektrokeemilise analüüsiga saadud andmed kooskõlas vastavate röntgenstruktuur-analüüsi, lennuaja sekundaarioonide massi-spektromeetria ja elektronmikroskoopia tulemustega. Tahkeoksiidse kütuseelemendi ühikrakk, kus kasutati ultraheli-pihustuspürolüüsi meetodiga sadestatud $Ce_{0.9}Gd_{0.1}O_{2-\delta}$ barjäärkihti ilma täiendava kõrgtemperatuurse töötluseta, näitas kõige madalamaid võimsustihedusi. Termiline töötlus temperatuuril 1300 °C vähendas terade vahelise piirpinna osakaalu $Ce_{0.9}Gd_{0.1}O_{2-\delta}$ barjäärkihis ja parendas sel viisil selle elektrokeemilisi omadusi.

$Ce_{0.9}Gd_{0.1}O_{2-\delta}$ barjäärkihi toimimine sõltus ka selle paksusest. Paksuse kasv 0.7 µm-lt 1.4 µm-le parendas märkimisväärselt $Ce_{0.9}Gd_{0.1}O_{2-\delta}$ barjäärkihi omadusi. Nähtavasti on kõrgtemperatuursel töötlusel aset leidev $SrZrO_3$ kristalliitide teke $Ce_{0.9}Gd_{0.1}O_{2-\delta}$ barjäärkihis vähem kahjulik kui Sr akumuleerumisel $Ce_{1-x}Gd_xO_{2-\delta}|Zr_{1-x}Y_xO_{2-\delta}$ piirpinnale tekkiv tihe mittejuhtiv $SrZrO_3$ vahekiht. Parimate võimsuskarakteristikutega tahkeoksiidse kütuseelemendi jaoks on vajalik erinevate meetodite rakendamisel $Ce_{0.9}Gd_{0.1}O_{2-\delta}$ barjäärkihtide sadestamiseks läbi viia optimeerimisprotsess nii kihi paksuse kui ka termilise töötluse jaoks.

Kergelt difundeeruvaid katioone sisaldava katoodi termilise töötluse temperatuur peab olema samuti optimeeritud.

$BaZr_{0.9}Y_{0.1}O_{3-\delta}$ kihi kaitsvad omadused saavutati rakendades termilist töötlust, millega veel ei kaasnenud faaside segunemist. Aktivatsioonienergiate ja summaarsete juhtivuste väärtused sõltusid nii kasutatud sadestusmeetodist kui ka termilise töötluse tingimustest, mis määrasid ära $BaZr_{0.9}Y_{0.1}O_{3-\delta}$ kihi lõpliku struktuuri. Kõrgemate töötlustemperatuuridega kaasnes tera kasv (viletsate juhtivuslike omadustega terade vahelise piirpinna osakaal mikrostruktuuris vähenes) ja alanenud aktivatsioonienergia terade vahelisel piirpinnal toimuvate protsesside jaoks. Samas Ce ja Zr omavahelise segunemisega kaasnenud uue faasi teke nähtavasti tõstis aktivatsioonienergiat faasisisemuses asetleidvate protsesside jaoks ning viis alla materjali CO_2 taluvuse. Kõrgemad aktivatsioonienergiad saadi $BaZr_{0.9}Y_{0.1}O_{3-\delta}$ kihtide korral, mis olid sadestatud ultraheli-pihustuspürolüüsi meetodiga. See on seletatav nende kihtide madalama tihedusega võrreldes magnetronsadestamise meetodil valmistatud $BaZr_{0.9}Y_{0.1}O_{3-\delta}$ kihtidega. Kokkuvõtvalt saab väita, et antud töös kasutatud $BaCe_{0.9}Y_{0.1}O_{3-\delta}$ membraanide korral oli kaitsvatel $BaZr_{0.9}Y_{0.1}O_{3-\delta}$ kihtidel küllaltki väike mõju $BaCe_{0.9}Y_{0.1}O_{3-\delta}|BaZr_{0.9}Y_{0.1}O_{3-\delta}$ süsteemide summaarsele juhtivusele.

10. ACKNOWLEDGEMENTS

First and foremost, I would like to express my deepest gratitude to my supervisors Prof. Enn Lust and Gunnar Nurk for all their patient guidance, inspiration and encouragement during my electrochemical studies and research work.

I am also very grateful to my colleagues for all the technical support, exciting discussions and helpful comments.

Finally, I would like to thank my family and friends for understanding and unconditional support.

This work has been financially supported by Estonian target research project IUT20–13, by the EU through the European Regional Development Fund (Material Technology Program project No. 3.2.1101.12-0014, Estonian Energy Technology Program project No. 3.2.0501.10-0015**,** the Estonian Centre of Excellence in Science project No. 3.2.0101–0030, "Modernisation of Scientific Equipment" project "Nanomaterials in High-efficiency Energetics" 3.2.0302.10-0169), European Spallation Source Project: Estonian Partition in ESS Instrument design, development and building and application for scientific research (SLOKT12026T), by a scholarship from the World Federation of Scientists and by the graduate school „Functional materials and technologies“, receiving funding from the European Social Fund under project 1.2.0401.09-0079 in Estonia.

CURRICULUM VITAE

Name: Mihkel Vestli
Date of birth: June 4, 1985
Citizenship: Estonian
Contact: Institute of Chemistry, University of Tartu, Ravila 14a, 50411, Tartu, Estonia
E-mail: mihkel.vestli@ut.ee

Education:

2010–…	University of Tartu, Institute of Chemistry, PhD student
2008–2010	University of Tartu – Master's degree in chemistry
2004–2007	Tallinn University of Technology – Bachelor degree in chemical and environment technology

Professional employment:

2010–...	University of Tartu, Institute of Chemistry, chemist

List of publications:

1. E. Lust, I. Kivi, K. Tamm, P. Möller, A. Samussenko, E. Anderson, H. Kurig, M. Vestli, G. Nurk, Optimization of Solid Oxide Fuel Cell Materials Structure and Porosity, Proceedings of 9th European Solid Oxide Fuel Cell Forum: 9th European Solid Oxide Fuel Cell Forum, Lucerne, Switzerland, 29. June – 2. July 2010.
2. E. Lust, I. Kivi, K. Tamm, P. Möller, E. Anderson, R. Kanarbik, H. Kurig, M. Vestli, G. Nurk, Solid Oxide Fuel Cells Based on Supporting Porous Anode, Bi-layered Electrolyte and $Pr_{1-x}Sr_xCoO_{3-\delta}$ Cathodes, 62nd Annual Meeting of the International Society of Electrochemistry, Niigata, Japan, 11.–16. Sept. 2011.
3. E. Lust, I. Kivi, K. Tamm, P. Möller, E. Anderson, R. Kanarbik, H. Kurig, M. Vestli, G. Nurk, $La_{1-x}Sr_xCoO_{3-\delta}$ and $Pr_{1-x}Sr_xCoO_{3-\delta}$ Micro-Meso-Porous Cathodes for Medium-Temperature Solid Oxide Fuel Cells, 220th ECS Meeting, Boston, MA, 9.–14. oct. 2011.
4. M. Vestli, G. Nurk, E. Lust, Electrical Properties of Tb and Sm Co-Doped Ceria Electrolyte at Different Oxygen Partial Pressures, ECS Trans. 35 (2011) 1219–1224.
5. E. Lust, I. Kivi, K. Tamm, P. Möller, E. Anderson, H. Kurig, M. Vestli, G. Nurk, Medium Temperature Solid Oxide Fuel Cells Based on Supporting Porous Anode and Bilayered Electrolyte, ECS Trans. 35 (2011) 333−342.
6. Kivi, I. Drovtar, E. Anderson, J. Aruväli, K. Tamm, G. Nurk, P. Möller, M. Vestli, R. Kanarbik, E. Lust, Influence of Cathode Thickness on the Oxygen Reduction Kinetics at the Intermediate Temperature SOFC Cathodes, ECS Transactions 35 (2011) 2349–2355.

7. H. Kurig, M. Vestli, A. Jänes, E. Lust, Electrical Double Layer Capacitors Based on Two 1-Ethyl-3-Methylimidazolium Ionic Liquids with Different Anions, Electrochemical and Solid-State Letters, 14 (2011) A120–A122.
8. H. Kurig, M. Vestli, K. Tõnurist, A. Jänes, E. Lust, Influence of Room Temperature Ionic Liquid Anion Chemical Composition and Electrical Charge Delocalization on the Supercapacitor Properties, Journal of the Electrochemical Society, 159 (2012) A944–A951.
9. M. Vestli, M. Maide, G. Nurk, E. Lust, Characterization of Doped Ceria Films as SOFC Electrolyte Prepared by Using Ultrasonic Spray Pyrolysis Method, ECS Trans. 57 (2013) 1159–1165.
10. M. Maide, O. Korjus, M. Vestli, E. Lust, G. Nurk, Protective Yttrium Doped Barium Zirconate Layer on Yttrium Doped Barium Cerate Proton Conductive Membrane, ECS Trans. 57 (2013) 1151–1157.
11. M. Maide, O. Korjus, M. Vestli, T. Romann, G. Nurk, Comparative Study of $BaY_{0.1}Ce_{0.9}O_{3-\delta}$ Membrane with $BaY_{0.1}Zr_{0.9}O_{3-\delta}$ Protective Layers Synthesized with Spray Pyrolysis and Magnetron Sputtering Methods, ECS Trans. 68 (2015) 473–480.
12. M. Vestli, G. Nurk, Characterization of Terbium and Samarium Co-Doped Ceria Films as SOFC Electrolyte Prepared by Using Ultrasonic Spray Pyrolysis Method, ECS Trans. 68 (2015) 359–367.
13. M. Vestli, E. Lust, G. Nurk, Characterization of Terbium and Samarium Co-Doped Ceria Films Prepared Using Ultrasonic Spray Pyrolysis, J. Electrochem. Soc. 162 (2015) F812–F820.
14. G. Nurk, P. Möller, M. Vestli, R. Jaaniso, M. Kodu, H. Mändar, R. Kanarbik, E. Lust, Mobilty of Sr in Gadolinia Doped Ceria SOFC Chemical Barrier Layers Prepared Using Spray Pyrolysis, Pulsed Laser Deposition and Magnetron Sputtering Methods, ECS Trans. 68 (2015) 1757–1763.
15. M. Maide, O. Korjus, M. Vestli, T. Romann, J. Aruväli, K. Kirsimäe, G. Nurk, Comparative Study of $BaY_{0.1}Zr_{0.9}O_{3-\delta}$ Protective Layers Deposited to $BaY_{0.1}Ce_{0.9}O_{3-\delta}$ Membrane Using Ultrasonic Spray Pyrolysis and Magnetron Sputtering Methods, J. Electrochem. Soc. 163 (2016) F443−F447.
16. G. Nurk, M. Vestli, P. Möller, R. Jaaniso, M. Kodu, H. Mändar, T. Romann, R. Kanarbik, E. Lust, Mobility of Sr in Gadolinia Doped Ceria Barrier Layers Prepared Using Spray Pyrolysis, Pulsed Laser Deposition and Magnetron Sputtering Methods, J. Electrochem. Soc. 163 (2016) F88–F96.

ELULOOKIRJELDUS

Nimi: Mihkel Vestli
Sünniaeg: 4. juuni 1985
Kodakondsus: Eesti
Kontakt: Keemia Instituut, Tartu Ülikool, Ravila 14a, 50411, Tartu, Eesti
E-post: mihkel.vestli@ut.ee

Haridus:

2010–…	Tartu Ülikool, Keemia Instituut, doktorant
2008–2010	Tartu Ülikool – Magistrikraad keemias
2004–2007	Tallinna Tehnikaülikool – Bakalaureusekraad keemia- ja keskkonnakaitse tehnoloogias

Teenistuskäik:

2010–...	Tartu Ülikool, Keemia Instituut, keemik

Teaduspublikatsioonid:

1. E. Lust, I. Kivi, K. Tamm, P. Möller, A. Samussenko, E. Anderson, H. Kurig, M. Vestli, G. Nurk, Optimization of Solid Oxide Fuel Cell Materials Structure and Porosity, Proceedings of 9th European Solid Oxide Fuel Cell Forum: 9th European Solid Oxide Fuel Cell Forum, Lucerne, Switzerland, 29. June – 2. July 2010.
2. E. Lust, I. Kivi, K. Tamm, P. Möller, E. Anderson, R. Kanarbik, H. Kurig, M. Vestli, G. Nurk, Solid Oxide Fuel Cells Based on Supporting Porous Anode, Bi-layered Electrolyte and $Pr_{1-x}Sr_xCoO_{3-\delta}$ Cathodes, 62nd Annual Meeting of the International Society of Electrochemistry, Niigata, Japan, 11.–16. Sept. 2011.
3. E. Lust, I. Kivi, K. Tamm, P. Möller, E. Anderson, R. Kanarbik, H. Kurig, M. Vestli, G. Nurk, $La_{1-x}Sr_xCoO_{3-\delta}$ and $Pr_{1-x}Sr_xCoO_{3-\delta}$ Micro-Meso-Porous Cathodes for Medium-Temperature Solid Oxide Fuel Cells, 220th ECS Meeting, Boston, MA, 9.–14. oct. 2011.
4. M. Vestli, G. Nurk, E. Lust, Electrical Properties of Tb and Sm Co-Doped Ceria Electrolyte at Different Oxygen Partial Pressures, ECS Trans. 35 (2011) 1219–1224.
5. E. Lust, I. Kivi, K. Tamm, P. Möller, E. Anderson, H. Kurig, M. Vestli, G. Nurk, Medium Temperature Solid Oxide Fuel Cells Based on Supporting Porous Anode and Bilayered Electrolyte, ECS Trans. 35 (2011) 333−342.
6. Kivi, I. Drovtar, E. Anderson, J. Aruväli, K. Tamm, G. Nurk, P. Möller, M. Vestli, R. Kanarbik, E. Lust, Influence of Cathode Thickness on the Oxygen Reduction Kinetics at the Intermediate Temperature SOFC Cathodes, ECS Transactions 35 (2011) 2349–2355.
7. H. Kurig, M. Vestli, A. Jänes, E. Lust, Electrical Double Layer Capacitors Based on Two 1-Ethyl-3-Methylimidazolium Ionic Liquids with Different Anions, Electrochemical and Solid-State Letters, 14 (2011) A120−A122.

8. H. Kurig, M. Vestli, K. Tõnurist, A. Jänes, E. Lust, Influence of Room Temperature Ionic Liquid Anion Chemical Composition and Electrical Charge Delocalization on the Supercapacitor Properties, Journal of the Electrochemical Society, 159 (2012) A944–A951.
9. M. Vestli, M. Maide, G. Nurk, E. Lust, Characterization of Doped Ceria Films as SOFC Electrolyte Prepared by Using Ultrasonic Spray Pyrolysis Method, ECS Trans. 57 (2013) 1159–1165.
10. M. Maide, O. Korjus, M. Vestli, E. Lust, G. Nurk, Protective Yttrium Doped Barium Zirconate Layer on Yttrium Doped Barium Cerate Proton Conductive Membrane, ECS Trans. 57 (2013) 1151–1157.
11. M. Maide, O. Korjus, M. Vestli, T. Romann, G. Nurk, Comparative Study of $BaY_{0.1}Ce_{0.9}O_{3-\delta}$ Membrane with $BaY_{0.1}Zr_{0.9}O_{3-\delta}$ Protective Layers Synthesized with Spray Pyrolysis and Magnetron Sputtering Methods, ECS Trans. 68 (2015) 473–480.
12. M. Vestli, G. Nurk, Characterization of Terbium and Samarium Co-Doped Ceria Films as SOFC Electrolyte Prepared by Using Ultrasonic Spray Pyrolysis Method, ECS Trans. 68 (2015) 359–367.
13. M. Vestli, E. Lust, G. Nurk, Characterization of Terbium and Samarium Co-Doped Ceria Films Prepared Using Ultrasonic Spray Pyrolysis, J. Electrochem. Soc. 162 (2015) F812–F820.
14. G. Nurk, P. Möller, M. Vestli, R. Jaaniso, M. Kodu, H. Mändar, R. Kanarbik, E. Lust, Mobilty of Sr in Gadolinia Doped Ceria SOFC Chemical Barrier Layers Prepared Using Spray Pyrolysis, Pulsed Laser Deposition and Magnetron Sputtering Methods, ECS Trans. 68 (2015) 1757–1763.
15. M. Maide, O. Korjus, M. Vestli, T. Romann, J. Aruväli, K. Kirsimäe, G. Nurk, Comparative Study of $BaY_{0.1}Zr_{0.9}O_{3-\delta}$ Protective Layers Deposited to $BaY_{0.1}Ce_{0.9}O_{3-\delta}$ Membrane Using Ultrasonic Spray Pyrolysis and Magnetron Sputtering Methods, J. Electrochem. Soc. 163 (2016) F443–F447.
16. G. Nurk, M. Vestli, P. Möller, R. Jaaniso, M. Kodu, H. Mändar, T. Romann, R. Kanarbik, E. Lust, Mobility of Sr in Gadolinia Doped Ceria Barrier Layers Prepared Using Spray Pyrolysis, Pulsed Laser Deposition and Magnetron Sputtering Methods, J. Electrochem. Soc. 163 (2016) F88–F96.

DISSERTATIONES CHIMICAE UNIVERSITATIS TARTUENSIS

1. **Toomas Tamm.** Quantum-chemical simulation of solvent effects. Tartu, 1993, 110 p.
2. **Peeter Burk.** Theoretical study of gas-phase acid-base equilibria. Tartu, 1994, 96 p.
3. **Victor Lobanov.** Quantitative structure-property relationships in large descriptor spaces. Tartu, 1995, 135 p.
4. **Vahur Mäemets.** The ^{17}O and ^{1}H nuclear magnetic resonance study of H_2O in individual solvents and its charged clusters in aqueous solutions of electrolytes. Tartu, 1997, 140 p.
5. **Andrus Metsala.** Microcanonical rate constant in nonequilibrium distribution of vibrational energy and in restricted intramolecular vibrational energy redistribution on the basis of slater's theory of unimolecular reactions. Tartu, 1997, 150 p.
6. **Uko Maran.** Quantum-mechanical study of potential energy surfaces in different environments. Tartu, 1997, 137 p.
7. **Alar Jänes.** Adsorption of organic compounds on antimony, bismuth and cadmium electrodes. Tartu, 1998, 219 p.
8. **Kaido Tammeveski.** Oxygen electroreduction on thin platinum films and the electrochemical detection of superoxide anion. Tartu, 1998, 139 p.
9. **Ivo Leito.** Studies of Brønsted acid-base equilibria in water and non-aqueous media. Tartu, 1998, 101 p.
10. **Jaan Leis.** Conformational dynamics and equilibria in amides. Tartu, 1998, 131 p.
11. **Toonika Rinken.** The modelling of amperometric biosensors based on oxidoreductases. Tartu, 2000, 108 p.
12. **Dmitri Panov.** Partially solvated Grignard reagents. Tartu, 2000, 64 p.
13. **Kaja Orupõld.** Treatment and analysis of phenolic wastewater with microorganisms. Tartu, 2000, 123 p.
14. **Jüri Ivask.** Ion Chromatographic determination of major anions and cations in polar ice core. Tartu, 2000, 85 p.
15. **Lauri Vares.** Stereoselective Synthesis of Tetrahydrofuran and Tetrahydropyran Derivatives by Use of Asymmetric Horner-Wadsworth-Emmons and Ring Closure Reactions. Tartu, 2000, 184 p.
16. **Martin Lepiku.** Kinetic aspects of dopamine D_2 receptor interactions with specific ligands. Tartu, 2000, 81 p.
17. **Katrin Sak.** Some aspects of ligand specificity of P2Y receptors. Tartu, 2000, 106 p.
18. **Vello Pällin.** The role of solvation in the formation of iotsitch complexes. Tartu, 2001, 95 p.
19. **Katrin Kollist.** Interactions between polycyclic aromatic compounds and humic substances. Tartu, 2001, 93 p.

20. **Ivar Koppel.** Quantum chemical study of acidity of strong and superstrong Brønsted acids. Tartu, 2001, 104 p.
21. **Viljar Pihl.** The study of the substituent and solvent effects on the acidity of OH and CH acids. Tartu, 2001, 132 p.
22. **Natalia Palm.** Specification of the minimum, sufficient and significant set of descriptors for general description of solvent effects. Tartu, 2001, 134 p.
23. **Sulev Sild.** QSPR/QSAR approaches for complex molecular systems. Tartu, 2001, 134 p.
24. **Ruslan Petrukhin.** Industrial applications of the quantitative structure-property relationships. Tartu, 2001, 162 p.
25. **Boris V. Rogovoy.** Synthesis of (benzotriazolyl)carboximidamides and their application in relations with *N*- and *S*-nucleophyles. Tartu, 2002, 84 p.
26. **Koit Herodes.** Solvent effects on UV-vis absorption spectra of some solvatochromic substances in binary solvent mixtures: the preferential solvation model. Tartu, 2002, 102 p.
27. **Anti Perkson.** Synthesis and characterisation of nanostructured carbon. Tartu, 2002, 152 p.
28. **Ivari Kaljurand.** Self-consistent acidity scales of neutral and cationic Brønsted acids in acetonitrile and tetrahydrofuran. Tartu, 2003, 108 p.
29. **Karmen Lust.** Adsorption of anions on bismuth single crystal electrodes. Tartu, 2003, 128 p.
30. **Mare Piirsalu.** Substituent, temperature and solvent effects on the alkaline hydrolysis of substituted phenyl and alkyl esters of benzoic acid. Tartu, 2003, 156 p.
31. **Meeri Sassian.** Reactions of partially solvated Grignard reagents. Tartu, 2003, 78 p.
32. **Tarmo Tamm.** Quantum chemical modelling of polypyrrole. Tartu, 2003. 100 p.
33. **Erik Teinemaa.** The environmental fate of the particulate matter and organic pollutants from an oil shale power plant. Tartu, 2003. 102 p.
34. **Jaana Tammiku-Taul.** Quantum chemical study of the properties of Grignard reagents. Tartu, 2003. 120 p.
35. **Andre Lomaka.** Biomedical applications of predictive computational chemistry. Tartu, 2003. 132 p.
36. **Kostyantyn Kirichenko.** Benzotriazole – Mediated Carbon–Carbon Bond Formation. Tartu, 2003. 132 p.
37. **Gunnar Nurk.** Adsorption kinetics of some organic compounds on bismuth single crystal electrodes. Tartu, 2003, 170 p.
38. **Mati Arulepp.** Electrochemical characteristics of porous carbon materials and electrical double layer capacitors. Tartu, 2003, 196 p.
39. **Dan Cornel Fara.** QSPR modeling of complexation and distribution of organic compounds. Tartu, 2004, 126 p.
40. **Riina Mahlapuu.** Signalling of galanin and amyloid precursor protein through adenylate cyclase. Tartu, 2004, 124 p.

41. **Mihkel Kerikmäe.** Some luminescent materials for dosimetric applications and physical research. Tartu, 2004, 143 p.
42. **Jaanus Kruusma.** Determination of some important trace metal ions in human blood. Tartu, 2004, 115 p.
43. **Urmas Johanson.** Investigations of the electrochemical properties of polypyrrole modified electrodes. Tartu, 2004, 91 p.
44. **Kaido Sillar.** Computational study of the acid sites in zeolite ZSM-5. Tartu, 2004, 80 p.
45. **Aldo Oras.** Kinetic aspects of dATPαS interaction with $P2Y_1$ receptor. Tartu, 2004, 75 p.
46. **Erik Mölder.** Measurement of the oxygen mass transfer through the air-water interface. Tartu, 2005, 73 p.
47. **Thomas Thomberg.** The kinetics of electroreduction of peroxodisulfate anion on cadmium (0001) single crystal electrode. Tartu, 2005, 95 p.
48. **Olavi Loog.** Aspects of condensations of carbonyl compounds and their imine analogues. Tartu, 2005, 83 p.
49. **Siim Salmar.** Effect of ultrasound on ester hydrolysis in aqueous ethanol. Tartu, 2006, 73 p.
50. **Ain Uustare.** Modulation of signal transduction of heptahelical receptors by other receptors and G proteins. Tartu, 2006, 121 p.
51. **Sergei Yurchenko.** Determination of some carcinogenic contaminants in food. Tartu, 2006, 143 p.
52. **Kaido Tämm.** QSPR modeling of some properties of organic compounds. Tartu, 2006, 67 p.
53. **Olga Tšubrik.** New methods in the synthesis of multisubstituted hydrazines. Tartu. 2006, 183 p.
54. **Lilli Sooväli.** Spectrophotometric measurements and their uncertainty in chemical analysis and dissociation constant measurements. Tartu, 2006, 125 p.
55. **Eve Koort.** Uncertainty estimation of potentiometrically measured ph and pK_a values. Tartu, 2006, 139 p.
56. **Sergei Kopanchuk.** Regulation of ligand binding to melanocortin receptor subtypes. Tartu, 2006, 119 p.
57. **Silvar Kallip.** Surface structure of some bismuth and antimony single crystal electrodes. Tartu, 2006, 107 p.
58. **Kristjan Saal.** Surface silanization and its application in biomolecule coupling. Tartu, 2006, 77 p.
59. **Tanel Tätte.** High viscosity $Sn(OBu)_4$ oligomeric concentrates and their applications in technology. Tartu, 2006, 91 p.
60. **Dimitar Atanasov Dobchev**. Robust QSAR methods for the prediction of properties from molecular structure. Tartu, 2006, 118 p.
61. **Hannes Hagu**. Impact of ultrasound on hydrophobic interactions in solutions. Tartu, 2007, 81 p.

62. **Rutha Jäger.** Electroreduction of peroxodisulfate anion on bismuth electrodes. Tartu, 2007, 142 p.
63. **Kaido Viht.** Immobilizable bisubstrate-analogue inhibitors of basophilic protein kinases: development and application in biosensors. Tartu, 2007, 88 p.
64. **Eva-Ingrid Rõõm.** Acid-base equilibria in nonpolar media. Tartu, 2007, 156 p.
65. **Sven Tamp.** DFT study of the cesium cation containing complexes relevant to the cesium cation binding by the humic acids. Tartu, 2007, 102 p.
66. **Jaak Nerut.** Electroreduction of hexacyanoferrate(III) anion on Cadmium (0001) single crystal electrode. Tartu, 2007, 180 p.
67. **Lauri Jalukse.** Measurement uncertainty estimation in amperometric dissolved oxygen concentration measurement. Tartu, 2007, 112 p.
68. **Aime Lust.** Charge state of dopants and ordered clusters formation in CaF_2:Mn and CaF_2:Eu luminophors. Tartu, 2007, 100 p.
69. **Iiris Kahn**. Quantitative Structure-Activity Relationships of environmentally relevant properties. Tartu, 2007, 98 p.
70. **Mari Reinik.** Nitrates, nitrites, N-nitrosamines and polycyclic aromatic hydrocarbons in food: analytical methods, occurrence and dietary intake. Tartu, 2007, 172 p.
71. **Heili Kasuk.** Thermodynamic parameters and adsorption kinetics of organic compounds forming the compact adsorption layer at Bi single crystal electrodes. Tartu, 2007, 212 p.
72. **Erki Enkvist.** Synthesis of adenosine-peptide conjugates for biological applications. Tartu, 2007, 114 p.
73. **Svetoslav Hristov Slavov**. Biomedical applications of the QSAR approach. Tartu, 2007, 146 p.
74. **Eneli Härk.** Electroreduction of complex cations on electrochemically polished Bi(*hkl*) single crystal electrodes. Tartu, 2008, 158 p.
75. **Priit Möller.** Electrochemical characteristics of some cathodes for medium temperature solid oxide fuel cells, synthesized by solid state reaction technique. Tartu, 2008, 90 p.
76. **Signe Viggor.** Impact of biochemical parameters of genetically different pseudomonads at the degradation of phenolic compounds. Tartu, 2008, 122 p.
77. **Ave Sarapuu.** Electrochemical reduction of oxygen on quinone-modified carbon electrodes and on thin films of platinum and gold. Tartu, 2008, 134 p.
78. **Agnes Kütt.** Studies of acid-base equilibria in non-aqueous media. Tartu, 2008, 198 p.
79. **Rouvim Kadis.** Evaluation of measurement uncertainty in analytical chemistry: related concepts and some points of misinterpretation. Tartu, 2008, 118 p.
80. **Valter Reedo.** Elaboration of IVB group metal oxide structures and their possible applications. Tartu, 2008, 98 p.

81. **Aleksei Kuznetsov.** Allosteric effects in reactions catalyzed by the cAMP-dependent protein kinase catalytic subunit. Tartu, 2009, 133 p.
82. **Aleksei Bredihhin.** Use of mono- and polyanions in the synthesis of multisubstituted hydrazine derivatives. Tartu, 2009, 105 p.
83. **Anu Ploom.** Quantitative structure-reactivity analysis in organosilicon chemistry. Tartu, 2009, 99 p.
84. **Argo Vonk.** Determination of adenosine A_{2A}- and dopamine D_1 receptor-specific modulation of adenylate cyclase activity in rat striatum. Tartu, 2009, 129 p.
85. **Indrek Kivi.** Synthesis and electrochemical characterization of porous cathode materials for intermediate temperature solid oxide fuel cells. Tartu, 2009, 177 p.
86. **Jaanus Eskusson.** Synthesis and characterisation of diamond-like carbon thin films prepared by pulsed laser deposition method. Tartu, 2009, 117 p.
87. **Marko Lätt.** Carbide derived microporous carbon and electrical double layer capacitors. Tartu, 2009, 107 p.
88. **Vladimir Stepanov.** Slow conformational changes in dopamine transporter interaction with its ligands. Tartu, 2009, 103 p.
89. **Aleksander Trummal.** Computational Study of Structural and Solvent Effects on Acidities of Some Brønsted Acids. Tartu, 2009, 103 p.
90. **Eerold Vellemäe.** Applications of mischmetal in organic synthesis. Tartu, 2009, 93 p.
91. **Sven Parkel.** Ligand binding to 5-HT_{1A} receptors and its regulation by Mg^{2+} and Mn^{2+}. Tartu, 2010, 99 p.
92. **Signe Vahur.** Expanding the possibilities of ATR-FT-IR spectroscopy in determination of inorganic pigments. Tartu, 2010, 184 p.
93. **Tavo Romann**. Preparation and surface modification of bismuth thin film, porous, and microelectrodes. Tartu, 2010, 155 p.
94. **Nadežda Aleksejeva.** Electrocatalytic reduction of oxygen on carbon nanotube-based nanocomposite materials. Tartu, 2010, 147 p.
95. **Marko Kullapere.** Electrochemical properties of glassy carbon, nickel and gold electrodes modified with aryl groups. Tartu, 2010, 233 p.
96. **Liis Siinor.** Adsorption kinetics of ions at Bi single crystal planes from aqueous electrolyte solutions and room-temperature ionic liquids. Tartu, 2010, 101 p.
97. **Angela Vaasa.** Development of fluorescence-based kinetic and binding assays for characterization of protein kinases and their inhibitors. Tartu 2010, 101 p.
98. **Indrek Tulp.** Multivariate analysis of chemical and biological properties. Tartu 2010, 105 p.
99. **Aare Selberg.** Evaluation of environmental quality in Northern Estonia by the analysis of leachate. Tartu 2010, 117 p.
100. **Darja Lavõgina.** Development of protein kinase inhibitors based on adenosine analogue-oligoarginine conjugates. Tartu 2010, 248 p.

101. **Laura Herm.** Biochemistry of dopamine D_2 receptors and its association with motivated behaviour. Tartu 2010, 156 p.
102. **Terje Raudsepp.** Influence of dopant anions on the electrochemical properties of polypyrrole films. Tartu 2010, 112 p.
103. **Margus Marandi.** Electroformation of Polypyrrole Films: *In-situ* AFM and STM Study. Tartu 2011, 116 p.
104. **Kairi Kivirand.** Diamine oxidase-based biosensors: construction and working principles. Tartu, 2011, 140 p.
105. **Anneli Kruve.** Matrix effects in liquid-chromatography electrospray mass-spectrometry. Tartu, 2011, 156 p.
106. **Gary Urb.** Assessment of environmental impact of oil shale fly ash from PF and CFB combustion. Tartu, 2011, 108 p.
107. **Nikita Oskolkov.** A novel strategy for peptide-mediated cellular delivery and induction of endosomal escape. Tartu, 2011, 106 p.
108. **Dana Martin.** The QSPR/QSAR approach for the prediction of properties of fullerene derivatives. Tartu, 2011, 98 p.
109. **Säde Viirlaid.** Novel glutathione analogues and their antioxidant activity. Tartu, 2011, 106 p.
110. **Ülis Sõukand.** Simultaneous adsorption of Cd^{2+}, Ni^{2+}, and Pb^{2+} on peat. Tartu, 2011, 124 p.
111. **Lauri Lipping.** The acidity of strong and superstrong Brønsted acids, an outreach for the "limits of growth": a quantum chemical study. Tartu, 2011, 124 p.
112. **Heisi Kurig.** Electrical double-layer capacitors based on ionic liquids as electrolytes. Tartu, 2011, 146 p.
113. **Marje Kasari.** Bisubstrate luminescent probes, optical sensors and affinity adsorbents for measurement of active protein kinases in biological samples. Tartu, 2012, 126 p.
114. **Kalev Takkis.** Virtual screening of chemical databases for bioactive molecules. Tartu, 2012, 122 p.
115. **Ksenija Kisseljova**. Synthesis of aza-β^3-amino acid containing peptides and kinetic study of their phosphorylation by protein kinase A. Tartu, 2012, 104 p.
116. **Riin Rebane.** Advanced method development strategy for derivatization LC/ESI/MS. Tartu, 2012, 184 p.
117. **Vladislav Ivaništšev.** Double layer structure and adsorption kinetics of ions at metal electrodes in room temperature ionic liquids. Tartu, 2012, 128 p.
118. **Irja Helm.** High accuracy gravimetric Winkler method for determination of dissolved oxygen. Tartu, 2012, 139 p.
119. **Karin Kipper.** Fluoroalcohols as Components of LC-ESI-MS Eluents: Usage and Applications. Tartu, 2012, 164 p.
120. **Arno Ratas.** Energy storage and transfer in dosimetric luminescent materials. Tartu, 2012, 163 p.

121. **Reet Reinart-Okugbeni**. Assay systems for characterisation of subtype-selective binding and functional activity of ligands on dopamine receptors. Tartu, 2012, 159 p.
122. **Lauri Sikk.** Computational study of the Sonogashira cross-coupling reaction. Tartu, 2012, 81 p.
123. **Karita Raudkivi.** Neurochemical studies on inter-individual differences in affect-related behaviour of the laboratory rat. Tartu, 2012, 161 p.
124. **Indrek Saar.** Design of GalR2 subtype specific ligands: their role in depression-like behavior and feeding regulation. Tartu, 2013, 126 p.
125. **Ann Laheäär.** Electrochemical characterization of alkali metal salt based non-aqueous electrolytes for supercapacitors. Tartu, 2013, 127 p.
126. **Kerli Tõnurist.** Influence of electrospun separator materials properties on electrochemical performance of electrical double-layer capacitors. Tartu, 2013, 147 p.
127. **Kaija Põhako-Esko.** Novel organic and inorganic ionogels: preparation and characterization. Tartu, 2013, 124 p.
128. **Ivar Kruusenberg.** Electroreduction of oxygen on carbon nanomaterial-based catalysts. Tartu, 2013, 191 p.
129. **Sander Piiskop.** Kinetic effects of ultrasound in aqueous acetonitrile solutions. Tartu, 2013, 95 p.
130. **Ilona Faustova**. Regulatory role of L-type pyruvate kinase N-terminal domain. Tartu, 2013, 109 p.
131. **Kadi Tamm.** Synthesis and characterization of the micro-mesoporous anode materials and testing of the medium temperature solid oxide fuel cell single cells. Tartu, 2013, 138 p.
132. **Iva Bozhidarova Stoyanova-Slavova.** Validation of QSAR/QSPR for regulatory purposes. Tartu, 2013, 109 p.
133. **Vitali Grozovski**. Adsorption of organic molecules at single crystal electrodes studied by *in situ* STM method. Tartu, 2014, 146 p.
134. **Santa Veikšina**. Development of assay systems for characterisation of ligand binding properties to melanocortin 4 receptors. Tartu, 2014, 151 p.
135. **Jüri Liiv.** PVDF (polyvinylidene difluoride) as material for active element of twisting-ball displays. Tartu, 2014, 111 p.
136. **Kersti Vaarmets.** Electrochemical and physical characterization of pristine and activated molybdenum carbide-derived carbon electrodes for the oxygen electroreduction reaction. Tartu, 2014, 131 p.
137. **Lauri Tõntson**. Regulation of G-protein subtypes by receptors, guanine nucleotides and Mn^{2+}. Tartu, 2014, 105 p.
138. **Aiko Adamson.** Properties of amine-boranes and phosphorus analogues in the gas phase. Tartu, 2014, 78 p.
139. **Elo Kibena**. Electrochemical grafting of glassy carbon, gold, highly oriented pyrolytic graphite and chemical vapour deposition-grown graphene electrodes by diazonium reduction method. Tartu, 2014, 184 p.

140. **Teemu Näykki.** Novel Tools for Water Quality Monitoring – From Field to Laboratory. Tartu, 2014, 202 p.
141. **Karl Kaupmees.** Acidity and basicity in non-aqueous media: importance of solvent properties and purity. Tartu, 2014, 128 p.
142. **Oleg Lebedev**. Hydrazine polyanions: different strategies in the synthesis of heterocycles. Tartu, 2015, 118 p.
143. **Geven Piir.** Environmental risk assessment of chemicals using QSAR methods. Tartu, 2015, 123 p.
144. **Olga Mazina.** Development and application of the biosensor assay for measurements of cyclic adenosine monophosphate in studies of G protein-coupled receptor signalinga. Tartu, 2015, 116 p.
145. **Sandip Ashokrao Kadam.** Anion receptors: synthesis and accurate binding measurements. Tartu, 2015, 116 p.
146. **Indrek Tallo.** Synthesis and characterization of new micro-mesoporous carbide derived carbon materials for high energy and power density electrical double layer capacitors. Tartu, 2015, 148 p.
147. **Heiki Erikson.** Electrochemical reduction of oxygen on nanostructured palladium and gold catalysts. Tartu, 2015, 204 p.
148. **Erik Anderson.** *In situ* Scanning Tunnelling Microscopy studies of the interfacial structure between Bi(111) electrode and a room temperature ionic liquid. Tartu, 2015, 118 p.
149. **Girinath G. Pillai.** Computational Modelling of Diverse Chemical, Bio-chemical and Biomedical Properties. Tartu, 2015, 140 p.
150. **Piret Pikma.** Interfacial structure and adsorption of organic compounds at Cd(0001) and Sb(111) electrodes from ionic liquid and aqueous electrolytes: an *in situ* STM study. Tartu, 2015, 126 p.
151. **Ganesh babu Manoharan.** Combining chemical and genetic approaches for photoluminescence assays of protein kinases. Tartu, 2016, 126 p.
152. **Carolin Siimenson**. Electrochemical characterization of halide ion adsorption from liquid mixtures at Bi(111) and pyrolytic graphite electrode surface. Tartu, 2016, 110 p.
153. **Asko Laaniste.** Comparison and optimisation of novel mass spectrometry ionisation sources. Tartu, 2016, 156 p.
154. **Hanno Evard.** Estimating limit of detection for mass spectrometric analysis methods. Tartu, 2016, 224 p.
155. **Kadri Ligi.** Characterization and application of protein kinase-responsive organic probes with triplet-singlet energy transfer. Tartu, 2016, 122 p.
156. **Margarita Kagan.** Biosensing penicillins' residues in milk flows. Tartu, 2016, 130 p.
157. **Marie Kriisa.** Development of protein kinase-responsive photo-luminescent probes and cellular regulators of protein phosphorylation. Tartu, 2016, 106 p.